Search for a Heavy Right-Handed W Boson and Heavy Right-Handed Neutrino of the Left-Right Symmetric Extension of the Standard Theory

A DISSERTATION

SUBMITTED TO THE FACULTY OF THE GRADUATE SCHOOL

OF THE UNIVERSITY OF MINNESOTA

BY

Sean Thomas Kalafut

IN PARTIAL FULFILLMENT OF THE REQUIREMENTS

FOR THE DEGREE OF

DOCTOR OF PHILOSOPHY

Professor Roger W. Rusack

December, 2017

Acknowledgements

There are many people that I want to acknowledge for their contributions to my research, life and personal development as a graduate student.

First and foremost, I thank my parents Tom and Jane Kalafut, and my brother and sister Devin and Megan Kalafut for the time they spent with me, their advice, and everything that they did for me during my graduate career.

During the orientation for new PhD students, Professor Joseph Kapusta and I became fast friends through our mutual interest in cars and racing. I will be forever indebted to Joe because he helped me understand quantum field theory, and, most importantly, he introduced me to my research advisor - Professor Roger Rusack. For me, Roger was the ideal advisor. He has immense patience, exemplary knowledge of the English language, grammar and writing, and impressive management abilities. Thanks to Roger I wrote a doctoral dissertation that I am proud of, and I developed a large network of contacts within the CMS collaboration at Fermilab and CERN that helped me achieve my goals. In addition, Roger instilled in me greater self-confidence, emphasized the value of fastidious research, and, above all, helped me improve myself. Through Roger I had the privelege of getting to know and working with Professors Jeremy Mans and Yuichi Kubota at Minnesota, Dr. Frank Chlebana and Professor Richard Cavanaugh at Fermilab, Dr. Rajdeep Chatterjee, and Dr. Shervin Nourbahksh and many other CMS ECAL experts at CERN.

I would also like to thank all my collaborators in CMS and at the LHC who have made this research possible through their dedication. The excellence of the CMS and LHC physics programs speaks for itself, but none the less I am grateful to all those involved.

The methods and results presented in this thesis were improved and refined through conversations with the people discussed previously, and several other people that played important roles in my graduate career. My collaborators Shervin Nourbahksh and Dr. Nicole Manuela Ruckstuhl and Giulia Negro at CERN, Peter Hansen and Andrew Evans at Minnesota, and Professor Peter Wittich and Jorge Chaves at Cornell. They all provided invaluable insight into particle physics research, and literally gave me food for thought by sharing their knowledge of international cuisines in response to my countless questions about food. I also thank Dr. Niki Saoulidou and Dr. Dinko Ferencek for their useful questions and comments during the analysis review process.

I am grateful to Dr. Joe (Nathaniel) Pastika, Alexey Finkel, Dr. Tutanon Sinthuprasith, and Gabriele Meoni for their friendship and their advice in research and important aspects of life. All of them helped me improve myself, and become more productive in research and in recreational pursuits.

Since childhood I have been interested in other cultures, and curious to learn more about them. In 2012 an opportunity to learn more about Russian culture presented itself; I took advantage of the opportunity, and, in the time since then, my life has transformed into something better than I ever imagined. Many native Russian speakers around the world have contributed to this transformation, and I want to thank several people in particular: Vladimir Bychkov and his wife Nina Nikitina, Alexandra Rezova, Misha Kreshchuk, Serdar Kurbanov, Dr. Maxim Konyushikhin and his wife Valentina Maslova, and Professor Misha Shifman.

Dedication

This thesis is dedicated to my wonderful parents Tom and Jane Kalafut, my brother Devin Kalafut, and my sister Megan Kalafut.

Abstract

A search for a heavy right-handed W_R boson, and heavy right-handed neutrinos N_l ($\ell = e, \mu$) performed by the CMS experiment is summarized here. Using the 2.6 fb^{-1} of integrated luminosity recorded by the CMS experiment in 2015 at a center-of-mass energy of 13 TeV, this search seeks evidence of a W_R boson and N_l neutrinos in events with two leptons and two jets. The data do not significantly exceed expected backgrounds, and are consistent with expected results of the Standard Theory given uncertainties. For Standard Theory extensions with strict left-right symmetry, and assuming only one N_l flavor contributes significantly to the W_R decay width, mass limits are set in the two-dimensional (M_{W_R}, M_{N_l}) plane at 95% confidence level. The limits extend to a W_R mass of 3.3 TeV in the electron channel and 3.5 TeV in the muon channel, and span a wide range of N_l masses below M_{W_R}.

Contents

List of Tables

List of Figures

Chapter 1

Introduction

The Standard Theory of particle physics (ST) [5, 6] is a quantum field theory that describes the fundamental components of matter and their interactions. It was developed in light of experimental observations made in the 1960s and 1970s and earlier, and over the past several decades the details of the theory have survived many experimental tests.

Neutrinos and the weak interaction played an important role in the development of the ST. Neutrinos were first proposed in 1929 to preserve energy conservation in beta decays, and were first confirmed by experimental evidence [7] with the observation of a neutrino in 1956, later identified as the electron neutrino. Initially it was believed only one neutrino existed. The subsequent discovery of a second neutrino [8], later identified as the muon neutrino, motivated theories that predicted each charged lepton had a corresponding neutrino. These predictions were confirmed by experimental evidence [9] of the tau neutrino in 2001. Neutrinos were predicted to interact only through weak interactions, so advances in the understanding of neutrino physics and the theory of weak interactions often coincided. A 1932 theoretical model of the weak interaction was proposed to explain beta decay, and included a massless neutral lepton later identified as the electron neutrino. In the 1950s experimental measurements of hadron decay rates

through the weak interaction, like $K^+ \to 2\pi, 3\pi$, motivated new, parity violating models of the weak interaction; parity violating weak interactions were observed experimentally [10] in 1957. In the 1970s and earlier, experimental measurements of neutrinos[1] were consistent with massless neutrinos within experimental uncertainties, so the ST was developed with massless neutrinos, and modeled the weak interaction as a parity violating quantum field theory.

The success of the ST is exemplified by the quantum field model of electromagnetic and weak (electroweak) interactions. The electroweak model predicts the existence of a massive, neutral gauge boson, the Z, that mediates weak interactions. Existence of the Z was first confirmed by observations of neutral current scattering between neutrinos [11] in 1973. Later at LEP and the Tevatron, precise measurements of electroweak coupling strengths and gauge boson (W, Z) masses put indirect limits on the Higgs boson mass. The Higgs boson was observed in 2012 at the Large Hadron Collider (LHC) by the ATLAS and CMS experiments, and its mass[12] of 125 GeV was consistent with previous electroweak limits.

The ST makes many successful predictions, but there are indications that the ST is not a complete theory of the universe. Within the electroweak sector, the ST does not predict the experimentally observed baryon-antibaryon asymmetry or neutrino oscillations. Neutrino flavor oscillations were first suggested in 1957, and have been confirmed experimentally [13, 14, 15, 16, 17, 18]. This evidence supports models with massive neutrinos, and motivates extensions to the ST. The Left-Right Symmetric (LRS) extension of the ST predicts massive neutrinos, and retains ST predictions supported by experimental evidence.

The LRS model extends the ST electroweak sector by adding an $SU(2)_R$ gauge group and three heavy, right-handed neutrinos N_l. Due to the new gauge group, the

[1] ν energy spectra in beta decays, ν-nucleon interaction cross sections

LRS model predicts a new charged weak boson W_R that couples to N_l and all right-handed ST fermions. Since the W_R couples to quarks, evidence of the LRS model can be searched for using data collected from proton-proton collisions at the CERN LHC. In this thesis, a search for a W_R boson and N_l in events with two charged leptons and two jets collected by the CMS experiment in 2015 is presented.

Chapter 2

Theoretical Motivations

The experimental evidence of neutrino oscillations motivates extensions to the ST. Neutrino flavor oscillations have been observed by experiments [13, 14, 15, 16, 17, 18], and these observations imply that neutrinos have mass. Neutrinos in the ST are only produced in left-handed states, so an extension, like the LRS model, with massive neutrinos is needed for a Lorentz invariant theory.

In this chapter, particle mass generation is discussed as a precursor to ST extensions; then, the Majorana neutrino model and the LRS model are explained, highlighting how these extensions show better agreement with experimental observations than the ST. In conclusion, important characteristics of the LRS model that can be studied at the LHC are presented.

2.1 Particle Masses in the Standard Theory

In the ST the Brout-Englert-Higgs (BEH) mechanism transforms the four $SU(2)_L \times U(1)$ group generators into the electroweak interaction mediators. The BEH mechanism introduces a complex doublet Φ, representing four scalar bosons, that obey the Lagrangian

$\mathcal{L}_H$:

$$\Phi = \begin{bmatrix} \phi^+ \\ \phi^0 \end{bmatrix} \tag{2.1}$$

$$\mathcal{L}_H = (D_\mu \Phi)^\dagger D^\mu \Phi - V(\Phi); \quad V(\Phi) = \frac{1}{2}(|\Phi|^2 - \frac{\nu^2}{2}) \tag{2.2}$$

where $V(\Phi)$ is the Higgs potential (Figure 2.1), and $D_\mu = \partial_\mu + ig_L\tau^j A^j_\mu + i\frac{g'}{2}YB_\mu$ represents the propagation of the Higgs doublet Φ, and its couplings to the $SU(2)_L$ and $U(1)$ generators τ^j and Y and the massless vector fields A^j_μ and B_μ. g_L and g' set the weak and electromagnetic interaction coupling strengths. The Higgs doublet Φ naturally adopts a value $< \Phi >= (0\ \frac{\nu}{\sqrt{2}})$ that minimizes the Higgs potential, after which $\mathcal{L}_H$ reduces to Equation 2.3:

$$\mathcal{L}_{HK} = \frac{\nu^2}{8}[g_L^2(A^1_\mu + iA^2_\mu)(A^{1\mu} - iA^{2\mu}) + (g'B_\mu - g_L A^3_\mu)^2] \tag{2.3}$$

Defining the photon vector field A_μ, and the weak boson vector fields $W^\pm_\mu$ and Z_μ as:

$$W^\pm_\mu \equiv \frac{1}{\sqrt{2}}(A^1_\mu \pm iA^2_\mu), Z_\mu \equiv \frac{1}{\sqrt{g'^2 + g_L^2}}(g'B_\mu - g_L A^3_\mu), A_\mu \equiv \frac{1}{\sqrt{g'^2 + g_L^2}}(g_L B_\mu + g' A^3_\mu) \tag{2.4}$$

transforms $\mathcal{L}_{HK}$ (Equation 2.3) into:

$$\mathcal{L}_{HK} = (\frac{\nu g_L}{2})^2 W^+_\mu W^{-\mu} + \frac{1}{2}(\frac{\nu\bar{g}}{2})^2 Z_\mu Z^\mu + 0 A_\mu A^\mu \tag{2.5}$$

where $\bar{g} \equiv \sqrt{g'^2 + g_L^2}$. Following from this Lagrangian, the photon A_μ is massless, the

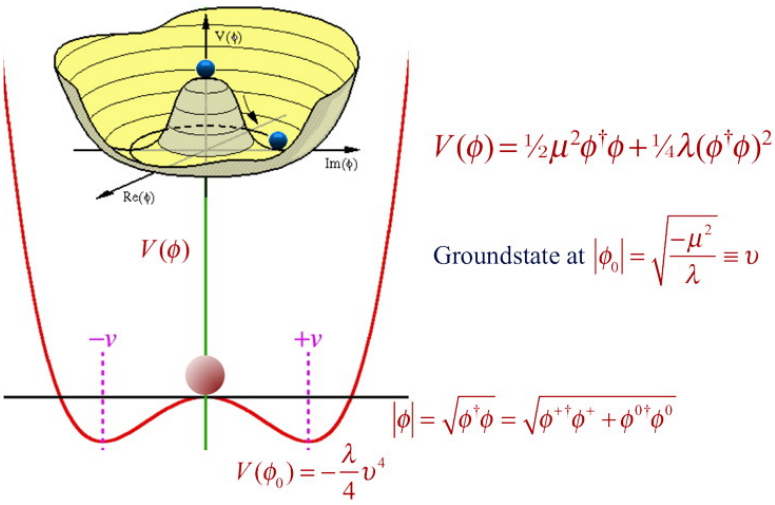

Figure 2.1: The Higgs potential drives the ST Higgs field to a stable state with non-zero vacuum expectation value, from *The Swiss Physical Society* [1].

Z boson has mass $m_Z = \nu\bar{g}/2$, and the $W^\pm$ bosons have mass $m_W = \nu g_L/2$. Three of the four scalar fields introduced by the BEH mechanism are consumed to give mass to the Z and $W^\pm$ bosons. The fourth scalar field manifests as a scalar boson, the Higgs boson, and couples to all massive particles with a coupling strength proportional to the particle's mass. The observation of the Higgs boson [12] supports the ST prediction that the Z and $W^\pm$ bosons acquire mass through the BEH mechanism.

In the ST, fermions acquire mass by adding more scalar Higgs fields to the BEH mechanism. Additional Higgs fields add mass terms of the form $-mf\bar{f}$, where f is a fermion, to the Lagrangian. In the basis where a fermion field f consists of right- and left-handed components χ_R and χ_L, $f = (\chi_L, \chi_R)$, a fermion mass term in the Lagrangian is expressed as:

$$\mathcal{L}_D = -m\bar{f}f = -m\chi_L^\dagger\chi_R - m\chi_R^\dagger\chi_L \tag{2.6}$$

This type of mass term, called a Dirac mass, contains the product of left- and right-handed fields. Experimentally, quarks and charged leptons exist in left and right-handed states that are degenerate in mass, so Dirac mass terms are used to give mass to the fermions in the ST.

Neutrinos play a special role in the ST. They are neutral, massless fermions, that only interact through the weak interaction. In addition, due to parity violation in the weak interaction, anti-neutrinos are always right-handed, and neutrinos are always left-handed. In the ST mass can only be assigned to a fermion through a Dirac mass term (Equation 2.6), which depends on the product of left- and right-handed fields. The Dirac mass term for a neutrino yields a mass of zero, so an extension is required to account for the experimental observation of massive neutrinos.

2.2 Standard Theory Extensions

There are several ways that the ST can be extended to accommodate massive, fermionic neutrinos. In one of the simplest extensions neutrinos are Majorana fermions, which are their own anti-particles, and have masses m_L and m_R defined in the Lagrangian $\mathcal{L}_M$:

$$\mathcal{L}_M = -m_L \chi_L^\dagger \chi_L - m_R \chi_R^\dagger \chi_R \tag{2.7}$$

The two Majorana masses are generated through an extended Higgs model. A consequence of Majorana neutrinos is that neutrinoless double beta decays could occur. This has not yet been observed [19, 20], leading to the exploration of alternate ideas.

One alternative is the Left-Right Symmetric (LRS) model, which predicts massive fermionic neutrinos that have not yet been observed in experiments. First proposed in 1974 [21], the LRS model predicts an electroweak interaction existed in the very early universe that conserved parity and was mediated by seven massless gauge bosons. An

extension of the ST BEH mechanism transformed the seven massless gauge bosons into the ST electroweak bosons, and the heavier $W_R^{\pm}$ (W_R) and Z' bosons.

In the LRS model an $SU(2)_R$ group is added to the ST electroweak $SU(2)_L \times U(1)$ groups. This introduces three massless vector fields $\xi^j_{R\mu}$, which become massive bosons through an extended BEH mechanism. The mechanism is extended in two stages, and ultimately yields one massless and six massive gauge bosons that mediate the electroweak interactions. In the first stage [22], a chiral, complex Higgs doublet $\chi_{L,R}$ is introduced:

$$\chi_{L,R} = \begin{bmatrix} \chi^+_{L,R} \\ \chi^0_{L,R} \end{bmatrix} \tag{2.8}$$

with bosonic fields that couple independently to the left- and right-handed gauge bosons. The propagation and interaction of these new fields with other massless bosons is described by the Lagrangian:

$$\mathcal{L}_{H,LRS} = \frac{1}{2}(D_\mu \chi_L)^\dagger D^\mu \chi_L + \frac{1}{2}(D_\mu \chi_R)^\dagger D^\mu \chi_R - V(\chi_{L,R}) \tag{2.9}$$

where $D_\mu = \partial_\mu + ig_L \tau^j A^j_{L\mu} + ig_R \tau^j \xi^j_{R\mu} + i\frac{g'}{2} Y B_\mu$ contains the massless boson fields $A^j_{L\mu}, \xi^j_{R\mu}, B_\mu$ multiplied by the generators of the $SU(2)_L, SU(2)_R, U(1)$ groups. In the simplified LRS model considered here the coupling strengths g_R, g_L were assumed to be equal, and are denoted as g. The potential $V(\chi_{L,R})$ respects the LRS model symmetries, and depends on a constant U_R. $\chi_{L,R}$ equilibrates at $< \chi^+_{L,R} >= 0, < \chi^0_L >= 0, < \chi^0_R >= U_R$ to minimize $V(\chi_{L,R})$, and subsequently creates new fields:

$$W^{\pm}_{R\mu} \equiv \frac{1}{\sqrt{2}}(\xi^1_{R\mu} \mp i\xi^2_{R\mu}); \quad Z'_\mu \equiv \frac{1}{\sqrt{g'^2 + g^2}}(-g' B_\mu + g\xi^3_{R\mu}) \tag{2.10}$$

that have masses:

$$M_{W_R} = \frac{1}{2} g U_R \quad m_{Z'} = \frac{1}{2} U_R \sqrt{g'^2 + g^2} \tag{2.11}$$

After the first stage, the W_R and Z' bosons are predicted to have masses $M_{W_R} = \frac{1}{2} g U_R$ and $m_{Z'} = \frac{1}{2} U_R \sqrt{g'^2 + g^2}$, and all other bosons remain massless.

In the second stage [22, 23], two complex Higgs doublets ϕ_1 and ϕ_2 are introduced through a multiplet Φ:

$$\Phi = \begin{bmatrix} \phi_1^0 & \phi_2^+ \\ \phi_1^- & \phi_2^0 \end{bmatrix} \tag{2.12}$$

This multiplet interacts with the left- and right-handed $SU(2)$ boson fields, and these interactions are described by a Lagrangian $\mathcal{L}_{H2,LRS}$ similar to Equation 2.9 but with additional terms for the second Higgs doublet. Within $\mathcal{L}_{H2,LRS}$ is a potential $V(\phi_1, \phi_2)$, and Φ naturally adopts a non-zero expectation value that minimizes $V(\phi_1, \phi_2)$:

$$< \Phi > = \begin{bmatrix} \nu_1 & 0 \\ 0 & \nu_2 \end{bmatrix} \tag{2.13}$$

At equilibrium, the W_R, Z', and the ST $W^{\pm}$ and Z bosons have masses:

$$m_W = \frac{1}{2} g \nu, \quad m_{W_R} \simeq \frac{1}{2} g U_R, \quad m_Z = \frac{1}{2} \bar{g} \nu, \quad m_{Z'} \simeq \frac{1}{2} \bar{g} U_R \tag{2.14}$$

$$\nu^2 \equiv \nu_1^2 + \nu_2^2, \quad \bar{g}^2 \equiv g^2 + g'^2 \tag{2.15}$$

It is assumed that $U_R \gg \nu$, and there is negligible mixing between the left and right-handed leptons. Thus, the LRS model predicts the correct masses for the ST weak bosons, and the masses of three new, heavier bosons. The mass difference between the left-handed $W^{\pm}, Z$ and the right-handed W_R, Z' is an indication of parity violation in the LRS model; compared with the ST where parity violation does not have a clear theoretical motivation. In the fermionic sector, the LRS model predicts new neutrinos with masses consistent with neutrino flavor oscillations.

With the addition of the $SU(2)_R$ group, three new right-handed neutrinos N_R^l (N_l) arise naturally to form doublets of $SU(2)_R$ hypercharge with right-handed charged leptons. The LRS model predicts non-zero masses for N_l and ST neutrinos using a mixture of Dirac and Majorana mass terms [24, 25]:

$$\mathcal{L} = \frac{1}{2}(\bar{\nu}_{Li} \quad \bar{\nu}_{Ri}) \begin{bmatrix} B_i' & M_i \\ M_i & B_i \end{bmatrix} (\nu_{Li} \quad \nu_{Ri})^T \tag{2.16}$$

where i is the lepton generation, and ν_L and ν_R are massive, pure left and right-handed fermionic neutrino fields. The nonzero value of $< \Phi >$ in Equation 2.13 leads to the Dirac masses M_i, and the expectation values of χ_L and χ_R defined in Equation 2.8 lead to the Majorana masses B_i' and B_i. As a result, $M_i \sim \nu$, $B_i' \sim 0$, $B_i \sim U_R$, and $B_i \gg M_i$, which is consistent with $m_{W_R} \gg m_W$. Substituting ν and U_R for the Dirac and Majorana masses, Equation 2.16 is diagonalized and yields the following neutrino mass eigenvalues, assuming negligible left-right mixing:

$$\lambda_{i+} \simeq B_i, \quad \lambda_{i-} \simeq \frac{M_i^2}{B_i} \tag{2.17}$$

The detectable states N_i and ν_i that participate in electroweak interactions are mixtures of the pure left- and right-handed neutrino fields:

$$\nu_i \simeq \frac{1}{\sqrt{M_i^2 + B_i^2}}(B_i\nu_{Li} - M_i\nu_{Ri}) \simeq \nu_{Li} - \frac{M_i}{B_i}\nu_{Ri}$$

$$\mathrm{N}_i \simeq \frac{1}{\sqrt{M_i^2+B_i^2}}(M_i\nu_{Li} + B_i\nu_{Ri}) \simeq \nu_{Ri} + \frac{M_i}{B_i}\nu_{Li}$$

(2.18)

that have masses:

$$m_{\nu_i} = \lambda_{i-} \simeq \frac{M_i^2}{B_i}, \quad m_{N_i} = \lambda_{i+} \simeq B_i \tag{2.19}$$

Thus, the LRS model predicts the left-handed neutrinos ν_i have masses $\lambda_{i-} \simeq M_i\frac{M_i}{B_i}$, and the right-handed neutrinos N_i have masses $\lambda_{i+} \simeq B_i \gg M_i$. Appropriate choices for M_i and B_i yields very light left-handed neutrinos, very heavy right-handed neutrinos, and negligible mixing between left- and right-handed states (suppressed by $\sim \frac{M_i}{B_i} \ll 1$), which is consistent with the experimental evidence [26, 27].

In addition to predicting massive neutrinos and parity violation in the weak interaction, the LRS model, through W_R and Z' mediated interactions, predicts more CP violation than in the ST [28]. Hence, the LRS model predicts an asymmetry between the number of baryons and anti-baryons that is closer to observations.

2.3 LRS Model Phenomenology

The LRS model discussed thus far retains all the aspects of the ST, and predicts massive neutrinos, parity violation in a natural way, and explains the baryon-antibaryon asymmetry of the universe. Specific realizations of the LRS model retain these features, and are distinguished by unique values of several free parameters: the weak coupling

constant g_R, the left-right symmetric energy scale U_R that sets the W_R mass, the masses B_i and M_i that set the N_l and ST ν masses, and the three mixing angles θ_i and the CP violating phase δ_R^{CP} that define the W_R analogue of the CKM quark mixing matrix. In this analysis the coupling g_R is assumed to be the same for all lepton flavors and equal to the ST weak coupling g_L. Both the W_R and N_l masses are constrained by unitarity to be $<\sim$ 3000 TeV [29]. Furthermore, the W_R is excluded at 95% CL for $M_{W_R} < 2.5$ TeV based on the measured neutral kaon $K_L - K_S$ mass difference [30]. The N_l mass (M_{N_l}) can be above or below M_{W_R}, but as M_{N_l} decreases both the rate of mixing between the N_l and ST ν, and the left-handed component of N_l increase. The larger left-handed component of N_l increases the rate of $N_l \to W^{\pm}\ell^{\mp}$. If M_{N_l} is close to the Z boson mass, energetic ST neutrinos from $Z \to \nu\nu$ decays could mix into N_l states, and produce a charged lepton through $pp \to Z \to \nu\nu \to \nu N_l \to \nu W^{\pm}\ell^{\mp}$. Measurements that are sensitive to the $Z \to \nu\nu$ rate [31, 32] have not seen any deviations from ST predictions, so it is expected that $M_{N_l} \gtrsim 90$ GeV.

Not all realizations of the LRS model can be tested at the LHC. However, at LHC energies there are some specific LRS model realizations that can be tested, if the following assumptions are made:

- The ST quarks and all right-handed leptons couple to the W_R and Z' with the same strengths as the ST quarks and all left-handed leptons couple to the ST weak bosons. This constrains the W_R analogue of the CKM matrix to match the ST CKM matrix.

- The right-handed neutrinos N_l are lighter than the W_R, and hence the W_R decays to the N_l.

- The decay of the N_l does not violate lepton flavor conservation, and hence only the processes $W_R \to eN_e \to eeW_R^*$ and $W_R \to \mu N_\mu \to \mu\mu W_R^*$ are allowed.

Given these assumptions, the W_R and Z' bosons can be produced in proton-proton (pp) collisions delivered by the LHC and recorded by the CMS experiment. The lighter W_R is more likely than the Z' to have a mass within the LHC's reach, so LRS model realizations were tested by searching for evidence of the W_R boson, where the W_R decays to a pair of quarks or a charged lepton ℓ and a heavy neutrino N_l. The W_R decay to a quark pair has the highest branching fraction, but does not permit a N_l mass measurement. The $W_R \to \ell N_l$ decay permits a measurement of the neutrino mass M_{N_l}, and this decay is the subject of this thesis.

2.4 Experimental Signature

In the $W_R \to l_1 N_l$ decay, the N_l decays to a virtual $Z'*$ and N_l^*, or a second charged lepton l_2 and a virtual W_R^*. The decay of the N_l to a charged lepton and two quarks through a virtual W_R^*, $N_l \to l_2 W_R^* \to l_2 q_1 q_2$, has the highest branching fraction and provides good M_{N_l} resolution because the energies of $l_2 q_1 q_2$ can be measured directly. Therefore, the N_l was searched for in the $N_l \to l_2 q_1 q_2$ decay mode. The production and decay of a W_R and N_l,$pp \to W_R \to l_1 N_l \to l_1 l_2 q_1 q_2$ ($l_1 l_2 = ee, \mu\mu$), is expected to produce events with two same flavor leptons and two quarks that hadronize into two jets, as shown in Figure 2.2. Based on prior searches [33] the W_R is expected to be heavier than 2 TeV, so it decays to high energy leptons and jets. By measuring the energies and trajectories of the leptons and jets, the dilepton-dijet invariant mass ($M_{\ell\ell jj}$) and lepton-dijet invariant mass ($M_{\ell jj}$) can be found, from which the W_R and N_l masses can be extracted: $M_{W_R} = M_{\ell\ell jj}$, $M_{N_l} = M_{\ell jj}$. In the CMS experiment, described in the next chapter, how the energies and trajectories of leptons and jets produced in proton-proton collisions are measured is described.

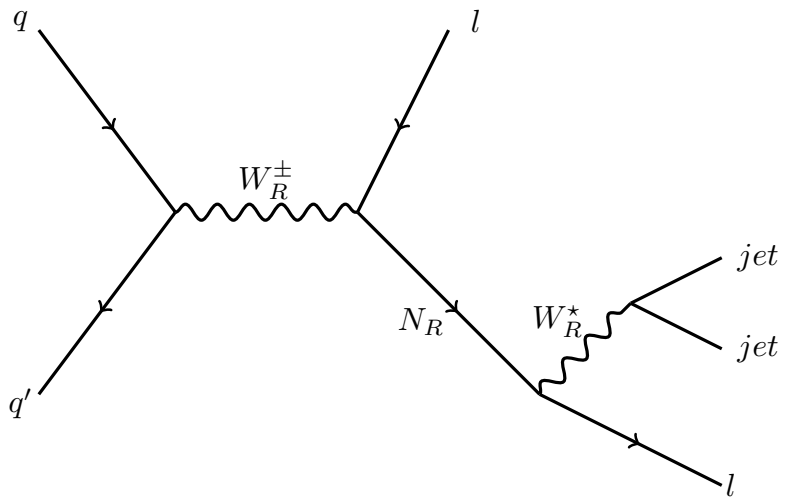

Figure 2.2: Production of a W_R boson and a heavy neutrino N_l and their decays to two charged leptons and two jets.

Chapter 3

The CMS Detector

The energies and trajectories of charged leptons and jets produced in proton-proton (pp) collisions are measured so that the masses M_{W_R} and M_{N_l} can be determined. The maximum M_{W_R} and M_{N_l} that can be measured are constrained by the pp collision energy and collision intensity integrated over time. The mass resolutions are driven by the resolutions with which the lepton and jet energies and trajectories are measured. In this chapter, the CERN Large Hadron Collider (LHC) and the pp collisions it delivers are described as a prelude to the main topic of the chapter - the Compact Muon Solenoid (CMS) sub-detectors that are used to identify leptons and jets, and measure their energies and trajectories. The structure and the performance of the sub-detectors used to detect leptons and jets are described here, and a more detailed explanation is given elsewhere [34].

3.1 The LHC and CMS Overview

The LHC was constructed in a 27 km circular tunnel [35] to deliver pp collisions at 13 TeV. In the collider two proton beams that contained ∼2300 proton bunches, with 25 ns

separating adjacent bunches are collided at the center of the CMS detector. Collisions occurred at 4 interaction points (IPs), and the beam optics were such that the highest intensity collisions occurred at 2 IPs. The general purpose ATLAS (A Toroidal Lhc Apparatus) [36] and CMS [37] experiments were built around these IPs, and the CMS IP coincides with the geometric center of CMS. The interaction intensity $\mathcal{L}$, given by Equation 3.1, is inversely proportional to the product of the two beam areas $4\pi\epsilon_n\beta^*$, and proportional to a geometric factor F based on the beam crossing angle, and the rate of protons crossing the IP $fnN^2\gamma$. The interaction frequency f is fixed at 40 MHz by the time separating adjacent bunches, the Lorentz boost γ is fixed by the beam energy, and the factor F is fixed by the LHC design. The other parameters - the number of bunches n, the number of protons per bunch N, and the beam areas - are manipulated to maximize the interaction intensity $\mathcal{L}$. In 2015 the intensity at the CMS IP approached $6 \times 10^{33} \frac{Hz}{cm^2}$ ($6 \times 10^{-3} \frac{Hz}{pb}$), and the intensity integrated over the year was 2.6 fb^{-1} [38].

$$\mathcal{L} = \frac{fnN^2\gamma}{4\pi\epsilon_n\beta^*}F \tag{3.1}$$

Particles produced at the CMS IP were detected using the sub-detectors shown in Figure 3.1. Located closest to the IP was the silicon tracker, which was used to detect and track charged particles. Surrounding the tracker were the electromagnetic (ECAL) and hadronic (HCAL) calorimeters, which were used to identify and measure the kinematics of photons and electrons ($e^{\pm}$), and neutral and charged hadrons. The tracker and both calorimeters were inside a solenoid magnet that generated a 3.8 T magnetic field. Muon detectors were located in the iron magnet return yoke where the magnetic field strength varied between 1 and 3 T, and were used to detect and track muons ($\mu^{\pm}$) over several meters. Each sub-detector covered 360° in the plane perpendicular to the beam axis, and was divided into a barrel and two endcap sections to detect particles over a large angular region: between 5.65° and 90° away from the

beam axis.

Particles detected in each sub-detector were characterized by energies perpendicular to the beam axis and trajectories relative to the IP. The tracker and muon detectors measured the scalar transverse momentum (p_T) of particles, and the calorimeters measured their scalar transverse energy (E_T). Detected particles were assumed to be massless, so p_T and E_T were equivalent. Each particle's trajectory was represented by a vector pointing from the IP to the spatial position of an energy measurement, and the vector coordinates were expressed in terms of two quantities: the angle ϕ, $0 \leq \phi < 2\pi$, in the plane perpendicular to the beam direction, and the pseudorapidity η:

$$\eta \equiv \frac{1}{2} \ln \frac{E + p_z}{E - p_z} \tag{3.2}$$

where E is the magnitude of the particle's energy, and p_z is the particle's momentum along the beam direction. The transverse energies E_T and p_T are related to the magnitudes E and $|p|$ by $E_T \equiv E/\cosh\eta$ and $p_T \equiv |p|/\cosh\eta$. The quantities η and ϕ were also used to quantify the distance between two trajectories as $\Delta R \equiv \sqrt{\eta^2 + \phi^2}$. Finally, each particle detected in the tracker was also distinguished by a point of origin - an interaction vertex. Each vertex's position was measured from the IP, and was defined by a transverse distance perpendicular to the beam axis, and a longitudinal distance along the beam axis.

3.2 The Silicon Tracker

The silicon tracker consisted of silicon pixel and strip detectors whose purpose was to detect and track charged particles as they traverse the magnetic field, thereby measuring their radii of curvature. Then the points where particle tracks originated were used to identify interaction vertices. Closest to the beam axis was the pixel detector, which

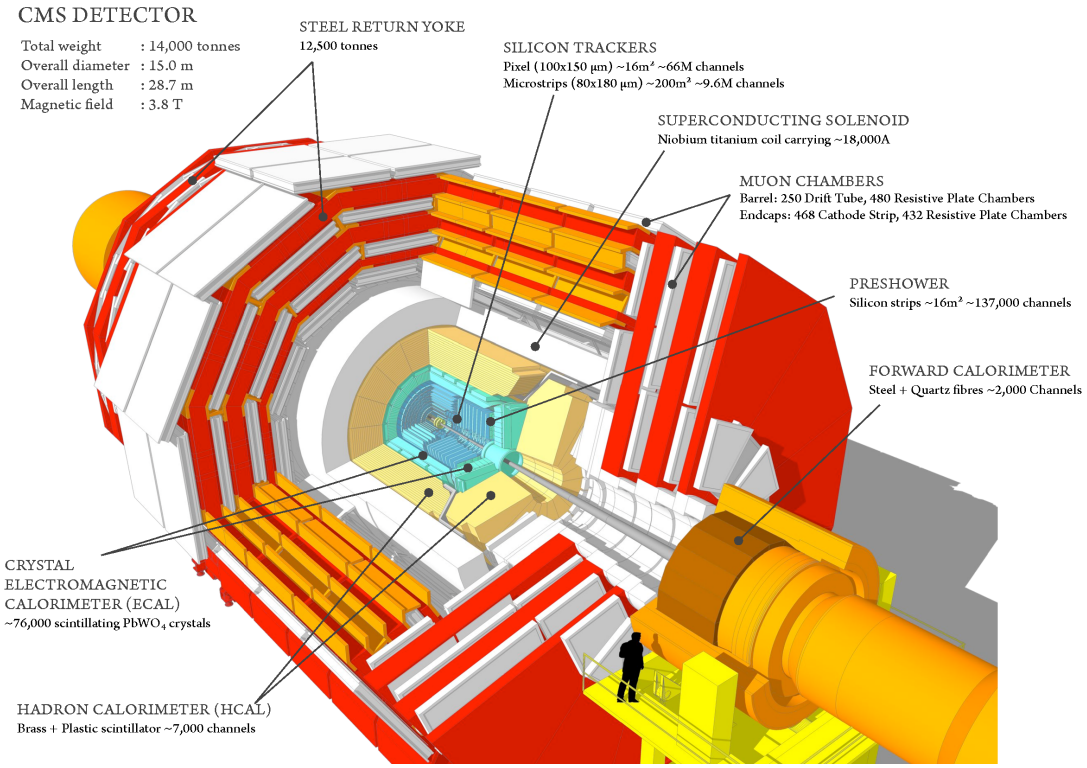

Figure 3.1: Cut-away view of the entire CMS detector. Closest to the proton-proton interaction point is the silicon tracker, followed by the electromagnetic calorimeter, then the hadronic calorimeter, and the magnet. The muon detectors are located in the magnet iron return yoke.

used silicon pixels to measure particles' points of origin and their trajectories up to 15 cm from the z axis. Surrounding the pixel detector was the strip detector, which used silicon strips to measure the radii of curvature of particles up to 110 cm from the z axis.

The pixel tracker was built from $\approx$1 m^2 of arrays of pixels, each covering 100 $\times$ 150 μm^2. In the barrel region ($0 < |\eta| < 1.2$), individual silicon detectors were assembled in three concentric cylindrical shells centered on the z axis. In the endcap region ($1.2 < |\eta| < 2.5$), two layers of pixel detectors were installed in a turbine pattern (Figure 3.2) [39]. These provided up to 3 measurements for every track, and primarily were used to reconstruct interaction vertices.

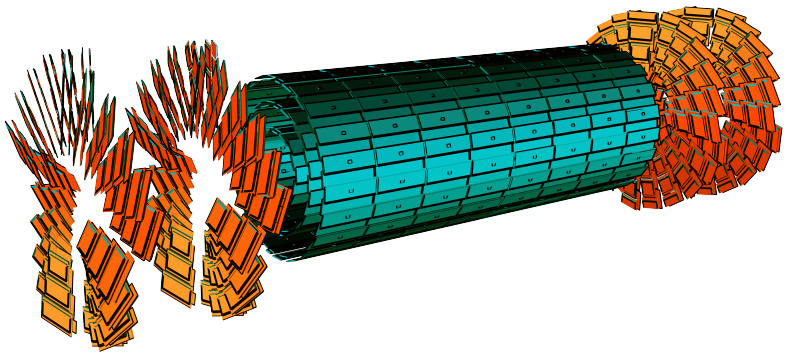

Figure 3.2: The barrel and endcap sections of the pixel detector.

Located outside the pixel tracker, the strip tracker was constructed with 198 m^2 of silicon divided into arrays of strips, and organized into the four structures that are shown in Figure 3.3 [40]. As the distance from the beam axis increased, the strip width increased from 80 to 180 μm, and the strip length increased from 12 to 16 cm. In the barrel region, silicon strips were used to build 10 concentric cylindrical shells. In the endcap region, silicon strips were arranged in 12 disks with some overlap in $|\eta|$ with the barrel region silicon strips. The strip tracker provided between 5 and 14 measurements for every track over a $\sim$1 meter distance.

Charged particles traversing the tracker generated signals in silicon detector modules that each had arrays of pixels or strips connected to Read-Out Chips (ROCs). In the pixel tracker, each ROC was connected to an array of 52 $\times$ 80 pixels. The pixel tracker barrel was built from silicon detector modules that each had 16 ROCs. In the pixel tracker endcap, each turbine blade was built from 7 silicon detector modules (4 on one

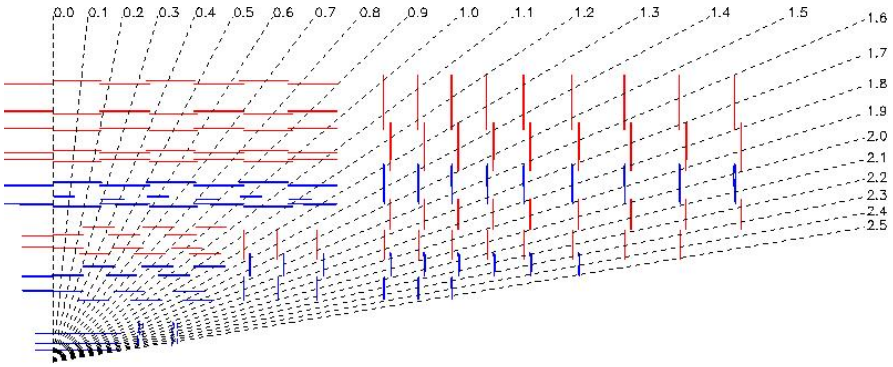

Figure 3.3: The barrel and endcap sections of the strip detector for $\eta \geq 0.$ and one quadrant of ϕ. The pixel detector is shown to scale in the bottom left corner.

face, 3 on the other), and each module had between 2 and 10 ROCs. In total, ∼16000 ROCs were connected to 66 million pixels. The strip tracker used a different type of ROC, and each ROC was connected to 128 strips located on the same η ring. Each ROC and its associated strips was one strip detector module, and the strip tracker was built from ∼15400 detector modules.

The tracker measured the positions and energies of charged particles at up to 17 points, and as far as 1.1 meters from the beam axis. The track reconstruction algorithms, described later, identified sets of track points as individual particle tracks. Along the trajectory of each track, the equation of motion of a charged particle in an inhomogenous magnetic field subject to ionization energy losses in silicon was solved numerically. The numerical solution was used to extract the particle's radius of curvature, and thereby its p_T.

The tracker performance depended on the number and momenta of the charged particles in a collision event. In events where two leptons and jets were reconstructed from tracks that pointed to one vertex, the vertex's position was measured with a resolution better than 12μm in any direction [41]. The tracker measured charged particle momenta by measuring the radius of curvature of charged particle tracks; thus the p_T

resolution degraded with increasing p_T. For muons with $20 < p_T < 100$ GeV, the tracker measured the p_T of barrel region muons with a resolution of 1.3% to 2.0%, and measured the p_T of endcap muons with a resolution of 6% or better [42]; higher p_T muons were measured with a worse p_T resolution. Charged hadrons that did not undergo a nuclear interaction in the tracker were measured with a p_T resolution similar that of a muon. Accounting for the η-dependent tracker material budget of 0.18 to 0.56 nuclear interaction lengths, the tracker measured the p_T of all charged hadrons with $10 < p_T < 100$ GeV with a resolution of 3.3% or better in the barrel, and 20% or better in the endcap [41]. Electrons were detectable as tracks if they had $p_T > 0.4$ GeV and $|\eta| < 2.5$, but their p_T resolution was significantly worse than that of charged hadrons or muons due to multiple scattering and bremsstrahlung. The tracker measured the p_T of electrons with $10 < p_T < 100$ GeV with a resolution of between 6% and 27% of p_T in the barrel, and between 20% and 50% of p_T in the endcap.

To measure the positions of the interaction vertices and charged particle momenta with these resolutions, the tracker alignment was measured before the start of data taking with cosmic ray muons. The alignment is the position of the silicon detector modules relative to the calorimeters and muon detectors. Knowing and calibrating the alignment is crucial because the momenta of charged particles and the positions of interaction vertices are extracted from track position measurements. During collisions, $Z \to \mu\mu$ events and cosmic ray muons were used to monitor and recalibrate the tracker alignment.

In the reconstruction, charged leptons and hadrons were distinguished from photons and neutral hadrons using tracks found in the tracker. Tracks that extrapolated to energy deposits found in the electromagnetic calorimeter (ECAL) or hadronic calorimeter (HCAL) were identified as electrons or charged hadrons, respectively. Tracks found in the silicon tracker that extrapolated to tracks found in the muon detectors were

identified as muons.

3.3 The Electromagnetic Calorimeter

Surrounding the silicon tracker was the electromagnetic calorimeter (ECAL), which detected photons, and distinguished electrons and positrons from other charged particles. The ECAL is a homogeneous absorption calorimeter built from scintillating lead-tungstate ($PbWO_4$) crystals. In response to incident photons and electrons ($e^{\pm}$), the ECAL crystals emitted visible light in ~20 ns in amounts proportional to the incident particle energies that was detected with avalanche photodiodes (APDs) and vacuum phototriodes (VPTs).

The ECAL contained 75848 crystals [43] divided into barrel and endcap regions. In the barrel region ($0 < |\eta| < 1.479$), 61200 crystals with ~26 radiation lengths[1] of $PbWO_4$ were arranged in a cylindrical shell. The scintillation light emitted in the barrel crystals was detected with APDs. The front face of each crystal measured 2.2 × 2.2 cm^2, and was 19 cm away from the outer most silicon tracker layer. In the endcap region ($1.479 < |\eta| < 3.0$), 14648 crystals (half in each endcap) with ~25 radiation lengths of $PbWO_4$ were installed in a disk. The scintillation light emitted in the endcap crystals was detected with VPTs. The front face of the endcap crystals measured 2.86 × 2.86 cm^2, and was located behind 3 radiation lengths of lead and silicon that constituted a preshower detector. The preshower detector is a sampling calorimeter built from two disks of lead absorber and two planes of silicon strips that cover $1.653 < |\eta| < 2.6$. The first disk is 2 radiation lengths thick, and the second is 1 radiation length thick. The back side of each disk is covered by arrays of silicon sensors that each cover 63 × 63 mm^2 and contain 32 individual strips. Each silicon sensor was connected to its own

[1] On average the energy of a relativistic $e^{\pm}$ decreases by e^{-1} after travelling through one radiation length of material.

Read-Out Chip (ROC), and groups of 7, 8, or 10 ROCs were organized into individual micromodules. The preshower detector improved the spatial and energy resolution with which electromagnetic showers were studied in the endcap. A partial view of the ECAL barrel, endcap and preshower detectors is shown in Figure 3.4 [44].

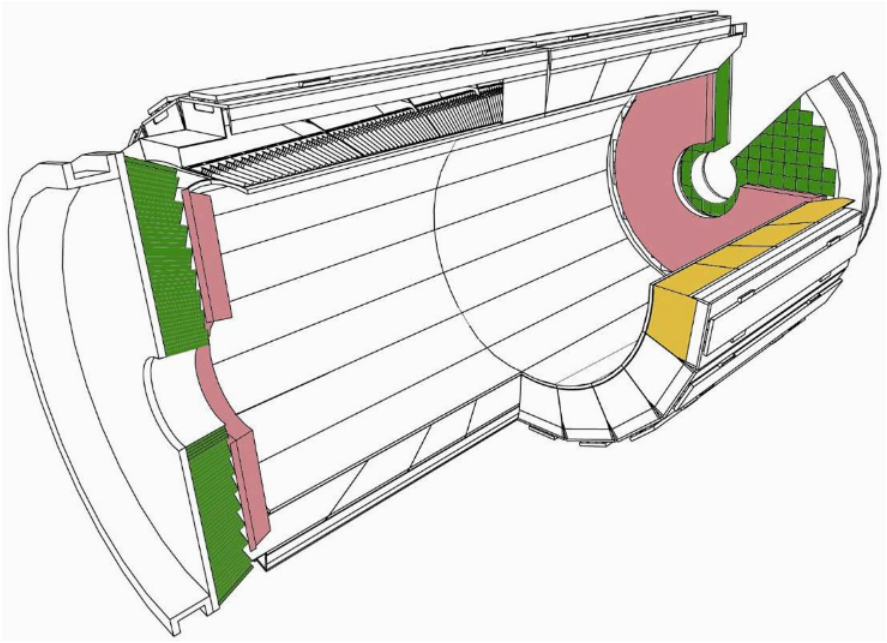

Figure 3.4: The ECAL barrel, endcap and preshower detectors.

The ECAL measured the energies of photons and electrons with $0 < |\eta| < 3.0$ by measuring the amount of scintillation light produced in clusters of crystals. The density of $PbWO_4$, 5.4 $\frac{gm}{cm^3}$, was sufficiently high that the signal of an electron or photon was usually fully contained in a 3×3 crystal cluster centered on the most energetic crystal. To estimate the energy lost through bremsstrahlung in the tracker, the signals of electrons and photons were measured in 3×5 crystal clusters or larger. Based on real collision data, the ECAL measured the energies of electrons from $Z \rightarrow ee$ decays ($E_T \approx 45$GeV) with a resolution better than 2% for $|\eta| < 0.8$, and between 2% and 5% elsewhere. At a slightly lower E_T scale in real collision data, the ECAL measured the

energies of photons from $Z \to \mu\mu\gamma$ decays with a resolution of 2.5% in the barrel, and 4.7% in the endcaps [43].

To measure photon and electron energies with similar precision across the entire detector, the ECAL crystals were monitored and calibrated during data taking using several techniques. Every 40 minutes each ECAL crystal was illuminated with light from blue and green lasers to monitor the crystal transparency. Every week laser data was used to calculate new crystal correction factors, which corrected the changes in crystal transparency since the previous week. Photons from $\eta \to \gamma\gamma$, and electrons from $W \to e\nu$ and $Z \to e^+e^-$ were used to validate the weekly transparency corrections.

To compliment the transparency corrections, additional corrections were applied to ECAL crystals to calibrate their responses based on the arrival times and energies of reconstructed particles. Relative energy and arrival time corrections for each crystal were calculated using methods described elsewhere [45], and were applied to normalize the the responses of all crystals, in terms of energy and time, to the same value. Then absolute energy scale corrections were derived using electrons from $Z \to e^+e^-$ events, and applied to calibrate each crystal's energy response to the true Z boson mass. New arrival time corrections were applied every month, and new energy corrections were applied once in September 2015.

In the reconstruction, energies measured by individual ECAL crystals were grouped into dynamically sized superclusters (SCs) with at least 15 crystals. The SC size was allowed to vary in η and ϕ to capture bremsstrahlung photons produced when $e^{\pm}$s traversed the silicon tracker. In the subset of SCs that were isolated from HCAL energy deposits, each $e^{\pm}$ was identified as a SC that geometrically matched a reconstructed track trajectory, and each photon was identified as a SC not matched to any track.

3.4 The Hadronic Calorimeter

Surrounding the ECAL was the hadronic calorimeter (HCAL), which detected charged and neutral hadrons. The HCAL is a sampling calorimeter constructed with 17 layers of 3.7 mm thick scintillating plastic tiles separated by 17 layers of 5 cm thick metal absorber plates. In the barrel region ($0 < |\eta| < 1.4$), absorber plates and scintillating tiles were organized into 2304 towers, each covering a 5×5 grid of ECAL barrel crystals. In the endcap region ($1.3 < |\eta| < 3.0$), absorber plates and scintillating tiles were assembled into 2304 towers (1152 per endcap), each covering a 5×5 grid of ECAL endcap crystals.

Hadrons that impinged on the HCAL showered in brass absorber layers, and in $\sim$10 ns produced scintillation light in the plastic tiles. Optical fibers transmitted the scintillation light to hybrid photodiodes, which measured the scintillation light to determine the energies of incident hadrons. The HCAL was used in combination with the tracker, ECAL, and muon detectors to measure the energy of jets. After calibrating the HCAL and the other sub-detectors, the energy of jets with $p_T > 40$GeV and $|\eta| < 1.3$ was measured with a resolution of 16% or better [46].

To measure hadron energies with similar precision across the whole detector, the amount of light measured in scintillating tile towers was monitored and calibrated before and during 2015 collisions. Before collisions, a cesium-137 source was lowered into the HCAL, and the amount of scintillation light produced by each tower was used to calibrate each tower's response. Once collisions began, a laser system monitored the efficiency of light transmission from the scintillator tiles to the photodetectors. From laser transparency data, relative calibrations were derived that normalized the energy response of all towers to the same level. The absolute energy calibration was determined in events where a jet recoiled off a photon, or a leptonically decaying Z boson. There, the absolute hadronic energy scale was calibrated relative to the electromagnetic or muonic energy scale derived from $Z \to \ell\ell$ and $Z \to \mu\mu\gamma$ events. Finally, the precision

of the absolute hadronic energy scale calibration was improved using dijet resonances like $W/Z \to jj$.

In the reconstruction, the energy measured by each HCAL tower was treated as the basic unit of HCAL energy. Each reconstructed hadron contained at least one HCAL energy deposit, and potentially one or more ECAL energy deposits. Reconstructed tracks that extrapolated to the (η, ϕ) positions of HCAL energies were identified as charged hadrons, while HCAL energies that did not match any track were identified as neutral hadrons.

3.5 The Muon Detectors

Interspersed among layers of the magnet iron return yoke were gas ionization chambers that were used to detect and measure the trajectories of muons. The muon detectors had a geometrical acceptance of $0 < |\eta| < 2.4$. Since the muon detectors were located 4.0 meters or further from the IP, the muon detectors also measured each muon's arrival time to identify the collision event that produced it.

The muon barrel and endcap sections, shown in Figure 3.5, used three types of gas ionization detectors to identify muons and to measure their kinematics. In the barrel region ($0 < |\eta| < 1.2$), drift tubes (DTs) and resistive plate chambers (RPCs) were used, while in the endcap region ($1.2 < |\eta| < 2.4$), RPCs and cathode strip chambers (CSCs) were used.

The DTs were organized into 5 wheels, each with 4 radial units called stations, and 12 ϕ segments per station that each covered 30 degrees in ϕ. Each DT chamber measured muon trajectories using a set of 4 DT planes measuring r-z coordinates[2] that were between two sets of DTs measuring r-ϕ coordinates. Each r-ϕ set had 4 DT planes, and the two sets were separated by 24 cm to increase the lever arm length that causes

[2]There were no r-z planes of drift tubes in the outermost station.

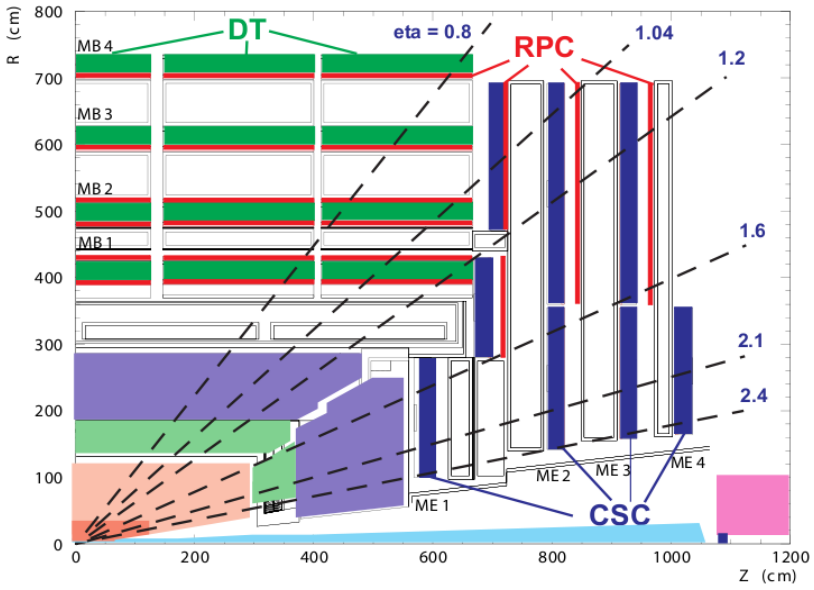

Figure 3.5: The barrel and endcap sections of the muon detectors for $\eta \geq 0.$ and one quadrant of ϕ. Shown between the muon detectors and the interaction point are the magnet solenoid and return yoke, the HCAL, the ECAL, and the silicon tracker.

muons to curve in the magnetic field. Based on collision data from 2015, each DT station measured muon trajectories with a resolution better than 300μm in any direction, and measured muon arrival times with a resolution of 2 ns [47].

In the endcap, CSCs were installed in four disks facing the interaction point. These disks were segmented into several radial layers (rings of different radii, stations), as shown in Figure 3.5, each containing 18 or 36 chambers, and each chamber had 6 planes of CSC detectors. Based on muon measurements made in 2015, the CSC chambers measured muon trajectories with a resolution better than 150 μm in any direction, and measured muon arrival times with a resolution of 3.2 ns [47].

In the barrel and endcap for $|\eta| < 1.9$, the RPCs measured muon arrival times with a resolution better than 2 ns. RPC measurements were used to identify the collision event that produced each muon [47].

By combining information from the tracker and the muon system, the p_T resolution of muons could be improved. Due to the 3.8 T magnetic field, the tracker measured muon momenta in the $p_T < 200$ GeV phase space with a resolution better than the muon detectors by a factor of 3 or more. As the muon p_T increased above 200 GeV, the muon momentum resolution reduced. However, since particle trajectories in the muon detectors were measured over 3 meters or more, the p_T of muons with a $p_T > 200$ GeV was measured with a better resolution than the tracker. Based on cosmic ray measurements made in 2015, the combined tracker and muon system measured the p_T of barrel region muons that had $200 < p_T < 400$GeV with a resolution ($\frac{\Delta p}{p_T}$) of 3.5% or better [47].

To measure the trajectories of tracks and muon momenta with these resolutions, the muon detector alignment was measured before the start of data taking with cosmic ray muons. Knowing and calibrating the alignment is crucial because the momenta of muons and their trajectories are extracted from track position measurements. During collisions, cosmic ray muons, and $W \to \mu\nu$ and $Z \to \mu\mu$ events were used to monitor and recalibrate the alignment of the muon detectors.

In the reconstruction, the tracks measured in individual ϕ segments of each muon station were treated as the basic building block of a muon. Each reconstructed muon contained one track from a muon station or one track from the silicon tracker, or both.

3.6 The Trigger System

In 2015 the rate of pp collision events delivered by the LHC was many orders of magnitude greater than the rate that CMS could store all the data. The LHC collided two proton bunches at a rate of 40 MHz, and in nearly every collision $\gtrsim$1 GeV of energy was detected in CMS. Due to the large cross section of QCD multijet processes and leptonically decaying heavy quark processes (Figure 3.6), there were $\sim 10^6$ collision events

per second with energetic charged leptons or hadronic jets. A two level event-selection trigger system was used to select events during collisions (online) that were stored for physics analyses.

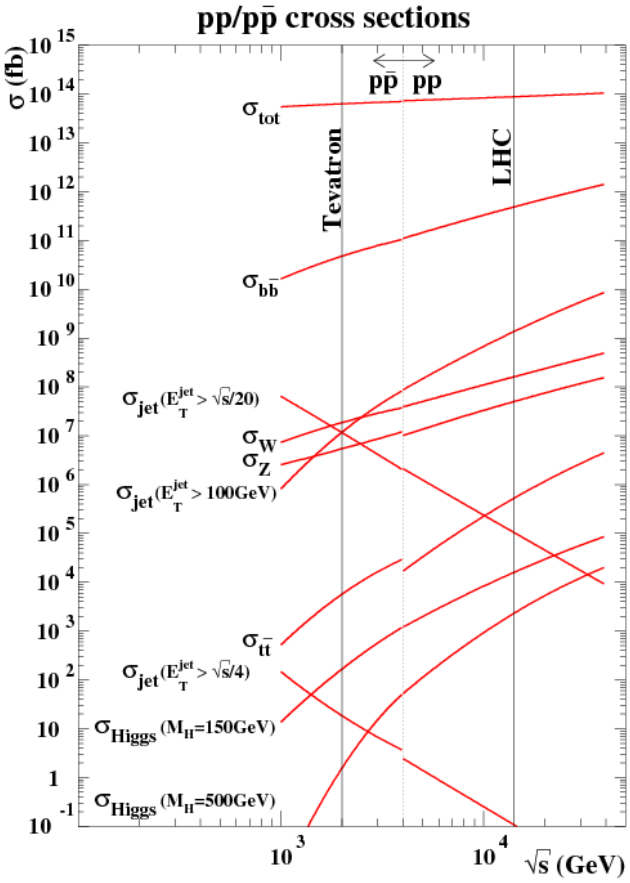

Figure 3.6: Production cross sections at the LHC and Tevatron as a function of center of mass energy. Each cross section divided by 10^5 yields the approximate production rate in events per second in 2015 at the LHC.

The Level-1 (L1) trigger system searched for collision events with photons, charged leptons, hadronic jets or missing energy. After every collision event, data from the ECAL, the HCAL and the muon detectors was used to identify energy clusters and build tracks that represented photons, hadrons, muons and other particles. In $\sim$1 μs these clusters and tracks, distinguished by (η, ϕ) trajectories and E_T (or p_T) values,

were built and sent to the L1 logic system located ∼20 m from CMS. Implemented in programmable hardware, the L1 logic system ran ∼200 algorithms in less than 1 μs, and selected events of interested based on clusters and tracks passing energy and $|\eta|$ selection criteria. Approximately 80000 events per second were passed to the second level trigger.

This High Level trigger (HLT) was used to select events to be stored for offline physics analyses or for detector calibration. The HLT began by transferring data from all sub-detectors to ∼13000 CPU cores running the HLT software [48]. A fast, simplified version of the full offline particle reconstruction software was run in small regions identified from the L1 trigger. Then, ∼400 different selection algorithms, running in parallel, applied selection criteria (E_T, $|\eta|$, etc) to locally reconstructed particles to select energetic photons, charged leptons, jets, and neutrinos. About 1000 events per second passed at least one selection algorithm, and the complete event was stored for subsequent reconstruction using the entire event information. The offline analysis of each event, the particle reconstruction algorithms, and the selection criteria are described in the next chapter.

Chapter 4

Event Reconstruction and Selection

W_R decays produce electrons, muons, and jets that generate signals in multiple sub-detectors (Figure 4.1). In the data analysis, offline selection criteria are applied to select events that have two jets and two leptons whose kinematics are consistent with those of the W_R progeny. The reconstruction algorithms, lepton triggers, and offline selection criteria are described in this section.

The same reconstruction algorithms and selection criteria were applied to simulated events to estimate the signal and the background. In this section, any difference in reconstruction and selection efficiency between data and simulated events is described.

4.1 Track Reconstruction

Muons and charged hadrons are reconstructed as helical tracks from signals measured in the silicon tracker and, in the case of muons, with the muon detectors. A reconstruction algorithm starts by reconstructing tracks from signals found in the innermost

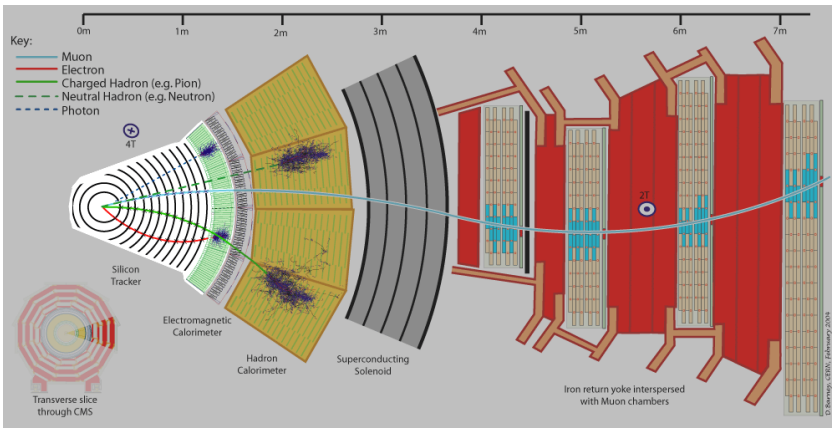

Figure 4.1: Typical trajectories of particles travelling through CMS, from CERN.

pixel tracker layer that were closest to the IP. After identifying track candidates in the innermost layer, the algorithm works radially outward, and builds longer track candidates by including new signals. Signals in successive layers are linked and identified as tracks using a Kalman filter that requires each additional track point's measured position to be consistent with the track trajectory within $\chi^2 < 30$ [41]. Each time a new position measurement is added to a track, all the track parameters are recalculated, and an analytic function extrapolates the track trajectory to the next layer assuming energy can be lost through multiple scattering and ionization in the silicon. Signals in the next layer are searched for in the region identified by this extrapolation. This procedure is repeated out to the outermost silicon strip tracker layer. Then, the same algorithm is applied in reverse - starting from the outermost strip layer and working inward - to identify track points that were missed and are compatible with an existing track. Then, the track points that are linked into tracks are removed from the list of track candidates, and the algorithm is restarted using signals measured in the innermost pixel tracker layer that were further from the IP. Using this algorithm, isolated muons with a $p_T > 0.9$ GeV and an $|\eta| < 2.4$ were reconstructed as tracks with essentially 100% efficiency [41]. After reconstructing all tracks in an event, each point where two

or more tracks originate is identified as an interaction vertex. A vertex is required to have at least two reconstructed tracks originating within 2 mm of the vertex position. The positions of vertices that have muon tracks with $|\eta| < 1.4$ and $p_T = 100$ GeV were measured with 10 and 30 μm resolutions in the transverse (r-ϕ) and longitudinal (z) directions.

Using a second track reconstruction algorithm, electrons are reconstructed as helical tracks from signals measured in the silicon tracker. This is necessary because the tracker contains 1 to 2 radiation lengths of material, causing electrons to shower and lose energy through bremsstrahlung. The electron track reconstruction algorithm uses the same iterative track reconstruction procedure described previously, but extrapolates each track's trajectory to the next silicon layer assuming the track loses energy through bremsstrahlung that is described by a sum of six Gaussians [49]. The Gaussian widths can be any positive value, but their total width must minimize the difference in the cumulative probability function of the predicted energy loss between the Bethe-Heitler formula and the six-Gaussian approximation. Also, the Kalman filter used to link signals in successive layers requires that additional signals need to have $\chi^2 < 2000$. Using the electron track reconstruction algorithm, electrons that had $p_T > 20$ GeV and were within $|\eta| < 2.5$ were reconstructed as tracks with an efficiency $\geq 97\%$ [50].

4.1.1 Muon Reconstruction

Muons are reconstructed as tracks from signals measured in individual muon chambers. In each DT chamber, the start and end points of track candidates are identified as pairs of track points measured in the same plane (r-ϕ or r-z) but in different layers. Then, straight lines representing the track candidates are drawn between the pairs of points, and candidates that do not project to the IP are discarded. The trajectories of these candidates are compared to the positions of all track points, and the points that overlap

with the candidate trajectories are merged with the candidates to build track segments that are measured in at least 3 layers. In each plane the track segment that is measured in the largest number of layers (N_{layer}) and has the lowest $\chi^2/nDOF$ (χ^2_{min}), less than 20, is used to build a 3D track. If there are two or more track segments in one plane with the same N_{layer} and χ^2_{min}, then all combinations of r-ϕ and r-z track segments are used to build tracks. In practice, only $\sim$1% of events have more than 1 track in a DT chamber [37]. The same track segment reconstruction algorithm is used in each of the six-layer, single plane CSCs. There, the final track segment is required to have signals in at least 4 layers. In the barrel-endcap transition region ($1.3 < |\eta| < 1.6$) where the DT chambers end and the CSCs begin, RPCs are used to improve the muon reconstruction efficiency and the precision of arrival time measurements. Each RPC contains two parallel plates divided into many thin strips, and strips that measure a signal are grouped into clusters. Each reconstructed cluster represents a hit whose position is the center of gravity of all the strips in the cluster.

Tracks in individual chambers are connected to reconstruct muon trajectories over several meters. A Kalman filter algorithm similar to the one used to reconstruct electron tracks starts with tracks in the chambers closest to the IP, and predicts the track positions in chambers in the next radial station with the effects of an inhomogeneous magnetic field and material losses taken into account [42]. Track segments in outer chambers are added to existing tracks subject to a χ^2 requirement, and existing tracks are propagated to the next radial station even if no matching track segment is found in the current station. Once the outermost station is included, a reverse Kalman filter is applied to reconstructed tracks from the outermost to the innermost station. The reverse Kalman filter is used to determine the final track parameters, and the resultant tracks are compared to tracks found in the silicon detector to identify muons.

Each silicon detector track that passes within 3 cm of a muon detector track is

identified as a muon. If a muon detector track has multiple silicon detector track candidates within 3 cm, the closest match is identified as a muon; and comparing the results of the silicon detector track and the muon detector track determines the (η, ϕ) trajectory of each muon.

As there are two independent detectors each measuring the muon's momentum, four different muon reconstruction algorithms are composed, and the highest quality result is selected. Each algorithm fits a continuous track [47] to a unique combination of silicon tracker and muon detector measurements to estimate a muon's trajectory, depicted in Figure 4.1. The quality of each continuous track is identified by a fit uncertainty $\chi^2/nDOF$ and momentum uncertainty $\sigma(p_T)/p_T$. The track with the lowest $\chi^2/nDOF$ and momentum uncertainty $\sigma(p_T)/p_T < 0.3$ determines the muon's momentum. For muons with $p_T \lesssim 100$ GeV the highest quality result is obtained using only silicon tracker measurements. Muons that had $|\eta| < 1.4$ and $p_T = 100$ GeV were measured with a p_T resolution of ~2.8% [41]. As a muon's p_T increases above 100 GeV the silicon tracker p_T resolution degrades faster that that of the muon detectors. A significant fraction of $W_R \to \mu\mu jj$ events are expected to produce at least one muon with $p_T > 200$ GeV (Table 4.1). In this high p_T region the highest quality momentum measurement comes from a combination of the silicon tracker and muon detector measurements, such that muons with $|\eta| < 0.9$ and $200 < p_T < 400$ GeV were measured with a p_T resolution of 3.2%; higher p_T muons were measured with a resolution better than 6% [47].

Table 4.1: Fraction of expected $W_R \to \mu\mu jj$ events that had at least one muon with $p_T > 200$ GeV. ($M_{N_l} = \frac{1}{2} M_{W_R}$)

M_{W_R} (TeV)	Fraction of events with at least one high-p_T muon (%)
1.0	80.
2.0	95.
3.0	98.

Muons produced in simulated events are reconstructed with a higher efficiency than

muons produced in real collisions. This efficiency difference was eliminated by multiplying the weight of each simulated event by a value between 0.99 (1% decrease) and 1.0, depending on the muon p_T and η, for each muon that was selected.

4.2 Energy Measurement

The energies of photons and electrons are measured in groups of ECAL crystals. Photons and electrons impinging on the ECAL generate signals in the ECAL crystals that are converted into uncalibrated energies. The most energetic crystals with $E_T \gtrsim 0.2$ GeV and their nearest neighbors are grouped into superclusters (SCs) that are at least 3 crystals wide in η. The upstream tracker material causes $\sim$35% of electrons and photons to shower early in the tracker [41], and the magnetic field spreads the shower over several crystals in ϕ. To capture the early shower energy, each SC is at least 5 crystals wide in ϕ, and can be much larger, as in Figure 4.2. Once a SC is built, the energy of each crystal in the SC is multiplied by a laser transparency correction, and relative and absolute energy calibration corrections. The sum of the calibrated crystal energies is the SC energy, and the energy weighted average (η, ϕ) position is the SC position. Using only ECAL SCs, the (η, ϕ) positions of electrons in the barrel (endcap) were measured with a ϕ resolution of 0.17° (0.29°), and an η resolution of 0.001 (0.002) units.

The energies of hadrons are measured over 10 nuclear interaction lengths of material, the first of which is the lead tungstate ECAL. Up to 25% of hadrons start showering in the tracker [41], so hadrons impinging on the ECAL are reconstructed as SCs like electrons and photons. Hadrons impinging on the HCAL generate signals in the HCAL towers that are converted into uncalibrated energies. The highest energy towers with $E_T \gtrsim 1$ GeV are used to seed tower clusters, which include all neighboring towers that have $E_T > 0.8$ GeV [51]. If one tower is grouped into multiple clusters, the tower's contribution to each cluster is weighted by its distance from each cluster's seed. After the

clusters are built, each tower's energy is multiplied by a laser transparency correction, and relative and absolute energy calibration corrections. The sum of the calibrated tower energies is the cluster energy, and the energy weighted average (η, ϕ) position is the cluster position. Combining ECAL and HCAL energy measurements, hadrons that have $E_T = 100$ GeV were measured with a resolution of 10% E_T [51].

4.2.1 Electron, Photon, and Hadron Reconstruction

A track is identified as being caused by an electron if it extrapolates from the outermost silicon strip layer to the front face of the ECAL, and matches a shower found at that location, represented by an ECAL SC. If a track matches the (η, ϕ) position of a SC to within 1.0° (1 crystal wide) in ϕ and within 0.004 units (below $\frac{1}{2}$ a crystal wide) in η, then the track and ECAL SC are identified as an electron candidate. If the measured E_T and the matched track p_T agree within the track p_T uncertainty, then the track and shower are identified as being caused by an electron. Using the SC energy, electrons with $E_T \approx 45$ GeV and $|\eta| < 0.8$ were measured with an E_T resolution better than 2%, and a resolution between 2% and 5% at higher values of $|\eta|$ [43].

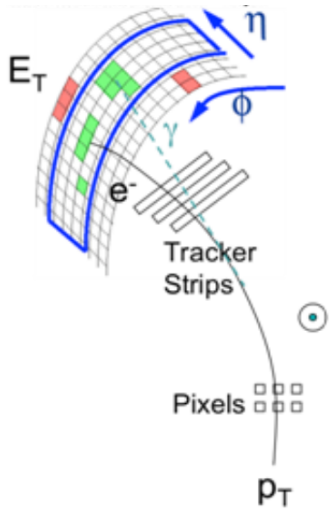

Figure 4.2: The trajectory of a typical electron through the tracker and the ECAL.

Electrons produced in simulated events are reconstructed with a higher efficiency than electrons produced in real collisions. This efficiency difference was eliminated by multiplying the weight of each simulated event by 0.982 for each electron that was selected.

After electrons have been identified, ECAL SCs are identified as being caused by photons using the remaining reconstructed tracks. A SC that does not match any reconstructed track within the matching window ($\Delta\eta = 0.004$ units, $\Delta\phi = 1.0°$) is identified as a photon. Alternatively, an ECAL shower that matches a reconstructed track within the matching window is identified as a photon if its E_T does not agree with the track p_T within the uncertainty of the measurement of the track p_T.

A reconstructed track is identified as being caused by a charged hadron using the calorimeter energy clusters. A track that is not identified as an electron is extrapolated from the outermost silicon strip layer to the HCAL front face, and its (η, ϕ) position is compared to that of the HCAL clusters. If a track intersects any portion of an HCAL cluster, and the cluster E_T and track p_T agree within the E_T uncertainty, then the track is identified as being caused by a charged hadron. The track p_T and (η, ϕ) determine the charged hadron kinematics.

After all charged tracks have been identified as leptons or hadrons, an HCAL cluster that is not intersected by a track is identified as a neutral hadron. Also, an HCAL cluster that is intersected by a track is identified as a neutral hadron if its E_T does not agree with the track p_T within the uncertainty of the measurement of the E_T. If an ECAL SC (energy E_{ECAL}, uncertainty δE_{ECAL}) overlaps with any portion of an HCAL cluster (energy E_{HCAL}, uncertainty δE_{HCAL}) identified as being caused by a neutral hadron, then the SC can be identified as coming from a neutral hadron. The SC is identified as a neutral hadron if E_{ECAL} and E_{HCAL} agree within the larger of the two uncertainties δE_{ECAL} and δE_{HCAL}. The E_T and (η, ϕ) trajectory of each neutral

hadron is determined by the calorimeter E_Ts, and the E_T-weighted average cluster position relative to the IP.

4.2.2 Jet Reconstruction

Quarks and gluons emitted from pp interactions produced jets of photons, hadrons and leptons. On average, 85% of a jet's energy is carried by charged particles and photons [52], so during jet reconstruction these particles are reconstructed first. The particle flow jet reconstruction algorithm [51] identifies (η, ϕ) regions with one or more silicon tracker or muon detector tracks, one or more HCAL clusters, and any number of ECAL SCs. In these regions, algorithms described previously are used to reconstruct muons first, followed by electrons and photons and charged hadrons, then neutral hadrons. After all tracks and energy clusters in a region are identified as specific particles, a jet, represented by the cone in Figure 4.3, is reconstructed from those particles.

Due to the high instantaneous collision luminosity, each pp bunch crossing delivered by the LHC produces multiple pp interactions, or pileup (PU) interactions, that make jet reconstruction more challenging. In every unit of η-ϕ, each PU interaction adds $\sim$11 charged particle tracks with $p_T \approx 0.5$ GeV to the event [53]. These tracks are primarily charged hadrons, so before jets are reconstructed the charged hadrons associated with PU interaction vertices are removed from all jet reconstruction regions. Jets are then reconstructed as clusters of particles using the anti-k_T algorithm [54] with a distance parameter $R = 0.4$. The anti-k_T algorithm starts with the highest p_T particle and adds other particles to the jet based on their p_T and distance from the jet axis. Using the distance parameter $R = 0.4$, particles located $\Delta R > 0.4$ from the jet axis are less likely to be clustered into the jet than particles located within $\Delta R \leq 0.4$. Once jets are reconstructed, a second set of smaller jets are reconstructed to estimate the average increase in jet energy due to neutral particles produced in PU interactions. The second

set of jets are reconstructed as clusters of particles using the k_T algorithm [55, 56, 57] with distance parameter $R = 0.3$. The k_T algorithm builds a jet starting with the lowest p_T particle and adds higher p_T particles to the jet based on their p_T and distance from the jet axis. Then, the p_T of each jet reconstructed with the k_T algorithm is divided by its area $A = \eta \times \phi$ (p_{Tj}/A_j), and the median value ρ is the average neutral particle energy density in the event [58, 59]. The neutral particles produced by each PU interaction increase ρ by about 0.5 GeV per unit of η-ϕ [46]. Using the hybrid jet area subtraction technique described in [52], the energy of photons and neutral hadrons found in each jet reconstructed with the anti-k_T algorithm are reduced by multiplying ρ by the jet's area and an η dependent factor. After the area based subtraction, jet energies are calibrated to correct for known η and p_T variations of the detector's response to jets. After calibrations, particle flow jets with a $p_T > 40$ GeV and an $|\eta| < 1.3$ were measured with a resolution of 16% of p_T or better [46].

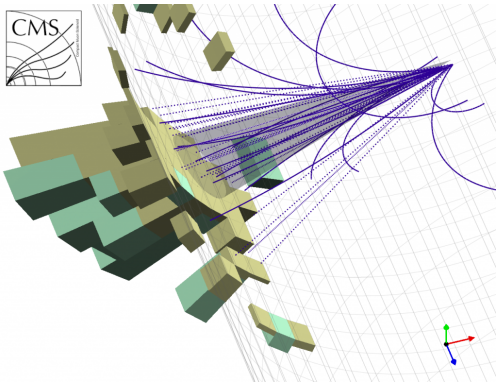

Figure 4.3: A cone of reconstructed particles reconstructed as a jet, with the reconstructed vertex on the right. From the CMS Experiment.

4.3 Trigger and Offline Selection Criteria

During collisions, in the high-level trigger the electron, muon, and HCAL cluster reconstruction algorithms are used to reconstruct electrons and muons. Then, trigger selection criteria are applied to select events that have two electrons or one muon that is isolated from other particles and has a large transverse energy: $p_T > 50$ GeV for a muon, and $E_T > 33$ GeV for both electrons. Offline, particles in each event are reconstructed using information from the entire detector, and then additional selection criteria are applied to the reconstructed leptons and jets. Events that met the selection criteria, described in detail in Appendix B, had two same flavor leptons and at least two jets with the following characteristics:

Electrons

- The E_T of each electron was equal to the energy of its SC measured in the ECAL.
- Each electron had an $E_T > 33$ GeV, and an $|\eta| < 1.44$ or an $|\eta| > 1.57$.
- The majority of each electron's energy in the ECAL was measured in a region that was 2 crystals wide in η.
- Each electron was promptly produced, and was not reconstructed near other particles.
- The track of each electron was reconstructed from multiple high quality measurements made in the tracker.

Muons

- Each muon had an $|\eta| < 2.4$, and at least one muon had a $p_T > 50$ GeV.

- Each muon was promptly produced, and was not reconstructed near other charged particles.
- Each muon was reconstructed from multiple high quality measurements made in the tracker and the muon detectors.

Jets

- Each jet had at least two particles, and at least one was a charged hadron.
- Less than 90% of the total energy of each jet came from neutral hadrons.
- Less than 90% of the total energy of each jet came from photons.
- Less than 99% of the total energy of each jet came from electrons.

Leptons reconstructed in simulated events passed the trigger and offline selection criteria with a different efficiency than leptons reconstructed in data events. This efficiency difference was eliminated by multiplying the weight of each selected simulated event by 0.989 for each electron, by a p_T,η-dependent value between 0.99 and 1.0 for each muon, and by an additional p_T,η- dependent value between 0.95 and 1.04 for the muon that passed the trigger selection criteria.

4.4 W_R Kinematics and Offline Kinematic Selection Criteria

The trigger and offline selection criteria described previously were used to select events where two leptons and jets are identified. These selection criteria were also used in other searches for heavy particles that decay to leptons and jets [60], and were not specifically optimized for this analysis.

Having selected events for this search, the leptons and jets were required to pass additional selection criteria that were motivated by the kinematics of the W_R progeny. The heavy W_R decays through a lighter N_l to two leptons and two jets according to the following decay chain:

$$W_R \to N_l \ell_1; \quad N_l \to \ell_2 jj \tag{4.1}$$

Since the W_R and N_l are assumed to couple to leptons and quarks with the same strengths as the W, the W_R and N_l decay promptly to leptons and quarks that hadronize into jets. The kinematics of these particles are governed by the W_R mass and the ratio M_{N_l}/M_{W_R}.

Since the W_R mass is expected to be several TeV the W_R has low net momentum, and its progeny N_l and ℓ_1 are emitted isotropically in the lab frame. As a result, the ℓ_1 and the N_l progeny are primarily emitted in the region $|\eta| < 2.4$, as shown in Figure 4.4. Therefore, both reconstructed leptons and jets were required to have an $|\eta| < 2.4$.

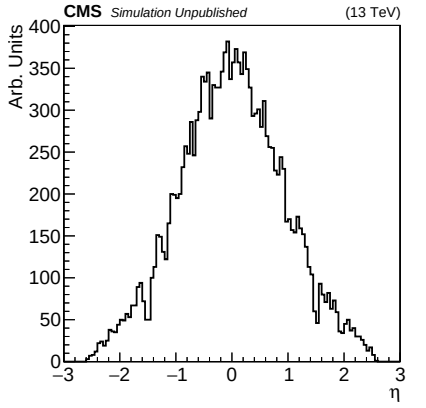

(a) ℓ from $W_R \to \ell N_l$

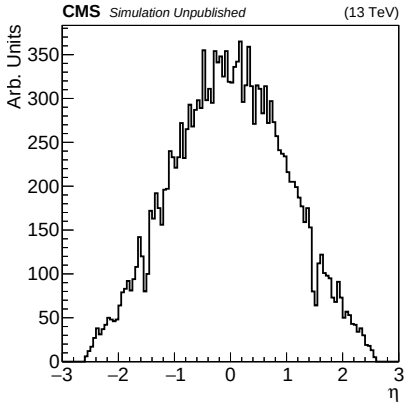

(b) ℓ from $N_l \to \ell jj$

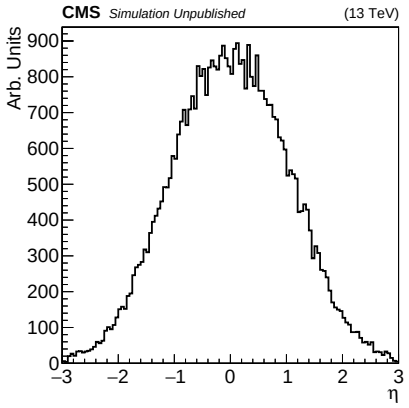

(c) jet from $N_l \to \ell jj$

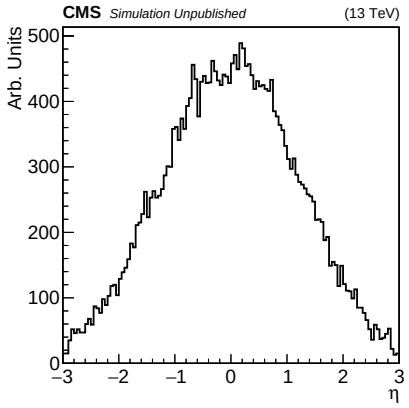

(d) jet from $N_l \to \ell jj$

Figure 4.4: The η distributions of leptons and jets reconstructed in $W_R \to \ell\ell jj$ events with $M_{W_R} = 2.2$ TeV and $M_{N_l} = \frac{1}{2} M_{W_R}$.

In the decay $N_l \to \ell_2 q_1 q_2$, the ratio M_{N_l}/M_{W_R} affects the separation between the lepton and the two quarks, $\Delta R(\ell, q)$. As M_{N_l}/M_{W_R} decreases from 1 to 0 the N_l momentum magnitude increases, as shown in Figure 4.5; this momentum boosts the N_l progeny along the N_l trajectory in the lab frame. As M_{N_l}/M_{W_R} decreases this boost increases, causing the $\Delta R(\ell, q)$ separation between the ℓ_2 and both quarks to decrease, as shown in Figure 4.6. Since the lepton reconstructed from ℓ_2 can also be reconstructed as part of a jet, as $\Delta R(\ell, q)$ decreases the it becomes more likely that a jet is reconstructed from ℓ_2 and either q_1 or q_2, and passes the selection criteria. In addition, there is a low probability, independent of M_{N_l}/M_{W_R}, that the lepton produced in the decay $W_R \to \ell_1 N_l$ is emitted in the vicinity of q_1 or q_2, and ℓ_1 and one quark are reconstructed as a jet that passes the selection criteria. To avoid selecting jets that are reconstructed from combinations of ℓ_1 or ℓ_2 and q_1 or q_2, each jet was required to be separated from each selected lepton by $\Delta R > 0.4$.

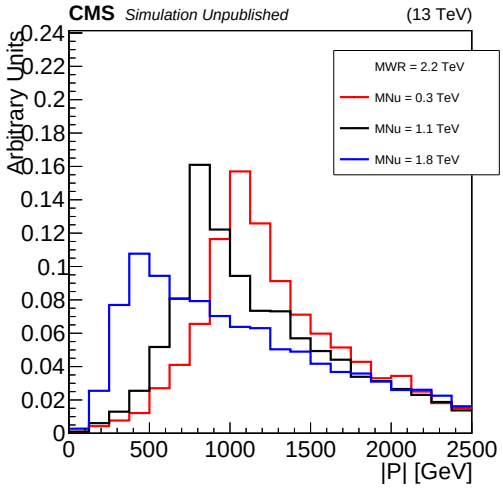

Figure 4.5: The $|p|$ distribution of the N_l produced in $W_R \to \ell N_l$ events with $M_{W_R} = 2.2$ TeV and different M_{N_l}.

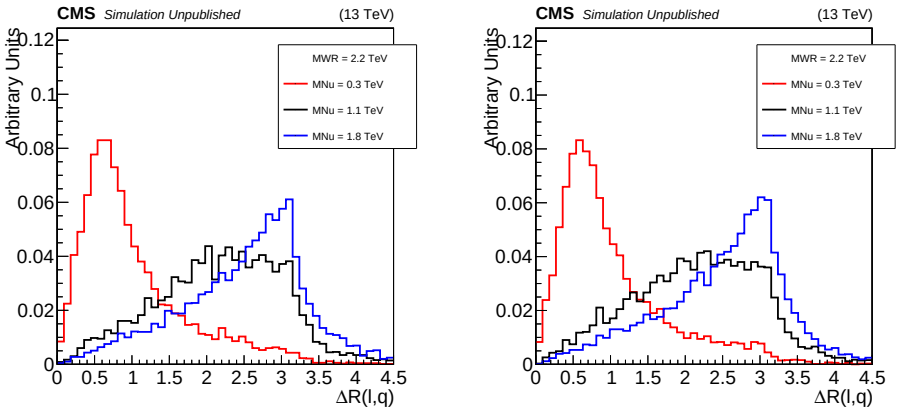

Figure 4.6: The $\Delta R(\ell, q)$ separation distributions between the ℓ and both quarks produced in $N_l \to \ell qq$ in $W_R \to \ell\ell qq$ events with $M_{W_R} = 2.2$ TeV and different M_{N_l}.

The leptons and jets produced in the W_R decay have p_T that are affected by the W_R mass and the ratio M_{N_l}/M_{W_R}. The W_R mass represents the total momentum that is distributed amongst the leptons and jets, so the lepton and jet p_T grow with the W_R mass. For $M_{W_R} = 2.2$ TeV and $M_{N_l} = 1.1$ TeV, the average p_T of reconstructed leptons and jets is above 60 GeV, as shown in Figure 4.7. As M_{N_l}/M_{W_R} increases to 1 the p_T of N_l progeny increase, and the p_T of the other lepton decreases, as shown in Figure 4.8. Similarly, as M_{N_l}/M_{W_R} decreases to 0 the p_T of both jets decrease, and the p_T of one lepton increases while the p_T of the other lepton decreases.

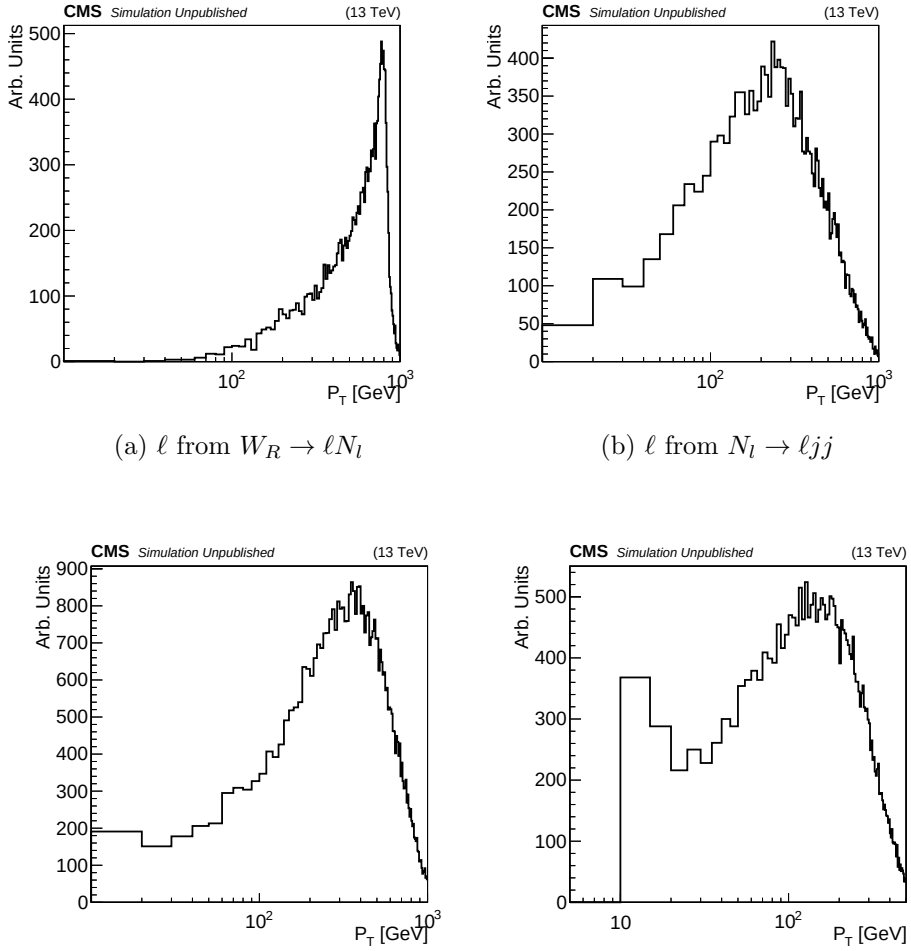

(a) ℓ from $W_R \to \ell N_l$

(b) ℓ from $N_l \to \ell jj$

(c) jet from $N_l \to \ell jj$

(d) jet from $N_l \to \ell jj$

Figure 4.7: The p_T distributions of leptons and jets reconstructed in $W_R \to \ell\ell jj$ events with $M_{W_R} = 2.2$ TeV and $M_{N_l} = \frac{1}{2} M_{W_R}$.

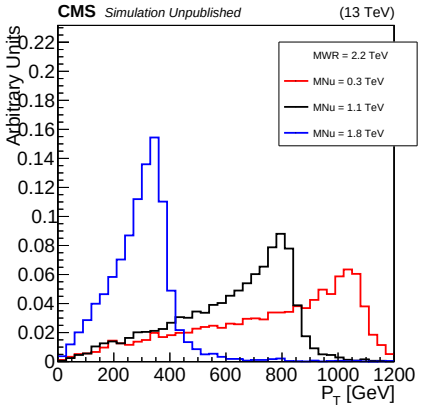

(a) ℓ from $W_R \to \ell N_l$

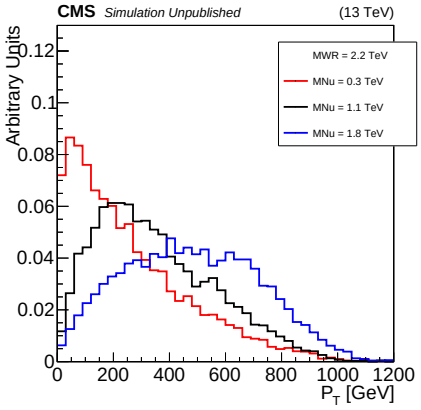

(b) ℓ from $N_l \to \ell qq$

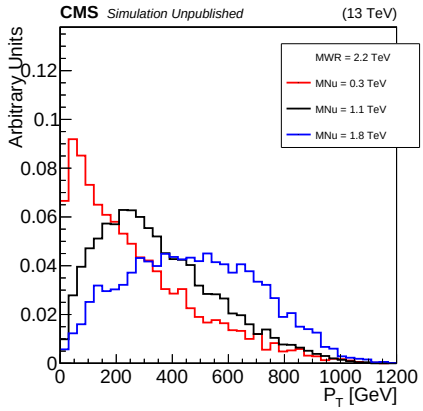

(c) quark from $N_l \to \ell qq$

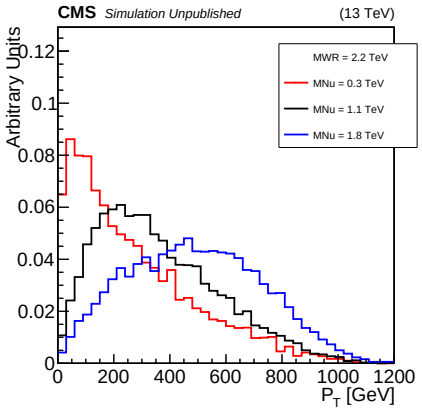

(d) quark from $N_l \to \ell qq$

Figure 4.8: The p_T distributions of leptons and quarks produced in $W_R \to \ell\ell qq$ events with $M_{W_R} = 2.2$ TeV and different M_{N_l}.

Based on these kinematics, one reconstructed lepton was required to have $p_T > 60$ GeV, and the other p_T selection criteria were set as low as possible to increase sensitivity to W_R signals with low M_{N_l}/M_{W_R}. The jet p_T requirement was set based on the decrease in jet p_T resolution with jet p_T. For reconstructed jets that were measured in the region $|\eta| < 1.3$, the jet p_T resolution was 16% of p_T or better for $p_T > 40$ GeV, and ∼21% of p_T for $30 < p_T < 40$ GeV [46]. The two selected jets were required to have $p_T > 40$ GeV to avoid selecting low p_T jets that were measured with poor p_T resolution. The p_T selection criterion applied to the lower p_T reconstructed lepton was set based on the lepton trigger selection efficiency. These efficiencies as a function of reconstructed muon and electron p_T, shown in Figure 4.9, are constant for $p_T > 53$ GeV, so the second reconstructed lepton was required to have $p_T > 53$ GeV.

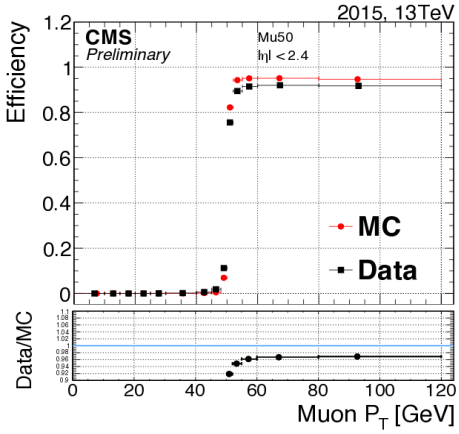

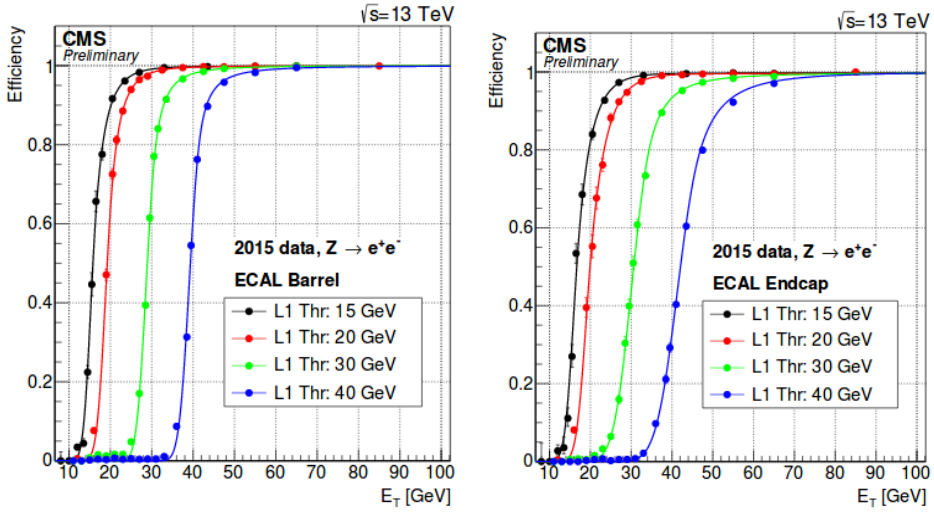

Figure 4.9: The muon and electron trigger efficiencies as a function of p_T or E_T in $Z \to \ell\ell$ events.

The invariant mass of the two leptons ($M_{\ell\ell}$), given by Equation 4.2, is affected by the W_R mass and the ratio M_{N_l}/M_{W_R}. As the W_R mass increases the p_T of both leptons also increase, thus increasing the $M_{\ell\ell}$. At a fixed W_R mass, increasing the ratio M_{N_l}/M_{W_R} causes the $M_{\ell\ell}$ to decrease. In the decay $W_R \to \ell_1 N_l$, the N_l always recoils against ℓ_1. As M_{N_l}/M_{W_R} decreases to 0 the ℓ_2 from the decay $N_l \to \ell_2 jj$ is increasingly boosted along the N_l direction of momentum, and opposite to the ℓ_1 direction of momentum. Therefore, as M_{N_l}/M_{W_R} decreases the angle θ_{12} between the two leptons, shown in Figure 4.10, increases, and the $M_{\ell\ell}$ increases, as shown in Figure 4.11. Based on the large expected W_R mass, the two reconstructed leptons were required to have $M_{\ell\ell} > 200$ GeV. The $M_{\ell\ell}$ threshold was not increased because it would reduce sensitivity to W_R signals with M_{N_l}/M_{W_R} ~1; the threshold was not lowered because it would increase backgrounds, especially from Drell-Yan +jets production, without a corresponding increase in the signal.

$$M_{\ell\ell} = \sqrt{2|p_1||p_2|(1 - \cos(\theta_{12}))} \tag{4.2}$$

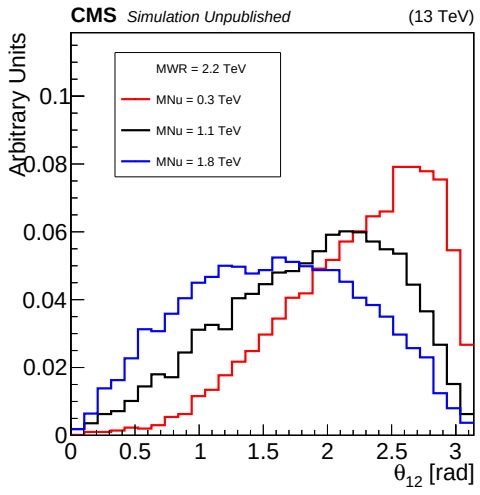

Figure 4.10: The distribution of the angle θ_{12} between the two leptons produced in $W_R \to \ell_1 \ell_2 qq$ events with $M_{W_R} = 2.2$ TeV and different M_{N_l}.

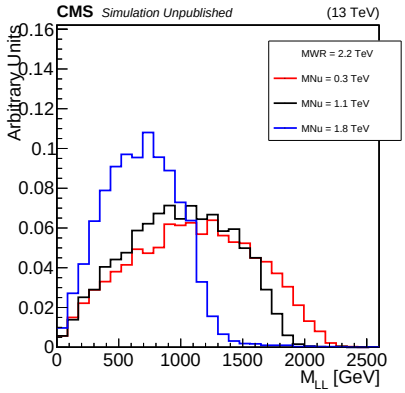

Figure 4.11: The $M_{\ell\ell}$ distribution of the two leptons produced in $W_R \to \ell\ell qq$ events with $M_{W_R} = 2.2$ TeV and different M_{N_l}.

In selected events, if more than two jets passed the selection criteria described previously, the two highest p_T jets were selected.

Applying the full selection criteria to simulated ST background events created a peak in the $M_{\ell\ell jj}$ distribution near 500 GeV, as shown in Figure 4.12. To avoid this peak, each event was required to have $M_{\ell\ell jj} > 600$ GeV.

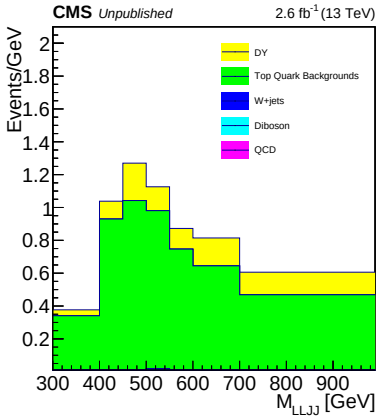

Figure 4.12: The $M_{\ell\ell jj}$ distribution in simulated background events after applying the event selection.

The offline kinematic selection criteria, listed in Table 4.2, were developed to select $W_R \to \ell\ell jj$ events over a large range of M_{W_R} and M_{N_l} values with the highest possible efficiency. The efficiency of the event selection, including trigger selection criteria, in signal events was estimated by simulating $pp \to W_R \to \ell\ell jj$ interactions, and applying the event selection to those events. The PYTHIA8 MC generator implements a flexible, generic W_R signal model that captures the main characteristics of theoretical models discussed in the literature [21, 22, 23, 24, 25, 29], so PYTHIA8 was used to simulate $W_R \to \ell\ell jj$ events with different values of M_{W_R} and M_{N_l}. The event selection efficiency was calculated using 50000 event datasets produced with $M_{N_l} = \frac{1}{2}M_{W_R}$ and M_{W_R} stepping from 0.8 to 6.0 TeV in increments of 0.2 TeV. The event selection efficiency, shown in Figure 4.13, exceeded 50% in the ee-channel, and 70% in the $\mu\mu$-channel. The efficiency is lower in the ee-channel due to the gap in ECAL coverage for $1.44 < |\eta| < 1.57$, and the lower efficiency offline ID criteria applied to electrons relative to muons.

Table 4.2: The kinematic selection criteria applied to reconstructed leptons and jets. The criteria were applied in the order that they are listed.

parameter	threshold
lead jet p_T, η	$p_T > 40\text{GeV}, \lvert\eta\rvert < 2.4$
sublead jet p_T, η	$p_T > 40\text{GeV}, \lvert\eta\rvert < 2.4$
lead ℓ p_T, η	$p_T > 60\text{GeV}, \lvert\eta\rvert < 2.4$
sublead ℓ p_T, η	$p_T > 53\text{GeV}, \lvert\eta\rvert < 2.4$
$\Delta R(\ell, j)$	> 0.4
$M_{\ell\ell}$	$> 200\text{GeV}$
$M_{\ell\ell jj}$	$> 600\text{GeV}$

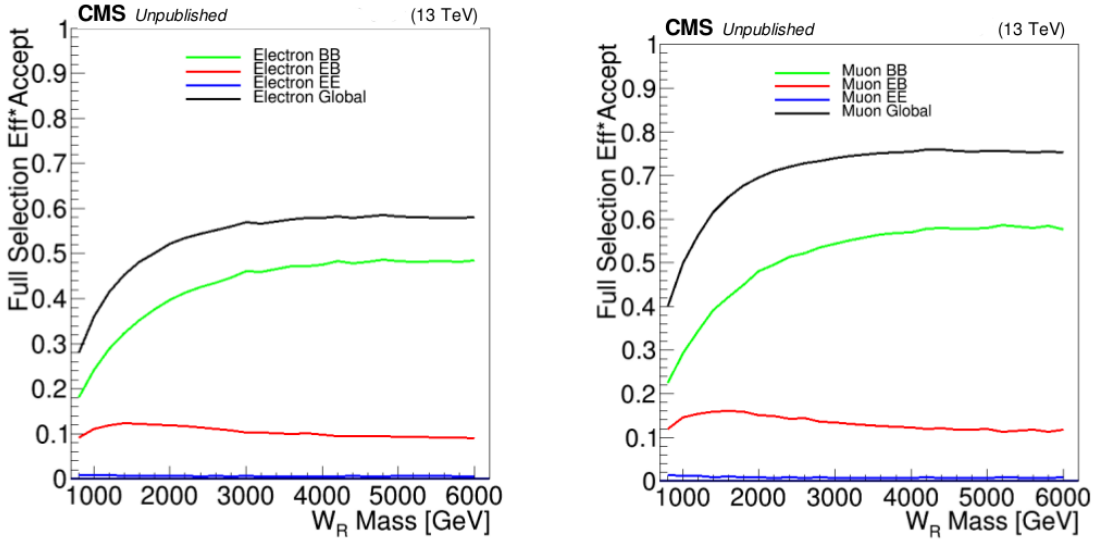

Figure 4.13: The event selection efficiency in simulated $W_R \to \ell\ell jj$ events, in the ee-channel (left) and the $\mu\mu$-channel (right). Different curves represent events where both leptons are in the barrel (BB), one is in the endcap (EB), or both are in the endcap (EE).

At a specific W_R mass, only the offline kinematic selection efficiency varied by more than a few percent over the entire M_{N_l} range. The variation in this selection efficiency as a function of M_{N_l} was calculated using 10000 event datasets produced with M_{W_R} increasing from 0.8 to 4.0 TeV in increments of 0.1 TeV. At each W_R mass, 10000 events were produced at each value of M_{N_l} starting at 100 GeV and increasing to M_{W_R} in increments of 0.1 TeV or less. The maximum variation in the kinematic selection efficiency as a function of M_{N_l}, shown in Figure 4.14, increased with M_{W_R}: up to 30% for $M_{W_R} \leq 1.3$ TeV, and up to 70% for $M_{W_R} \geq 2.5$ TeV. At a specific W_R mass, the kinematic selection efficiency is maximized or nearly so when $M_{N_l} = \frac{1}{2}M_{W_R}$.

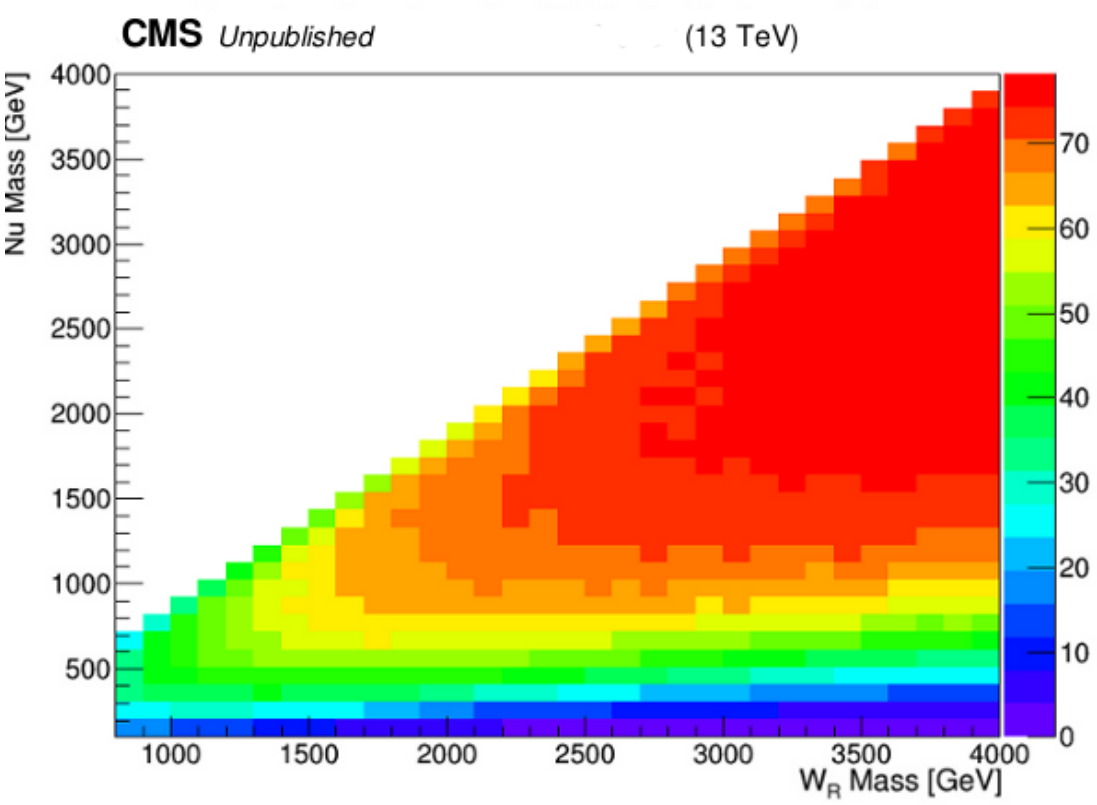

Figure 4.14: The offline kinematic selection efficiency (%) in $W_R \to \ell\ell jj$ events as a function of M_{W_R} and M_{N_l}.

4.5 Reconstruction and Event Selection Summary

Electrons, muons and jets expected from W_R and N_l decays are reconstructed from signals measured in CMS sub-detectors using dedicated reconstruction algorithms. These algorithms reconstruct leptons, hadrons and jets with high efficiency by using minimal selection criteria, and occasionally ($\sim$1-3%) reconstruct individual particles and jets incorrectly. The contribution of incorrectly reconstructed particles to $\ell\ell jj$ events was reduced by selecting events using lepton triggers and requiring that leptons and jets were reconstructed from high quality measurements. Selected particles were then required to pass kinematic selection criteria to identify particles whose kinematics are consistent with the W_R progeny. After applying the event selection to the data, the selected events were used to make a $M_{\ell\ell jj}$ distribution. The decay $W_R \to \ell\ell jj$ transfers all energy of the W_R into the invariant mass of the leptons and jets, so evidence of a W_R, independent of M_{N_l}, was searched for as an excess of data events above the predicted background in the $M_{\ell\ell jj}$ distribution. The contribution of background processes to the $M_{\ell\ell jj}$ distribution found in the data was predicted using procedures described in the next chapter.

Chapter 5

Background Estimation

As discussed in the previous chapter, the event selection criteria were applied to the data to select events where two leptons and jets were reconstructed, and had kinematics consistent with the W_R decay progeny. However, these criteria also selected data events produced by ST background interactions, like Drell-Yan +jets. The contributions of ST backgrounds to the $M_{\ell\ell jj}$ distribution found in the data were predicted using Monte Carlo (MC) simulations and control regions with no W_R signal contamination. The magnitudes of the individual backgrounds, how the backgrounds were simulated, and how the control regions were defined and used is described in this chapter.

The magnitude of the background produced by each ST process is proportional to the product of the cross section and branching ratio to $\ell\ell jj$ final states at $\sqrt{s} = 13$ TeV. The production of jets in association with the Drell-Yan process, and the production of top quarks yielded backgrounds with the largest magnitudes. The production of diboson (WW, WZ, ZZ) pairs, single W bosons in association with jets, and multiple jets through QCD also yielded backgrounds, but with significantly lower magnitudes.

The Drell-Yan process is initiated by a quark and anti-quark that annihilate into a Z/γ^*, which decays promptly into two opposite charge, same flavor leptons, as shown

in Figure 5.1. The production of dilepton pairs through Drell-Yan has a cross section-branching ratio product that peaks at 6000 pb for dilepton mass $M_{\ell\ell} \approx 90$ GeV, and decreases for higher values of $M_{\ell\ell}$. At $\sqrt{s} = 13$ TeV the quarks that initiate the Drell-Yan interaction radiate two partons with a probability of ∼0.01, equal to the QCD coupling squared α^2_{QCD}. Therefore, in ∼1% of Drell-Yan events two partons are radiated and hadronize into jets; the Drell-Yan process produces $\ell\ell jj$ final states with a cross section-branching ratio product of ≈60 pb.

Unlike Drell-Yan, the production of $t\bar{t}$ quark pairs, shown in Figure 5.2, produces $\ell\ell jj$ final states without initial state parton radiation. The product of the cross section and branching ratio, 86 pb, is similar to the product of the cross section and branching ratio of the Drell-Yan +2 jets process. Since more than 99% of top quarks decay to a W boson and bottom quark, the production of single top quarks with a W boson (Figure 5.3) yields two leptons and one jet when both W bosons decay leptonically. The gluon that initiates the top+W interaction radiates a gluon with ∼100% probability, so the production of top+W yields two lepton and two jet final states with a cross section-branching ratio product of ∼7 pb. The production of single top quarks through other processes, shown in Figure 5.3, yield only one W, and therefore do not produce $\ell\ell jj$ final states at leading order in the electroweak coupling.

The only other processes that produce two leptons and jets without initial state parton radiation are the production of WZ and ZZ pairs. The WZ production yields two leptons and jets when the W decays hadronically, and the Z decays to charged leptons. The ZZ process produces two leptons and jets when one Z decays hadronically, and the other decays to charged leptons. The combined product of the cross section and branching rato of the WZ and ZZ processes to $\ell\ell jj$ final states is ∼3 pb, negligible compared to the production of top quarks.

Other processes contributed to the total background, but at negligible levels. The

production of WW boson pairs yields two charged leptons when both W bosons decay leptonically. The two quarks that initiate the WW process radiate two partons with $\sim$1% probability, so the WW process produces $\ell\ell jj$ final states with a cross section-branching ratio product of $\sim$0.1 pb, negligible compared to other backgrounds. Although the W+jets and QCD multi-jet processes do not produce $\ell\ell$ final states at leading order in the electroweak coupling, a small fraction of their jets, less than 0.1%, are incorrectly reconstructed as charged leptons. Since the W+jets and QCD multi-jet processes produce multiple jets with cross section-branching ratio products in excess of several hundred pb [61, 62], they contributed to the $M_{\ell\ell jj}$ distribution found in data, but at a negligible level.

In conclusion, the Drell-Yan +jets and top quark processes produced the largest backgrounds, and other processes produced significantly smaller backgrounds. The shape and magnitude of the $M_{\ell\ell jj}$ distribution produced by these processes was estimated using Monte Carlo (MC) simulations.

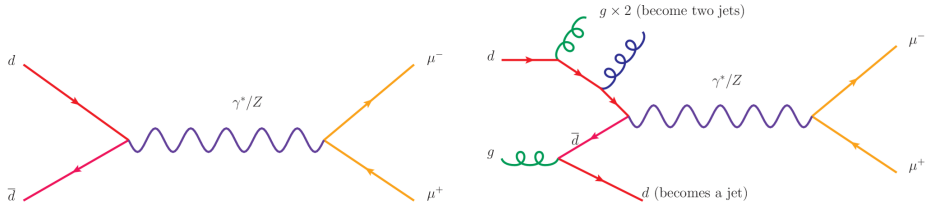

Figure 5.1: Feynman diagrams for the Drell-Yan interaction with 0 radiated partons, and 3 radiated partons [2].

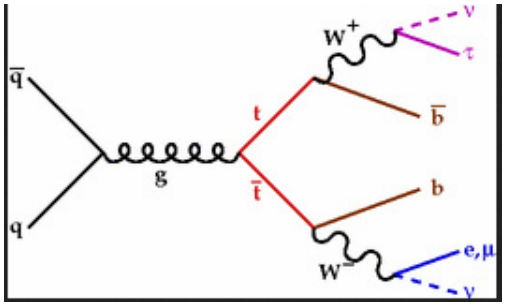

Figure 5.2: $t\bar{t}$ Feynman diagram [3].

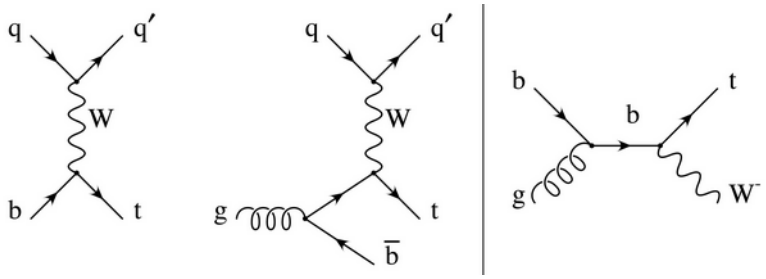

Figure 5.3: Single top quark Feynman diagrams [4].

5.1 Monte Carlo and Corrections

Background processes were simulated in three steps. The first step used one or two MC generators to simulate the interaction between colliding protons, the decay of unstable particles, and the hadronization of partons leaving the interaction. Particles produced by the interaction interacted with the sub-detectors, and the signals that were generated in the sub-detectors were simulated in the second step. In the third step, the reconstruction algorithms processed the simulated signals to reconstruct leptons and jets.

In the first step, one MC generator simulated the interaction between colliding protons, and the decay of unstable particles. This generator was chosen so that the strengths of the generator matched the characteristics of the interaction. The MADGRAPH generator [63] simulates an interaction at leading order in the electroweak coupling with up to 4 additional partons radiated from the interaction. The POWHEG generator [64] simulates an interaction at next-to-leading order in the electroweak and QCD couplings with up to one additional parton radiated from the interaction. Lastly, the PYTHIA8 generator [65, 66] simulates an interaction at leading order in the electroweak and QCD couplings with up to one additional parton radiated from the interaction. The MADGRAPH generator was used to simulate the processes with the highest products of the cross section and branching ratio - Drell-Yan +jets, $t\bar{t}$ pair production, and W+jets production. The production of single top quarks with a W boson has a cross section-branching ratio product to $\ell\ell jj$ final states that increases by 7% or more by going from leading order to next-to-leading order [67]. For this reason, POWHEG was used to simulate the single top quark processes to more accurately estimate the background produced by single top quark processes. Similar to the single top quark processes, the production of diboson pairs has a cross section-branching ratio product to $\ell\ell jj$ final states that increases, by up to 45%, going from leading order to next-to-

leading order [68]. However, the product of the cross section and branching ratio to $\ell\ell jj$ final states for the diboson processes at next-to-leading order is still negligible compared to Drell-Yan +jets and top quark processes, so PYTHIA8 was used to simulate the diboson processes.

The hadronization of partons was simulated separately with a single MC generator. Background processes that are simulated with any generator show the best agreement with experimental data when PYTHIA8 is used to simulate parton hadronization [69], so all simulations used PYTHIA8 and the NNPDF23 PDF set [70] to simulate parton hadronization. Excluding the partons, the generator that simulated the interaction between protons was also used to simulate the decay of unstable particles to quasi-stable and stable particles, like the $\Sigma^{\pm}$ and γ, that travel a mean distance $c\tau \gtrsim 2.4$ cm before decaying. Particles that travel a mean distance of 2.4 cm have a small probability to interact with the first silicon pixel tracker layer located 4.4 cm from the IP [37], so they were not decayed before the detector response was simulated.

The large instantaneous luminosity of the LHC beams produced multiple pp interactions (pileup) in each event in data. In the second step, the pileup interactions were simulated, and GEANT4 [71], which is a general purpose detector simulation program, was used to simulate the propagation and decay of quasi-stable and stable particles, and their interactions with the detector. The pileup was simulated by sampling a random integer X from a Poisson distribution with a mean of 12, and mixing X simulated minimum bias events into the event that were simulated through the first simulation step. The distributions of reconstructed particle multiplicity and kinematics found in minimum bias events in data show the best agreement with those found in events simulated with PYTHIA8 [69], so PYTHIA8 was used to simulate minimum bias events. After adding minimum bias events, GEANT4 propagated all particles through the 3.8 T magnetic field, and simulated their interactions with the detector and the resulting

signals. In addition, GEANT4 also simulated the decays of quasi-stable particles to the following stable particles - $\gamma, p^{\pm}, n^0, \bar{n}^0, \nu, e^{\pm}$.

In the third step, particle reconstruction algorithms reconstructed particles and vertices using the signals in the detector that were simulated by GEANT4. The trigger selection criteria were applied and the final decision of each trigger algorithm was saved in each event, but no events were discarded.

After the third step, corrections were applied to simulated event weights. As discussed in Chapter 4, the efficiencies of reconstruction algorithms and selection criteria differed between data and simulations. These efficiency differences were resolved by changing the weight of each simulated event by up to $\pm 7\%$, depending on the kinematics of the selected leptons. Independent of the kinematics of the reconstructed particles, the weight of each simulated event was normalized to the integrated luminosity of the data, and adjusted further to match the pileup distribution found in the data. The simulated pileup distribution is a Poisson distribution with a mean of 12, but the pileup distribution found in the data is better represented by a Poisson distribution with mean 14 [38]. The discrepancy between the data and simulated pileup distributions was corrected by changing the weight of each simulated event, on average by $\sim 5\%$.

Reconstructed leptons and jets were measured with different energies in data and simulated events, so energy corrections were applied to particles that were reconstructed in simulated events. Energy corrections for simulated muons, electrons, and jets were derived using $Z \to \ell\ell$, Z+jet, dijet and γ+jet events from simulations and data. The di-lepton and di-jet mass distributions found in these events were compared between data and simulations, and the energies of simulated leptons and jets were corrected so that the distributions matched. The average correction was 1% of a muon's p_T, 1% of an electron's E_T, and 6% of a jet's p_T.

The processes that were simulated and the corresponding number of simulated events

Table 5.1: A summary of the background processes and the sizes of the simulated datasets. The "Size" of a dataset is equal to the number of simulated events of a specific process divided by the product of the cross section and branching ratio.

Dataset	Step 1 Generator	cross section (pb)	Size (fb^{-1})
Inclusive DY+jets, $DY \to ll$	MADGRAPH	5991	1.51
DY+jets HT 100-200, $DY \to ll$	MADGRAPH	181.3	15.0
DY+jets HT 200-400, $DY \to ll$	MADGRAPH	50.42	19.3
DY+jets HT 400-600, $DY \to ll$	MADGRAPH	6.984	153.
DY+jets HT > 600, $DY \to ll$	MADGRAPH	2.704	369.
t$\bar{t}$+jets $\to ll$+jets	MADGRAPH	85.67	286.
single t $\to$ leptons+jets	POWHEG	80.95	20.8
single $\bar{t}$ $\to$ leptons+jets	POWHEG	136.0	24.3
$\bar{t}$+W $\to$ all	POWHEG	35.85	27.6
t+W $\to$ all	POWHEG	35.85	27.8
WW $\to$ all	PYTHIA8	113.8	8.73
ZZ $\to$ all	PYTHIA8	10.15	98.2
WZ $\to$ all	PYTHIA8	23.4	41.8
W+jets $\to l\nu$+jets	MADGRAPH	50270	1.44

is summarized in Table 5.1. The number of simulated events is expressed in units of fb^{-1}, and should be compared to the 2.6 fb^{-1} of data that was collected.

5.2 Top Quark Background

As discussed in Chapter 2.3, due to lepton flavor conservation the W_R cannot decay to final states with an electron and a muon. Therefore, $e\mu jj$ events found in the data were produced only by background processes. The production of a $t\bar{t}$ quark pair and a top quark with a W boson yields events with two partons and two W bosons. Since a W boson decays to an electron or a muon with equal branching ratios, the top quark processes produce the $e\mu jj$ final state twice as often as the $eejj$ or $\mu\mu jj$ final states. As no other ST processes produce the $e\mu jj$ final state at leading order in the electroweak coupling, the majority of $e\mu jj$ events found in data were produced by top quark processes. The $e\mu jj$ final state was used as a control region to estimate the top quark

background.

During collisions, $e\mu jj$ events were selected using a trigger that required one muon and one electron. Leptons and jets that were reconstructed offline were selected with additional criteria. Events that met the selection criteria, described in detail in Appendix B, had one electron, one muon, and at least two jets with the characteristics described previously in Chapter 4.3. However, the electron had an $E_T > 30$ GeV, and the muon had a $p_T > 30$ GeV.

In events selected by the trigger, leptons and jets were reconstructed, and events were selected using the event selection described in Chapter 4 applied to the electron and muon selected by the trigger.

These selection criteria were applied to simulated background events, and compared to the selected data events in Figure 5.4. Comparing the magnitudes of different simulated backgrounds, the top quark background produces more than 98% of selected $e\mu jj$ events, as expected.

The $M_{e\mu jj}$ distribution found in selected data events was scaled by one factor to estimate the top quark background in the ee- and $\mu\mu$-channels. The factor is the ratio of $\frac{\ell\ell}{e\mu}$ production, which is 0.5 based on lepton universality in the decay of the W boson, multiplied by the ratio of the electron and muon selection efficiencies $\frac{e}{\mu}$, which is below 1 due to the reduced acceptance of the ECAL relative to the muon detectors, and is not known *a-priori*. The factor and its variation with $M_{\ell\ell jj}$ was estimated using simulated top quark events. To make this estimation, simulated events were selected using the $e\mu$-, ee-, and $\mu\mu$-channel selection criteria. Then, the $M_{\ell\ell jj}$ distribution found in each set of events was split into variable width bins such that each bin had the same number of events. The first bin covered $600 < M_{\ell\ell jj} \leq 625$ GeV, and the last bin covered $M_{\ell\ell jj} > 1160$ GeV. Then, the integral of each bin was calculated for all three distributions. Finally, the integrals of the M_{eejj} and $M_{\mu\mu jj}$ bins were divided by the

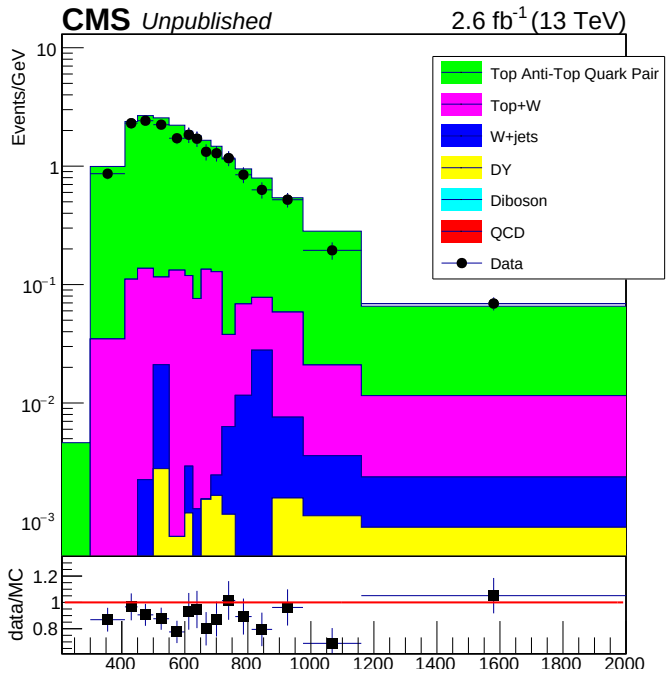

Figure 5.4: The $M_{\ell\ell jj}$ distribution from data and simulated ST events that passed the $e\mu$ selection criteria, excluding the $M_{\ell\ell jj} > 600$GeV cut. The bin widths were variable, and their contents were normalized to the bin widths.

integrals of the $M_{e\mu jj}$ bins. The result, shown in Figure 5.5, represents the factor used to estimate the top quark background as a function of $M_{\ell\ell jj}$. The factor within its statistical uncertainty is independent of $M_{\ell\ell jj}$, and is equal to 0.659 for $M_{\mu\mu jj}/M_{e\mu jj}$, and 0.432 for $M_{eejj}/M_{e\mu jj}$. It is assumed that the $M_{\ell\ell jj}$ distribution shape found in top quark events is independent of the final state lepton flavor. The top quark contributions to the M_{eejj} and $M_{\mu\mu jj}$ distributions found in data were estimated by scaling the $M_{e\mu jj}$ distribution found in data by 0.432 and 0.659, respectively.

Although the values 0.659 and 0.432 were calculated using all simulated events with $M_{\ell\ell jj} > 600$ GeV, the majority of selected simulated events had $M_{\ell\ell jj} < 1500$ GeV. A 10% uncertainty was assigned to the top quark background estimate to cover any

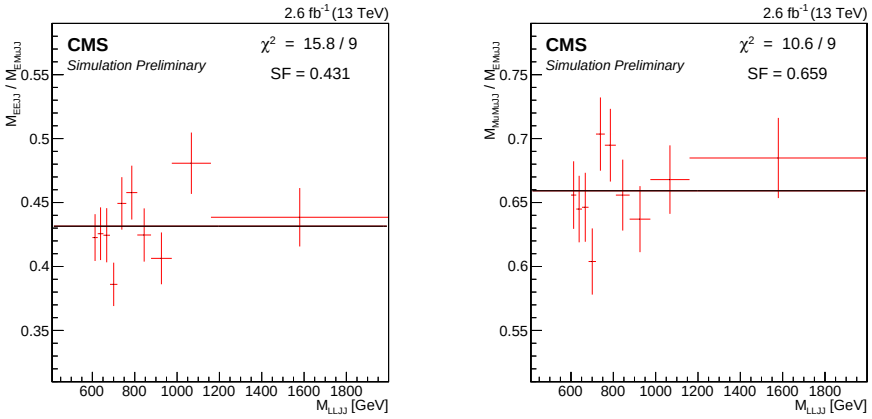

Figure 5.5: The bin-by-bin ratio of the $M_{\ell\ell jj}$ and $M_{e\mu jj}$ distributions from simulated top quark backgrounds, where ℓ is an electron on the left, and a muon on the right.

deviation from 0.659 or 0.432 at high $M_{\ell\ell jj}$. Based on the data and simulated events shown in Figure 5.4, the non-top quark backgrounds contributed ∼1% to the $M_{e\mu jj}$ distribution found in data. Their contribution was neglected because it was less than the 10% top quark background uncertainty.

5.3 Drell-Yan Background

The Drell-Yan +jets process produced $\ell\ell jj$ events at similar rates to the top quark processes. Since the W_R decay does not produce events with an electron and a muon, the top quark background was estimated directly from data in the $e\mu jj$ control region. No analogue of the $e\mu jj$ control region exists for the Drell-Yan +jets background, so it needed to be estimated using simulated events. The model of the Drell-Yan +jets process used in simulations is an approximation, and the differences between the Drell-Yan predictions and the data were estimated by comparing simulated background events to data events in three control regions.

5.3.1 Drell-Yan normalization in $M_{\ell\ell jj}$

The approximations made in the Drell-Yan +jets model result in a difference between the data and the simulations in the normalization of the $M_{\ell\ell jj}$ distribution. The size of this difference was estimated using the $Z \to \ell\ell$ control region.

The data and simulated Drell-Yan +jets events were compared in the $Z \to \ell\ell$ control region, where the majority of events found in the data were produced by the Drell-Yan +jets process. During collisions, events that had two electrons or one muon were selected using the triggers described in Appendix B.1. Offline, leptons and jets were reconstructed, and additional selection criteria were applied. Selected events had two leptons and jets with the following characteristics:

- Each lepton had a $p_T > 35$ GeV, and an $|\eta| < 2.4$.
- The two leptons had a di-lepton mass $70 < M_{\ell\ell} < 110$ GeV.
- Each jet had a $p_T > 40$ GeV, and an $|\eta| < 2.4$.
- Each jet was separated from both leptons by $\Delta R > 0.4$.

Electrons reconstructed in simulated events passed the trigger criteria with a different efficiency than electrons reconstructed in data events. This efficiency difference was corrected by multiplying the weight of every simulated event by a value that depended on the E_T and η of the highest E_T electron selected by the trigger. The average value of the correction was 0.96.

The $M_{\ell\ell}$ distribution in data for $Z \to \ell\ell$ events was compared with the distribution of the same events in Drell-Yan +jets simulations. The normalization of the $M_{\ell\ell}$ distribution in data and simulations was compared by integrating the distribution in data and simulated events, and comparing the integral values. The normalization of the $M_{\ell\ell}$ distribution measured in data exceeded the normalization measured in simulated events

by 15.7% in the ee-channel, and 14.2% in the $\mu\mu$-channel. As a result, the weight of simulated Drell-Yan +jets events was increased by 15.7% in the ee-channel, and 14.2% in the $\mu\mu$-channel to more accurately predict the Drell-Yan background.

The uncertainty on the $\sim$15% Drell-Yan normalization correction was estimated using simulated Drell-Yan +jets events produced using two other MC generators. One generator simulates the Drell-Yan process at next-to-leading order in the electroweak and QCD couplings and radiates up to four partons. The other generator, POWHEG, simulates the Drell-Yan process and radiates up to one parton. Events from data and Drell-Yan + jets simulations using all three generators were selected using the $Z \rightarrow \ell\ell$ selection criteria without jet requirements. The jet requirements were removed to compare data to simulations in a phase space where POWHEG yielded a large number of selected events, comparable to the simulations produced with the other generators. The normalization of the $M_{\ell\ell}$ distribution in data and simulations was compared by integrating the distribution measured in data and simulated events, and comparing the integral values. Since no jet requirements are applied the simulations are expected to match the data, and any deviation from this expectation was taken as an uncertainty. The largest difference in the normalization measured in data and any of the simulated events was 2.0% in the ee-channel, and 1.0% in the $\mu\mu$-channel. This difference was taken as an uncertainty on the number of Drell-Yan background events that were predicted in each channel.

Based on simulations of all ST processes, the contribution of ST processes excluding Drell-Yan +jets to the data events selected in the $Z \rightarrow \ell\ell$ control region was 2% of the total background that was predicted in the control region. This 2% is comparable to the Drell-Yan background normalization uncertainty, so the contribution of other backgrounds to the data in the control region was neglected.

5.3.2 Drell-Yan shape in $M_{\ell\ell jj}$

The approximations made in the Drell-Yan +jets model also cause the shape of the $M_{\ell\ell jj}$ distribution to differ between data and simulated Drell-Yan +jets events. The size of this shape difference was estimated using the low $M_{\ell\ell}$ control region.

The data and simulated events of all ST processes were compared in the low $M_{\ell\ell}$ control region, where the majority of events found in the data were produced by the Drell-Yan +jets process. Data and simulated events were selected using the event selection described previously in Chapter 4, but the two selected leptons were required to have a $M_{\ell\ell} < 180$ GeV. Based on the normalization correction described in Section 5.3.1, the weight of events selected in Drell-Yan +jets simulations was increased by 15.7% in the ee-channel, and 14.2% in the $\mu\mu$-channel. Then, the $M_{\ell\ell jj}$ distribution measured in data and simulated events were compared. The size of the $M_{\ell\ell jj}$ shape difference was calculated as the largest difference between the data and the total background in any bin shown in Figure 5.6. The maximum difference, 40% for $M_{\ell\ell jj} > 1.9$ TeV in both channels, was taken as the shape difference for events with $M_{\ell\ell jj} > 0.6$ TeV.

Initially the large shape difference was attributed to limitations of the Drell-Yan +jets simulation - the Drell-Yan process was simulated only at leading order in the electroweak and QCD couplings. This was tested by simulating a separate set of Drell-Yan +jets events using a different MC generator at next-to-leading order in the electroweak and QCD couplings, and with up to four partons radiated from the initial state quarks. The procedure described in Section 5.3.1 was repeated to re-calculate a Drell-Yan +jets normalization correction for the simulated Drell-Yan events. The $M_{\ell\ell jj}$ distribution measured in simulated events, compared to data in Figure 5.7, shows a larger difference with the data when using the next-to-leading order Drell-Yan +jets simulation than with the leading order simulation. The larger difference was therefore not caused by

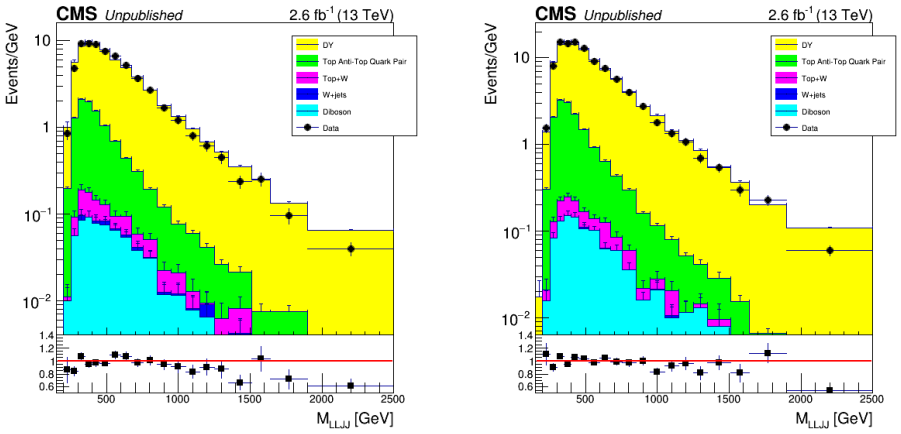

Figure 5.6: The $M_{\ell\ell jj}$ distributions from data and simulated background events that passed the low $M_{\ell\ell}$ control region selection criteria. The ee-channel is on the left, and the $\mu\mu$-channel on the right. The bin widths are variable, and the bin contents are normalized to their widths.

higher order QCD or electroweak interactions, but by a significant decrease in selected events. Comparing the leading order and next-to-leading order Drell-Yan +jets simulations after applying the low $M_{\ell\ell}$ selection criteria, the next-to-leading order simulation produced a factor of $\sim$3 fewer events with $M_{\ell\ell jj} > 0.6$ TeV, and a factor of $\sim$10 fewer events with $M_{\ell\ell jj} > 1$ TeV. Similar deficits in selected events were found in events that had $M_{\ell\ell jj} > 600$ GeV and $M_{\ell\ell} > 200$ GeV. For these reasons the next-to-leading order Drell-Yan +jets simulation was not used to estimate the Drell-Yan +jets background, and the large shape difference could not be attributed to next-to-leading order effects. Instead, it was investigated if the shape difference should be applied as a correction or assigned as an uncertainty.

The effect of the 40% $M_{\ell\ell jj}$ shape difference on the Drell-Yan background prediction can be accounted for in two ways. The simulated Drell-Yan +jets event weights can be adjusted to match the $M_{\ell\ell jj}$ distribution found in data, or an uncertainty can be assigned to the Drell-Yan background prediction. Correcting the simulated event weights to match the data was not done for two reasons. First, the variation of the $M_{\ell\ell jj}$-dependent

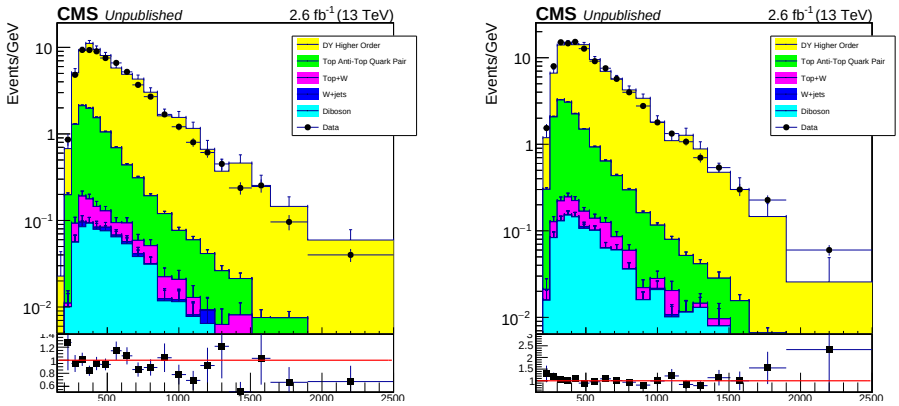

Figure 5.7: The $M_{\ell\ell jj}$ distribution found in data and simulated background events that passed the low $M_{\ell\ell}$ control region selection criteria. The ee-channel is on the left, and the $\mu\mu$-channel is on the right. The bin contents are normalized to their widths.

correction versus $M_{\ell\ell}$ could not be checked. This was a significant concern in particular for events that had $M_{\ell\ell jj} > 1900$ GeV, because the weight of those events would have been corrected by 40%. Secondly, the uncertainty on the correction was dominated by the statistical uncertainty of the data, which exceeded 30% for $M_{\ell\ell jj} > 1900$ GeV. Since the correction had a large statistical uncertainty and could not be validated in events with $M_{\ell\ell jj} > 600$ GeV and $M_{\ell\ell} > 200$ GeV, the effect of the 40% shape difference was accounted for by assigning an uncertainty to the Drell-Yan prediction.

The magnitude of the uncertainty was determined by counting the number of predicted Drell-Yan +jets events in bins of $M_{\ell\ell jj}$. Each bin is linked to a specific M_{W_R} hypothesis, and the shape of the Drell-Yan $M_{\ell\ell jj}$ distribution in each bin is irrelevant. Thus a shape difference and a normalization difference have the same effect - the total number of events in the bin change by the magnitude of the difference. Therefore, the effect of the shape difference was accounted for by assigning a 40% uncertainty to the normalization of the $M_{\ell\ell jj}$ distribution measured in simulated Drell-Yan +jets events, independent of $M_{\ell\ell jj}$.

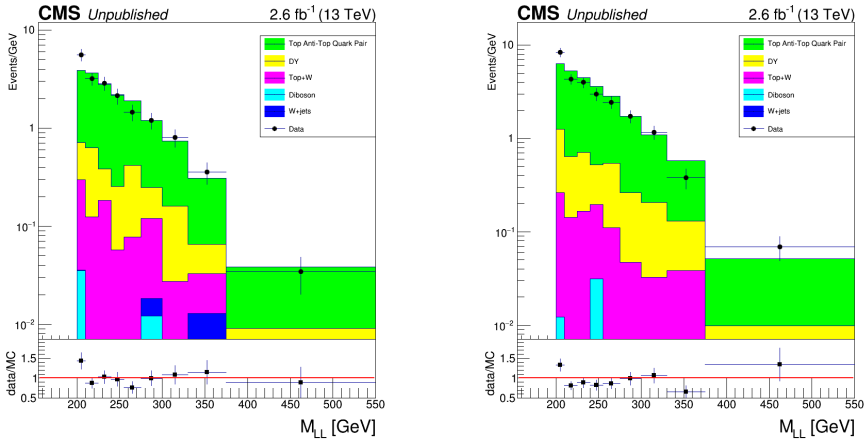

Figure 5.8: The $M_{\ell\ell}$ distribution found in data and simulated background events that passed the low $M_{\ell\ell jj}$ control region selection criteria. The ee-channel is on the left, and the $\mu\mu$-channel is on the right.

The low $M_{\ell\ell jj}$ control region was used to validate the ∼15% correction applied, and the 40% uncertainty assigned to the Drell-Yan prediction. Events from data and all background simulations were selected using the same selection criteria as the low $M_{\ell\ell}$ control region, but with $M_{\ell\ell} > 200$ GeV and $M_{\ell\ell jj} < 600$ GeV. The weight of simulated Drell-Yan events was increased by ∼15%, and then the $M_{\ell\ell}$ distributions found in selected data and simulated background events were compared. The comparison, shown in Figure 5.8, shows that the ∼15% Drell-Yan correction brought the background estimate into better agreement with the data. In addition, the 40% Drell-Yan uncertainty was not too conservative, because the disagreement between data and estimated backgrounds approached 40% in several bins.

5.3.3 Drell-Yan summary

The Drell-Yan contribution to the $M_{\ell\ell jj}$ distribution found in data was estimated by selecting simulated Drell-Yan events using the selection criteria described in Chapter 4. The weight of each selected event was increased by 15.7% the ee-channel, and by 14.2%

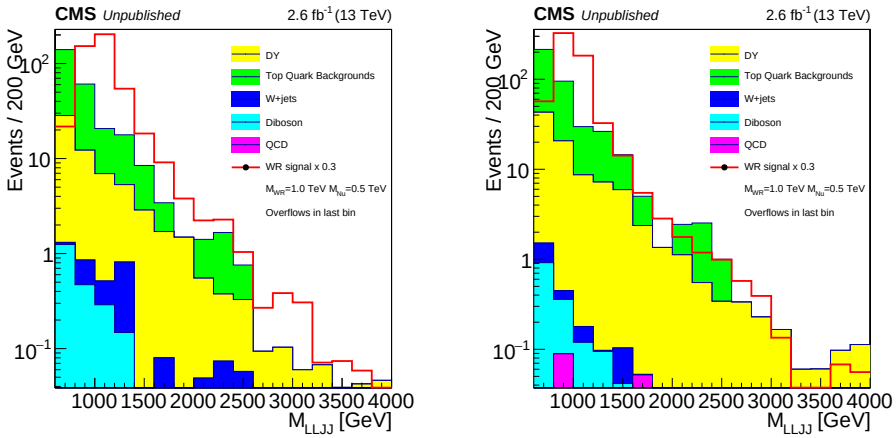

Figure 5.9: The M_{eejj} (left) and $M_{\mu\mu jj}$ (right) distributions found in selected signal and background events. The top quark and QCD backgrounds are estimated using data. The W_R $M_{\ell\ell jj}$ distribution normalization is reduced by 70%.

in the $\mu\mu$-channel. When calculating the results, a 40% uncertainty was assigned to the Drell-Yan prediction.

5.4 Diboson and W+jets Backgrounds

The diboson (WW, WZ, ZZ) and W+jets processes produced $\ell\ell jj$ events at a much lower rate than the Drell-Yan +jets process. No control region existed where the diboson or W+jets backgrounds could be extracted directly from data, so their contributions to the $M_{\ell\ell jj}$ distributions found in data were estimated using simulated events. The $M_{\ell\ell jj}$ distribution measured in selected diboson and W+jets events (Figure 5.9) was concentrated in the $M_{\ell\ell jj} \leq 2.0$ TeV region, and its integral was less than 3% of the total Drell-Yan and top quark prediction. For these reasons the diboson and W+jets contributions to the $M_{\ell\ell jj}$ distribution in the data were neglected.

5.5 QCD Background

Similarly, the QCD multi-jet processes produced $\ell\ell jj$ events at a much lower rate than the Drell-Yan +jets process. Unlike the other backgrounds, the leptons selected offline in QCD events were incorrectly reconstructed from jets that contained energetic electrons or photons. Events in data where two jets may have been identified as leptons were selected using the online and offline selection criteria described in Chapter 4, but using the following (reduced) lepton ID selection criteria:

Muons

- The silicon tracker track was reconstructed from signals in at least 1 silicon pixel detector layer, and signals in at least 5 layers in the entire tracker.

Electrons

- The electron track was reconstructed from signals in every silicon pixel and inner strip detector layers, or all but 1 layer.
- The electron track's origin was separated from its vertex by a small distance Δ_{xy} in the $x-y$ plane: $\Delta_{xy} < 0.2$ mm in the tracker barrel, and $\Delta_{xy} < 0.5$ mm in the tracker endcap.

Events were rejected if one or both selected leptons passed the standard lepton ID selection criteria. In the selected events, the p_T's and η's of both selected leptons were used as inputs to a p_T, η-dependent probability function. This function, derived elsewhere [72], calculates the probability that a jet reconstructed as a lepton will pass the standard lepton ID selection criteria[1]. The probability calculated for both selected leptons was applied to each selected event as a weight. The $M_{\ell\ell jj}$ distribution found in selected weighted events (Figure 5.9) was negligible compared to other backgrounds, so the QCD background was neglected.

[1]The form of the function differed for electrons and muons.

5.6 Background Estimation Summary

ST processes produced events in data where two leptons and jets were reconstructed, and passed the selection criteria that was designed to select $W_R \to \ell\ell jj$ events. The $M_{\ell\ell jj}$ distribution produced by each interaction, and the uncertainty on its normalization was estimated using data and simulated events in control regions. The Drell-Yan +jets and top quark processes were estimated to give more than 97% of the background, so the sum of the Drell-Yan and top quark backgrounds was identified as the total predicted background. This was compared to data in bins of $M_{\ell\ell jj}$ that were linked to specific M_{W_R} hypotheses. These bins and the comparison between the data and predicted background is discussed in the next chapter.

Chapter 6

Results and their Uncertainties

After estimating the background, the $M_{\ell\ell jj}$ distributions found in the selected data and predicted background events were compared. The difference between the number of data and background events was compared to the estimate of the background uncertainty. Since different M_{W_R} hypotheses resulted in $M_{\ell\ell jj}$ distributions (Figure 6.1), comparisons were made in distinct windows (bins) that were linked to specific M_{W_R} hypotheses. The sizes of these windows, the estimate of the background uncertainty, and the results of the comparisons are described in this chapter.

6.1 Statistical Analysis

The number of different $M_{\ell\ell jj}$ windows was chosen based on how the $M_{\ell\ell jj}$ distribution found in simulated W_R events changed with the W_R and N_l masses. For a fixed W_R mass, the shape of the $M_{\ell\ell jj}$ distribution found in signal events is weakly dependent on the N_l mass, as shown in Figure 6.2, because the product of the W_R cross section and branching ratio varies weakly with M_{N_l}. Since the shape varies weakly with the N_l mass, one $M_{\ell\ell jj}$ window is assigned to each W_R mass for all N_l mass values. The $M_{\ell\ell jj}$

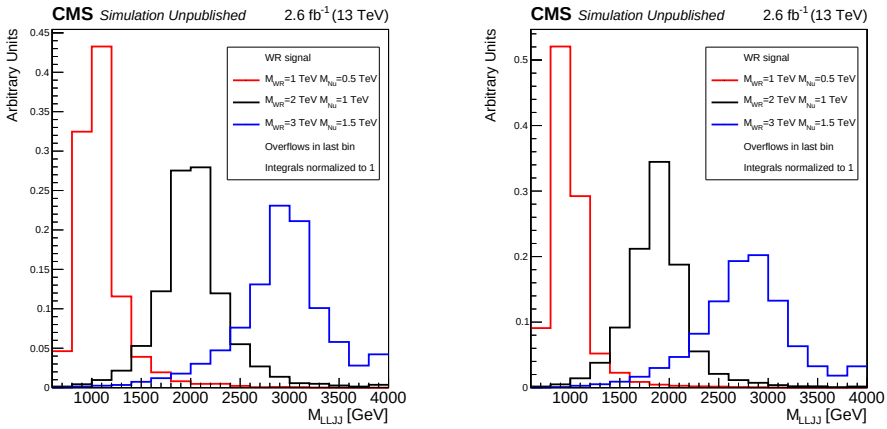

Figure 6.1: The $M_{\ell\ell jj}$ distributions found in selected W_R events with different values of the W_R and N_l masses. The ee-channel is on the left, and the $\mu\mu$-channel is on the right.

window size for a specific W_R mass is determined using events that have $M_{N_l} = \frac{1}{2}M_{W_R}$, because at this M_{N_l} the event selection efficiency is maximized or nearly maximized. As the W_R mass increases the peak in the $M_{\ell\ell jj}$ distribution moves higher in $M_{\ell\ell jj}$, and the distribution becomes wider because the probability to produce a virtual W_R increases. In addition, the $M_{\ell\ell jj}$ distribution normalization decreases because the product of the W_R cross section and branching ratio decreases as the W_R mass increases. Therefore, several windows are needed to cover the entire $M_{\ell\ell jj}$ range that is spanned by the data, but the the number of windows should not be so large that multiple windows for different W_R mass hypotheses overlap significantly. For W_R mass hypotheses above 2.0 TeV, the $M_{\ell\ell jj}$ distributions linked to two signal hypotheses whose W_R masses differ by 0.2 TeV overlap by 10% or more, as shown in Figure 6.3. Due to this overlap, the two $M_{\ell\ell jj}$ windows designed for these two W_R mass hypotheses are also sensitive to any signal hypotheses that have W_R masses between these two masses, and an additional window is not needed. To cover the entire $M_{\ell\ell jj}$ spectrum found in the data, one $M_{\ell\ell jj}$ window is assigned to each value of M_{W_R} stepping from 0.8 to 6 TeV in increments of 0.2 TeV.

The size of each $M_{\ell\ell jj}$ window was determined based on the shape and normalization of the $M_{\ell\ell jj}$ distribution found in background events, and was chosen to maximize the sensitivity of the search.

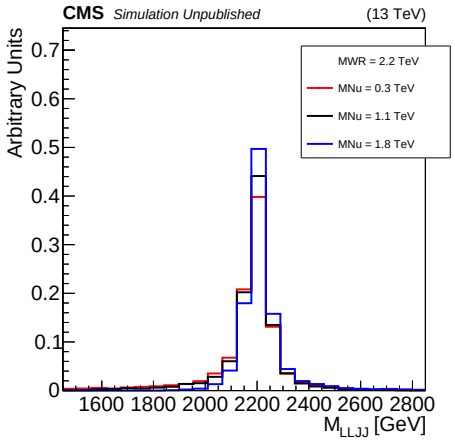

Figure 6.2: The $M_{\ell\ell jj}$ distribution found in $W_R \to \ell\ell jj$ events that have $M_{W_R} = 2.2$ TeV and different values of the N_l mass.

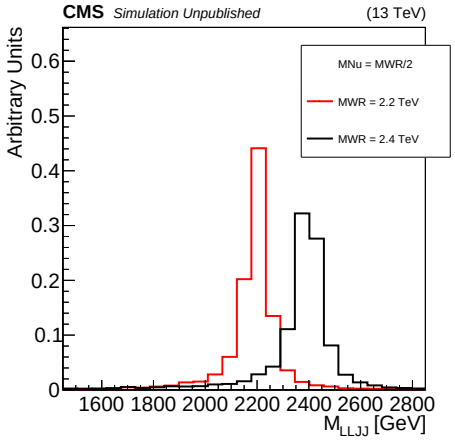

Figure 6.3: The $M_{\ell\ell jj}$ distribution found in $W_R \to \ell\ell jj$ events that have $M_{N_l} = \frac{1}{2}M_{W_R}$ and different values of the W_R mass.

6.1.1 $M_{\ell\ell jj}$ Window Sizes

The sizes of the $M_{\ell\ell jj}$ windows were chosen to maximize the sensitivity to $\sigma(W_R) \times BR(W_R \to \ell\ell jj)$. For each value of M_{W_R} between 0.8 and 6 TeV in increments of 0.2 TeV, the size of the window was determined using the following procedure:

- 150 $M_{\ell\ell jj}$ windows of different sizes and central values were defined based on the peak position in the W_R $M_{\ell\ell jj}$ distribution. The window lower bound went down to 40% of M_{W_R}, and the upper bound went up to 140% of M_{W_R}.
- For each window:
  - The number of signal events S and background events B were counted.
  - A Poisson distribution was created with mean B, and a random number C was sampled from the Poisson distribution. C represents the number of measured events in the window.
  - Using C, S, B, and the procedure described in Appendix C, an expected upper limit on $\sigma(W_R) \times BR(W_R \to \ell\ell jj)$ was calculated at 95% CL. The systematic uncertainties on S and B had a negligible effect on the final window size, so only the statistical uncertainties on S and B were included.
  - The limit was recalculated 300 times, and each time a new random number C was sampled from the Poisson distribution. The median value of all 300 limits was used as the expected upper limit for the window.
- The window that minimized the expected upper limit was chosen.

The $M_{\ell\ell jj}$ windows, listed in Table 6.1, capture at least 70% of the corresponding W_R $M_{\ell\ell jj}$ distribution. The central value of each window ($\frac{maxmin}{2}$) exceeds the corresponding W_R mass to reduce the background predicted in the window, which falls rapidly with increasing $M_{\ell\ell jj}$.

Table 6.1: $M_{\ell\ell jj}$ window ranges that maximized the sensitivity to detection at different W_R masses.

M_{W_R} (GeV)	$M_{\ell\ell jj}$ window (GeV)	
	Electrons	Muons
800	700 - 1100	700 - 1200
1000	900 - 1300	900 - 1400
1200	1100 - 1550	1100 - 1650
1400	1250 - 1750	1300 - 1850
1600	1450 - 2000	1500 - 2100
1800	1600 - 2250	1600 - 2300
2000	1850 - 2550	1850 - 2600
2200	2000 - 2800	2000 - 2850
2400	2150 - 3100	2150 - 3100
2600	2250 - 3400	2300 - 3400
2800	2350 - 3700	2400 - 3700
3000	2500 - 4000	2500 - 3950
3200	2550 - 4300	2700 - 4250
3600	2700 - 4900	2900 - 4850
3800	2750 - 5200	2950 - 5150
4000	2800 - 5500	3000 - 5450
4200	2800 - 5750	3100 - 5750
4400	2850 - 6050	3150 - 6100
4600	2850 - 6300	3150 - 6400
4800	2850 - 6600	3200 - 6700
5000	2900 - 6850	3200 - 7000
5200	2900 - 7050	3200 - 7300
5600	2900 - 7500	3200 - 7850
5800	2950 - 7700	3200 - 8150
6000	2950 - 7900	3200 - 8400

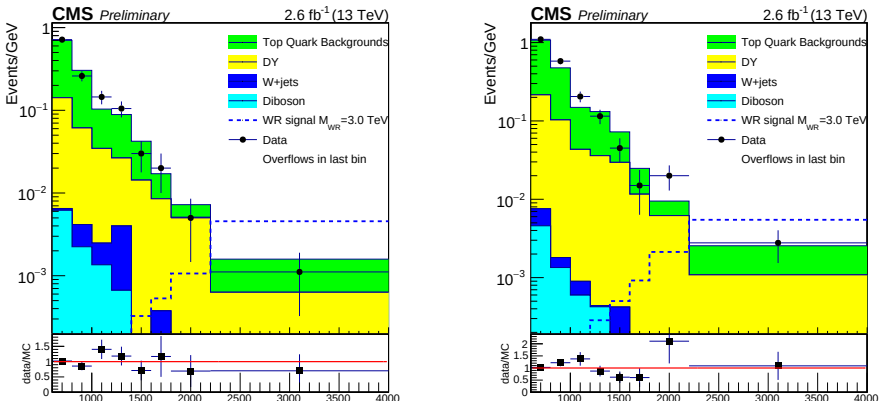

Figure 6.4: The $M_{\ell\ell jj}$ distributions found in data, and predicted in W_R and background events. The ee-channel is on the left, and the $\mu\mu$-channel is on the right.

6.2 Results

The M_{eejj} and $M_{\mu\mu jj}$ distributions found in data events were compared to those in predicted background events without the $M_{\ell\ell jj}$ window selection criteria applied in Figure 6.4, and with the selection criteria applied, listed in Table 6.2. No statistically significant excess of data events relative to the background was found in any of the $M_{\ell\ell jj}$ windows, so limits on $\sigma(W_R) \times BR(W_R \to \ell\ell jj)$ were calculated.

Table 6.2: The predicted number of signal ($M_{N_l} = \frac{1}{2}M_{W_R}$) and background events, their uncertainties, and the number of data events. BG = Total Background

	Electron channel				
M_{W_R} (GeV)	Signal (exp ± stat ± syst)	DY (exp ± stat ± syst)	Top quark (exp ± stat ± syst)	$\sum$ BG (exp ± stat ± syst)	Data
800	2690.0 ± 36.4 ± 103.4	37.95 ± 2.54 ± 15.69	107.52 ± 6.81 ± 11.62	145.48 ± 7.27 ± 19.52	136.0
1000	1196.0 ± 15.0 ± 46.0	21.11 ± 1.64 ± 8.79	40.87 ± 4.2 ± 4.76	61.99 ± 4.51 ± 10.0	64.0
1200	583.0 ± 7.2 ± 23.0	14.31 ± 1.3 ± 5.9	24.25 ± 3.23 ± 2.58	38.56 ± 3.49 ± 6.43	43.0
1400	327.0 ± 3.8 ± 12.3	10.67 ± 0.99 ± 4.44	16.15 ± 2.64 ± 1.79	26.82 ± 2.82 ± 4.79	23.0
1600	179.0 ± 2.0 ± 6.9	7.48 ± 0.7 ± 3.12	5.96 ± 1.6 ± 0.75	13.44 ± 1.75 ± 3.21	10.0
1800	108.0 ± 1.2 ± 4.1	5.8 ± 0.6 ± 2.52	3.05 ± 1.15 ± 0.42	8.85 ± 1.29 ± 2.56	6.0
2000	59.0 ± 0.6 ± 2.4	3.56 ± 0.2 ± 1.49	2.21 ± 0.98 ± 0.32	5.77 ± 1.0 ± 1.52	1.0
2200	38.0 ± 0.4 ± 1.5	2.66 ± 0.15 ± 1.16	2.25 ± 0.99 ± 0.3	4.92 ± 1.0 ± 1.2	2.0
2400	24.6 ± 0.26 ± 0.97	1.9 ± 0.13 ± 0.87	2.1 ± 0.95 ± 0.26	4.0 ± 0.96 ± 0.91	3.0
2600	16.3 ± 0.17 ± 0.61	1.58 ± 0.14 ± 0.7	1.43 ± 0.78 ± 0.29	3.01 ± 0.79 ± 0.76	2.0
2800	11.2 ± 0.11 ± 0.42	1.35 ± 0.13 ± 0.59	0.47 ± 0.45 ± 0.13	1.82 ± 0.46 ± 0.6	2.0
3000	7.3 ± 0.07 ± 0.27	1.02 ± 0.09 ± 0.44	0.43 ± 0.43 ± 0.05	1.45 ± 0.44 ± 0.45	2.0
3200	4.8 ± 0.05 ± 0.18	0.96 ± 0.09 ± 0.42	0.34 ± 0.34 ± 0.18	1.3 ± 0.35 ± 0.46	2.0
3600	2.1 ± 0.02 ± 0.08	0.76 ± 0.09 ± 0.35	0.0 ± 0.43 ± 0.0	0.76 ± 0.44 ± 0.35	1.0
3800	1.5 ± 0.01 ± 0.05	0.71 ± 0.09 ± 0.32	0.0 ± 0.43 ± 0.0	0.71 ± 0.44 ± 0.32	1.0
4000	1.0 ± 0.01 ± 0.04	0.65 ± 0.08 ± 0.29	0.0 ± 0.43 ± 0.0	0.65 ± 0.44 ± 0.29	1.0
4200	0.7 ± 0.01 ± 0.02	0.66 ± 0.08 ± 0.3	0.0 ± 0.43 ± 0.0	0.66 ± 0.44 ± 0.3	1.0
4400	0.44 ± 0.0042 ± 0.0163	0.61 ± 0.08 ± 0.27	0.0 ± 0.43 ± 0.0	0.61 ± 0.44 ± 0.27	1.0
4600	0.29 ± 0.0028 ± 0.0109	0.61 ± 0.08 ± 0.28	0.0 ± 0.43 ± 0.0	0.61 ± 0.44 ± 0.28	1.0
4800	0.2 ± 0.0019 ± 0.0074	0.61 ± 0.08 ± 0.28	0.0 ± 0.43 ± 0.0	0.61 ± 0.44 ± 0.28	1.0
5000	0.14 ± 0.0013 ± 0.005	0.56 ± 0.08 ± 0.26	0.0 ± 0.43 ± 0.0	0.56 ± 0.44 ± 0.26	1.0
5200	0.09 ± 0.0008 ± 0.0033	0.56 ± 0.08 ± 0.26	0.0 ± 0.43 ± 0.0	0.56 ± 0.44 ± 0.26	1.0
5600	0.04 ± 0.0004 ± 0.0015	0.56 ± 0.08 ± 0.26	0.0 ± 0.43 ± 0.0	0.56 ± 0.44 ± 0.26	1.0
5800	0.03 ± 0.0002 ± 0.001	0.51 ± 0.08 ± 0.23	0.0 ± 0.43 ± 0.0	0.51 ± 0.44 ± 0.23	1.0
6000	0.02 ± 0.0002 ± 0.0007	0.51 ± 0.08 ± 0.23	0.0 ± 0.43 ± 0.0	0.51 ± 0.44 ± 0.23	1.0
	Muon channel				
M_{W_R} (GeV)	Signal (exp ± stat ± syst)	DY (exp ± stat ± syst)	Top quark (exp ± stat ± syst)	$\sum$ BG (exp ± stat ± syst)	Data
800	3966.0 ± 44.4 ± 176.2	73.29 ± 6.11 ± 30.45	174.32 ± 10.72 ± 18.79	247.61 ± 12.34 ± 35.78	244.0
1000	1805.0 ± 17.9 ± 83.1	42.16 ± 2.28 ± 17.85	70.51 ± 6.82 ± 7.97	112.67 ± 7.19 ± 19.55	121.0
1200	872.0 ± 8.1 ± 43.4	24.23 ± 1.74 ± 10.07	38.5 ± 5.04 ± 4.07	62.73 ± 5.33 ± 10.86	57.0
1400	441.0 ± 4.0 ± 22.9	17.04 ± 1.42 ± 7.02	18.94 ± 3.53 ± 2.06	35.98 ± 3.81 ± 7.32	24.0
1600	244.0 ± 2.2 ± 13.3	12.71 ± 1.01 ± 5.31	6.56 ± 2.07 ± 1.08	19.27 ± 2.31 ± 5.42	17.0
1800	150.0 ± 1.3 ± 6.7	10.94 ± 0.41 ± 4.66	5.24 ± 1.86 ± 0.68	16.18 ± 1.9 ± 4.71	12.0
2000	82.0 ± 0.7 ± 4.3	6.52 ± 0.29 ± 2.81	3.44 ± 1.51 ± 0.45	9.96 ± 1.53 ± 2.85	8.0
2200	52.0 ± 0.5 ± 2.5	4.97 ± 0.25 ± 2.14	3.44 ± 1.51 ± 0.45	8.41 ± 1.53 ± 2.18	5.0
2400	32.5 ± 0.28 ± 1.52	3.89 ± 0.21 ± 1.69	3.2 ± 1.45 ± 0.4	7.1 ± 1.47 ± 1.74	4.0
2600	20.9 ± 0.18 ± 0.97	3.28 ± 0.17 ± 1.4	1.31 ± 0.92 ± 0.27	4.59 ± 0.94 ± 1.42	4.0
2800	13.8 ± 0.12 ± 0.6	2.97 ± 0.17 ± 1.28	0.66 ± 0.66 ± 0.18	3.63 ± 0.68 ± 1.29	4.0
3000	9.1 ± 0.08 ± 0.39	2.62 ± 0.16 ± 1.13	0.66 ± 0.66 ± 0.08	3.28 ± 0.68 ± 1.13	4.0
3200	5.9 ± 0.05 ± 0.26	1.99 ± 0.13 ± 0.9	0.0 ± 0.66 ± 0.0	1.99 ± 0.67 ± 0.9	1.0
3600	2.6 ± 0.02 ± 0.11	1.52 ± 0.12 ± 0.69	0.0 ± 0.66 ± 0.0	1.52 ± 0.67 ± 0.69	1.0
3800	1.8 ± 0.02 ± 0.07	1.46 ± 0.12 ± 0.66	0.0 ± 0.66 ± 0.0	1.46 ± 0.67 ± 0.66	1.0
4000	1.2 ± 0.01 ± 0.05	1.37 ± 0.1 ± 0.63	0.0 ± 0.66 ± 0.0	1.37 ± 0.67 ± 0.63	1.0
4200	0.8 ± 0.01 ± 0.03	1.21 ± 0.1 ± 0.55	0.0 ± 0.66 ± 0.0	1.21 ± 0.67 ± 0.55	1.0
4400	0.54 ± 0.0045 ± 0.0223	1.13 ± 0.09 ± 0.52	0.0 ± 0.66 ± 0.0	1.13 ± 0.67 ± 0.52	1.0
4600	0.37 ± 0.003 ± 0.0151	1.14 ± 0.09 ± 0.53	0.0 ± 0.66 ± 0.0	1.14 ± 0.67 ± 0.53	1.0
4800	0.24 ± 0.002 ± 0.0101	1.06 ± 0.08 ± 0.5	0.0 ± 0.66 ± 0.0	1.06 ± 0.66 ± 0.5	1.0
5000	0.18 ± 0.0014 ± 0.0074	1.06 ± 0.08 ± 0.5	0.0 ± 0.66 ± 0.0	1.06 ± 0.66 ± 0.5	1.0
5200	0.12 ± 0.0009 ± 0.0048	1.06 ± 0.08 ± 0.5	0.0 ± 0.66 ± 0.0	1.06 ± 0.66 ± 0.5	1.0
5600	0.05 ± 0.0004 ± 0.0022	1.06 ± 0.08 ± 0.5	0.0 ± 0.66 ± 0.0	1.06 ± 0.66 ± 0.5	1.0
5800	0.04 ± 0.0003 ± 0.0015	1.06 ± 0.08 ± 0.5	0.0 ± 0.66 ± 0.0	1.06 ± 0.66 ± 0.5	1.0
6000	0.02 ± 0.0002 ± 0.001	1.06 ± 0.08 ± 0.5	0.0 ± 0.66 ± 0.0	1.06 ± 0.66 ± 0.5	1.0

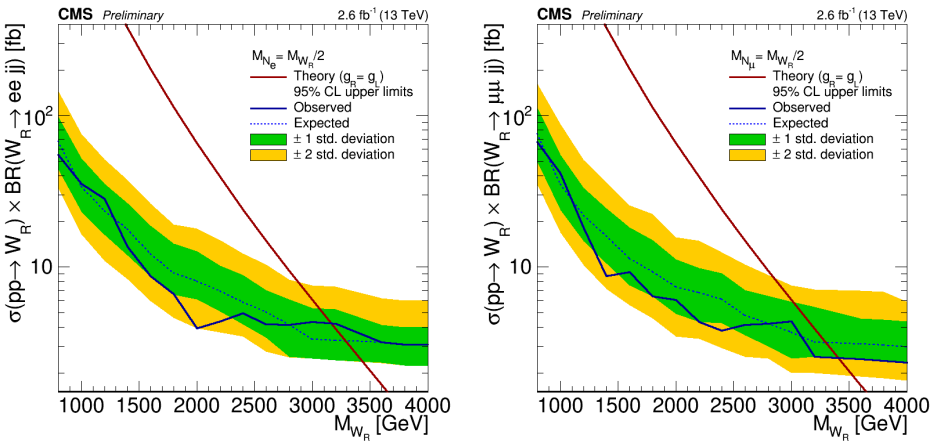

Figure 6.5: The expected and observed limits on $\sigma(W_R) \times BR(W_R \to \ell\ell jj)$ at 95% CL versus the M_{W_R} hypothesis. The ee-channel is on the left, and the $\mu\mu$-channel is on the right.

Using the observed number of data events and the signal and background predictions, upper limits on $\sigma(W_R) \times BR(W_R \to \ell\ell jj)$ were calculated at 95% CL in each $M_{\ell\ell jj}$ window. Observed upper limits were calculated using the data and signal and background predictions, and expected upper limits were calculated using only the signal and background predictions. The observed limit never exceeds the expected limit by more than one standard deviation, as shown in Figure 6.5. The uncertainties that contribute to the expected limit uncertainty are discussed in Section 6.3. For $M_{N_l} = \frac{1}{2} M_{W_R}$, the data excludes W_R production at 95% CL for $M_{W_R} < 3.2$ TeV in the ee-channel, and $M_{W_R} < 3.4$ TeV in the $\mu\mu$-channel.

The observed and expected limits were extrapolated into M_{N_l} and M_{W_R} exclusion limits. For any M_{N_l} the cross section limit L is linearly proportional to the signal efficiency χ of the event selection criteria multiplied by the W_R cross section $L \sim \chi \times \sigma(W_R)$. Since the background prediction at a given M_{W_R} value is the same for all M_{N_l}, the cross section limit at two (M_{W_R}, M_{N_l}) points with the same M_{W_R} but different M_{N_l} are related by the ratio of $\chi \times \sigma(W_R)$ at the points. Using this relationship, the

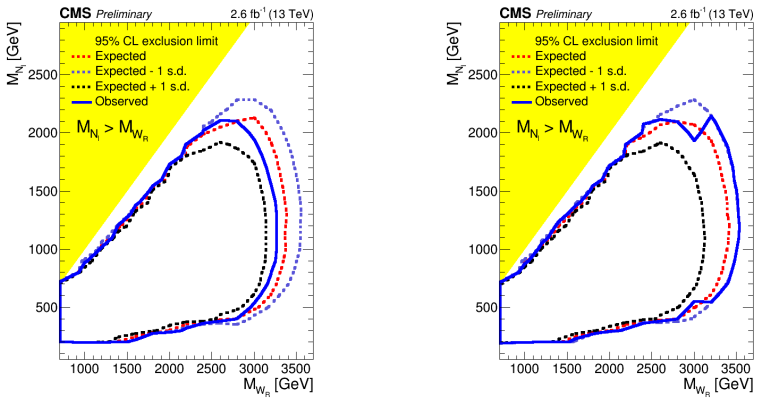

Figure 6.6: The exclusion limits on M_{W_R} and M_{N_l} at 95% CL. The ee-channel is on the left, and the $\mu\mu$-channel is on the right.

known cross section limit at $(M^a_{W_R}, M^a_{N_l} = \frac{1}{2}M^a_{W_R})$ was transformed into a limit at $(M^a_{W_R}, M^b_{N_l} \neq M^a_{N_l})$ using Equation 6.1.

$$Limit[(M^a_{W_R}, M^b_{N_l} \neq M^a_{N_l})] = \frac{\chi[(M^a_{W_R}, M^b_{N_l})]}{\chi[(M^a_{W_R}, M^a_{N_l} = \frac{1}{2}M^a_{W_R})]} \quad Limit[(M^a_{W_R}, M^a_{N_l} = \frac{1}{2}M^a_{W_R})] \tag{6.1}$$

The signal selection efficiency χ was calculated at different (M_{W_R}, M_{N_l}) points using simulated signal events. At a given M_{W_R}, the variation of χ versus M_{N_l} due to the online criteria and offline identification criteria was expected to be small, no more than a few percent. Therefore, χ was approximated by the selection efficiency $\chi^{'}$ of the offline kinematic selection criteria. $\chi^{'}$, whose variation with M_{W_R} and M_{N_l} is described in Chapter 4.4, was used in Equation 6.1 to extrapolate the cross section limits calculated for $M_{N_l} = \frac{1}{2}M_{W_R}$ to new limits L' for $M_{N_l} \neq \frac{1}{2}M_{W_R}$. Then, at each (M_{W_R}, M_{N_l}) point the new limit L' was divided by the cross section $\times$ branching ratio. The points where L' and the cross section $\times$ branching ratio are equal (Figure 6.6) are the extreme values of M_{N_l} and M_{W_R} that are excluded at 95% CL.

The difference between the selection efficiency $\chi^{'}$, without trigger and offline ID

criteria, and χ was expected to be small. This was checked by simulating $W_R \to \ell\ell jj$ events with $M_{W_R} = 2400$ and 4000 GeV and several $M_{N_l} \neq \frac{1}{2}M_{W_R}$ through the full simulation sequence, including pileup, trigger simulations, and particle reconstruction. Then the event selection criteria were applied, and selected events were used to calculate the limits L_{true} on $\sigma(W_R) \times BR(W_R \to \ell\ell jj)$. If the limits L_{true} and L' agree within their uncertainties, then the difference between $\chi^{'}$ and χ can be neglected. For events that have $M_{N_l} \gtrsim \frac{1}{8}M_{W_R}$, L_{true} and L' are consistent within their uncertainties. For events that have $M_{N_l} \lesssim \frac{1}{8}M_{W_R}$, the limit L_{true} is stronger than L' because of jets produced by pileup interactions. Each simulated event used to calculate L_{true} had an average of 12 pileup interactions, some of which produced jets that were reconstructed and passed the event selection criteria. As a result, the efficiency χ increased relative to $\chi^{'}$, and the lowest M_{N_l} excluded at 95% CL was about 75 GeV lower for L_{true} relative to L'. The 75 GeV difference was small compared to the entire range of M_{N_l} excluded at 95% CL, so no correction was applied to $\chi^{'}$, and the limit L' is the result.

6.3 Uncertainties

In each window, the observed and the expected limits were calculated with all systematic and statistical uncertainties included. The dominant uncertainties were the 40% Drell-Yan +jets uncertainty, the lepton and jet energy uncertainties, and the top quark background statistical uncertainty. The magnitudes of these uncertainties and all others were calculated in each $M_{\ell\ell jj}$ window using the procedures described here. The uncertainty magnitudes are the same for all $M_{\ell\ell jj}$ windows unless noted otherwise.

6.3.1 Energy and lepton identification Uncertainties

The lepton and jet energy uncertainties are unique in that they are the only uncertainties that can change the shapes of the $M_{\ell\ell jj}$ distributions found in signal and background

events. These uncertainties, specifically on the lepton and jet energy scales and resolutions, affect the energies of all reconstructed leptons and jets in every event. Variations of lepton and jet energies within their uncertainties can cause each event to pass or fail the selection criteria, or change a selected event's $M_{\ell\ell jj}$ value. The jet energy uncertainties went up to 25% for jets that had low p_T and large $|\eta|$, and the lepton energy uncertainties went up to ∼7% for electrons and muons. The efficiency of the lepton ID selection criteria is sensitive to lepton and jet energies, so the energy uncertainties are correlated with the lepton ID selection efficiency uncertainty. The effect of energy and lepton ID uncertainties were estimated simultaneously using the following procedure:

- In each event selected by a trigger, but before applying any lepton or jet selection criteria:
  - Eight random numbers were sampled from eight different Gaussians, each with mean 0 and variance 1.
  - Two random numbers multiplied each electron's energy scale and resolution uncertainty to determine the energy change applied to each electron. In simulated events, a third random number multiplied each electron's ID weight uncertainty, and the change in weight of the two selected electrons was propagated to the total event weight.
    - Using the same procedure with three other random numbers, the effect of muon energy and ID uncertainties were propagated to each muon's energy and ID weight.
  - The last two random numbers multiplied every jet's energy scale and resolution uncertainty, and these energy changes were added to the jet's energy.
- The offline selection criteria were applied to each event. Selected events were assigned to $M_{\ell\ell jj}$ bins based on their $M_{\ell\ell jj}$ values.

This procedure was repeated 3200 times for every event used to predict the signal and background $M_{\ell\ell jj}$ distributions. Then, a distribution was made showing the number of selected events in each window for all 3200 iterations (Figure 6.7). The distribution's standard deviation is the uncertainty on the number of predicted events, and this uncertainty varied with the $M_{\ell\ell jj}$ window. Increasing the M_{W_R} hypothesis from 1.8 to 4.0 TeV, the uncertainty on the signal prediction in each window was constant - 1% in the ee-channel, and 3% in the $\mu\mu$-channel. In both channels over the same M_{W_R} range the uncertainty on the Drell-Yan prediction increased from 10% to 20%, and the uncertainty on the top quark prediction increased from 14% to 53%. These uncertainties were included in limit calculations using Gamma distributions for the marginal posterior distributions.

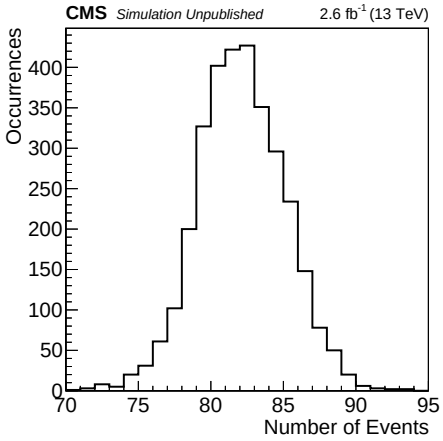

Figure 6.7: The distribution of the number of expected $W_R \to \mu\mu jj$ signal events with $M_{W_R} = 2.2$ TeV in the 2.2 TeV $M_{\ell\ell jj}$ window after 3200 iterations of energy and ID uncertainty variations.

6.3.2 Statistical Uncertainty

The signal and background statistical uncertainties were calculated as $\sqrt{\sum w_i^2}$, where w_i is the weight of event i, and the sum ran over all events in a $M_{\ell\ell jj}$ window. The $e\mu$ data

events, used to estimate the top quark background, all have a weight of 1. The simulated W_R and Drell-Yan +jets event weights were normalized to the integrated luminosity of the data, and as a result have positive weights less than 1. The statistical uncertainty due to the number of selected events was higher for the background prediction than the signal prediction, and the background uncertainty varied with the $M_{\ell\ell jj}$ window. Increasing the M_{W_R} hypothesis from 1.8 to 4.0 TeV, the uncertainty on the signal prediction in each window was 1% in both channels. In both channels over the same M_{W_R} range, the uncertainty on the Drell-Yan prediction increased from 10% to 13%, and the uncertainty on the top quark prediction increased from 38% to 100%. The statistical uncertainty was the largest uncertainty on the top quark background prediction. These uncertainties were included in limit calculations using Gamma distributions for the marginal posterior distributions.

No $e\mu$ data events were found in data with $M_{e\mu jj} \geq 2700$ GeV, so in the $M_{\ell\ell jj}$ windows used for $M_{W_R} \geq 3.6$ TeV the predicted top quark background was 0 events. In these windows the statistical uncertainty on the top quark prediction was set to 1 $e\mu$ event multiplied by the appropriate $\ell\ell : e\mu$ normalization factor - 0.659 or 0.432.

6.3.3 Background Uncertainty from control regions

Based on fluctuations in the number of simulated top quark and Drell-Yan +jets events in control regions, additional uncertainties were assigned to both background predictions. A 10% uncertainty was assigned to the top quark background prediction, and a 40% uncertainty was assigned to the Drell-Yan background prediction. This was the dominant uncertainty on the Drell-Yan background prediction. Both uncertainties were included in limit calculations using log-normal distributions for the marginal posterior distributions.

6.3.4 Lepton efficiency Uncertainties

The efficiencies of the lepton reconstruction algorithms and the muon trigger selection criteria differed between data and simulated events, and these differences were corrected by applying ∼unity event weights to simulated events. The uncertainties on these weights affected the signal and Drell-Yan background predictions. In the $\mu\mu$-channel, the trigger and lepton reconstruction efficiency weights varied with the p_T and η of the selected muons, and their uncertainties were statistical - based on the number of data and simulated events used to calculate the weights. The uncertainty on the muon reconstruction weight was negligible. For events triggered by muons that had $p_T < 140$ GeV, the muon trigger uncertainty resulted in an uncertainty below 0.5% on the signal and Drell-Yan predictions. For events triggered by higher p_T muons, the prediction uncertainty was below 3% if the triggering muon had $|\eta| < 2.1$; the uncertainty was 5.1% for higher $|\eta|$ muons. For events that passed the ee-channel criteria, an electron reconstruction efficiency weight of 0.982 was applied to all selected electrons, and propagated into the weight of each event. The reconstruction weight uncertainty, calculated as the maximum difference between 0.982 and an E_T, η dependent weight, resulted in a 2% uncertainty on the signal and Drell-Yan predictions. The lepton reconstruction and trigger uncertainties were included in limit calculations using log-normal distributions for the marginal posterior distributions.

6.3.5 Cross section, luminosity, pileup and PDF Uncertainties

Additional weights were applied to simulated W_R and Drell-Yan +jets events for reasons explained previously. The uncertainties on these weights resulted in additional, small uncertainties on the signal and Drell-Yan background predictions.

Simulated events were weighted by the integrated luminosity of data $\mathcal{L}$, the cross section σ, and the number of simulated events N_{evts}: $\frac{\mathcal{L}\times\sigma}{N_{evts}}$. The uncertainty on the

integrated luminosity measurement resulted in a 2.7% uncertainty on the signal and Drell-Yan predictions. The uncertainty on the Drell-Yan cross section, equivalent to the difference between Drell-Yan MC generators discussed in Chapter 5.3.1, resulted in a 2% uncertainty on the Drell-Yan prediction in the ee-channel, and a 1% uncertainty in the $\mu\mu$-channel. The uncertainty on the W_R cross section, calculated during simulations, resulted in an uncertainty below 0.5% on the signal prediction for all values of M_{W_R}.

The efficiency to reconstruct an interaction as a vertex was known exactly in simulated events, but could only be estimated to within $\sim$5% uncertainty in data events. As a result, there was an uncertainty on the number of pileup interactions reconstructed in each data event. Simulated events were weighted to bring the pileup distributions found in data and simulated events into agreement, ignoring the pileup uncertainty in data. The effect of the pileup uncertainty on the signal and background predictions was estimated by shifting the pileup distribution found in data within its uncertainty, and calculating new weights for simulated events. The change in the signal and Drell-Yan predictions using the new and original weights was taken as an uncertainty. The resulting uncertainty for signal and Drell-Yan predictions was between 2% and 3% for all $M_{\ell\ell jj}$ windows.

In simulated events, the distribution of momenta amongst gluons, up, down, and strange quarks, and their anti-quarks in interacting protons was modeled using one parton distribution function (pdf). Drell-Yan events were simulated using the NNPDF30 pdf [73], and signal events were simulated using the NNPDF23 pdf [74]. Both pdfs are parameterized in terms of the momentum fraction of the parton, the energy scale, and several constant coefficients and exponents whose values and uncertainties are determined using experimental data. In each simulated event these coefficients and exponents were varied within their uncertainties, and the average change in the cross section was propagated to the event weight. The average change in the total weight of all events

was taken as an uncertainty on the signal or Drell-Yan prediction. The uncertainty on the Drell-Yan prediction was between 2% and 3% for all $M_{\ell\ell jj}$ windows. As M_{W_R} increased from 0.8 to 4 TeV the uncertainty on the signal prediction increased from 1% to 15%. The portion of the W_R pdf uncertainty that affected the (η, ϕ) trajectories was below 1% for all values of M_{W_R}; only this portion of the uncertainty was included in limit calculations. The remaining uncertainty, that grew with M_{W_R}, depended on unconstrained parameters of the LRS model, and therefore was not included in limit calculations.

In each simulated pp interaction the coupling α_{QCD} was calculated at a renormalization energy scale μ_R, and QCD processes were divided into two regions based on a factorization energy scale μ_F. QCD processes that exchange momentum $Q^2 \ll \mu_F^2$ are not perturbative in α_{QCD}, and are simulated using low energy QCD models, and those that exchange momentum $Q^2 \gtrsim \mu_F^2$ are simulated using perturbative QCD [75]. Neither μ_R nor μ_F are extracted from experimental data or simulations, and no uncertainties are assigned to either parameter. Variations of μ_R or μ_F affect the simulated cross section, and therefore the signal and Drell-Yan predictions. The uncertainties on the signal and Drell-Yan predictions due to variations in μ_R and μ_F were estimated by simulating each signal and Drell-Yan event 8 different times, and each time increasing or decreasing one or both parameters by a factor of 2. Then, the change in cross section was propagated to the weight of each event. The maximum change in the total weight of all selected events relative to the standard μ_R and μ_F values was taken as an uncertainty on the prediction. The uncertainties on the signal and Drell-Yan predictions were below 3%.

These uncertainties on the signal and Drell-Yan predictions were included in limit calculations using log-normal distributions for the marginal posterior distributions.

6.3.6 Cumulative Uncertainty

The signal and background predictions, and their total uncertainties are listed in Table 6.3. The magnitudes of all uncertainties excluding the statistical uncertainty are summed in quadrature, and are listed as the systematic uncertainty.

Table 6.3: The predicted number of signal ($M_{N_l} = \frac{1}{2} M_{W_R}$) and background events, and the prediction uncertainties in several $M_{\ell\ell jj}$ windows. The uncertainties are expressed in number of events. BG = Total Background

	Electron channel			
M_{W_R} (GeV)	Signal (exp ± stat ± syst)	DY (exp ± stat ± syst)	Top quark (exp ± stat ± syst)	$\sum$ BG (exp ± stat ± syst)
1000	1196.0 ± 15.0 ± 46.0	21.11 ± 1.64 ± 8.79	40.87 ± 4.2 ± 4.76	61.99 ± 4.51 ± 10.0
2200	38.0 ± 0.4 ± 1.5	2.66 ± 0.15 ± 1.16	2.25 ± 0.99 ± 0.3	4.92 ± 1.0 ± 1.2
3000	7.3 ± 0.07 ± 0.27	1.02 ± 0.09 ± 0.44	0.43 ± 0.43 ± 0.05	1.45 ± 0.44 ± 0.45
4000	1.0 ± 0.01 ± 0.04	0.65 ± 0.08 ± 0.29	0.0 ± 0.43 ± 0.0	0.65 ± 0.44 ± 0.29
	Muon channel			
M_{W_R} (GeV)	Signal (exp ± stat ± syst)	DY (exp ± stat ± syst)	Top quark (exp ± stat ± syst)	$\sum$ BG (exp ± stat ± syst)
1000	1805.0 ± 17.9 ± 83.1	42.16 ± 2.28 ± 17.85	70.51 ± 6.82 ± 7.97	112.67 ± 7.19 ± 19.55
2200	52.0 ± 0.5 ± 2.5	4.97 ± 0.25 ± 2.14	3.44 ± 1.51 ± 0.45	8.41 ± 1.53 ± 2.18
3000	9.1 ± 0.08 ± 0.39	2.62 ± 0.16 ± 1.13	0.66 ± 0.66 ± 0.08	3.28 ± 0.68 ± 1.13
4000	1.2 ± 0.01 ± 0.05	1.37 ± 0.1 ± 0.63	0.0 ± 0.66 ± 0.0	1.37 ± 0.67 ± 0.63

6.4 Results Summary

The $M_{\ell\ell jj}$ distributions were divided into finite width $M_{\ell\ell jj}$ windows linked to specific M_{W_R} hypotheses. In each window the background prediction and its uncertainties was compared to the data, and no statistically significant excess of data above the background was found. Limits on the product of the W_R cross section and branching ratio were calculated at 95% CL for $M_{N_l} = \frac{1}{2}M_{W_R}$, and transformed into exclusion limits on M_{W_R} and M_{N_l} that extend to ∼3.5 TeV in W_R mass, and to ∼2.2 TeV in N_l mass. These extend the Run I mass limits 150 GeV or higher in M_{N_l}, and 400 GeV higher in M_{W_R}.

Chapter 7

Conclusion

The LRS model extends the Standard Theory of particle physics to explains the low ST neutrino masses, and the large abundance of baryons relative to anti-baryons in the universe. The model predicts heavy neutrinos N_l that couple to a heavy, charged W_R boson. The W_R couples to quarks, so it can be produced in proton-proton collisions. In events with two charged leptons and two jets collected by the CMS experiment in 2015, evidence of a W_R and N_l was searched for as an excess of data above the predicted background in the M_{eejj} and $M_{\mu\mu jj}$ distributions. No statistically significant excess was found, so the data was used to set upper limits on $\sigma(W_R) \times BR(\ell\ell jj)$ at 95% CL for $M_{N_l} = \frac{1}{2}M_{W_R}$, which were extrapolated into exclusion limits on M_{W_R} and M_{N_l} for $M_{N_l} < M_{W_R}$. The limit excludes $M_{W_R} < 3500$ GeV and $M_{N_l} < 2200$ GeV in the $\mu\mu$-channel, and $M_{W_R} < 3300$ GeV and $M_{N_l} < 2200$ GeV in the ee-channel. Relative to the Run I mass limits [33], the mass limits were extended 400 GeV higher in M_{W_R}, and at least 150 GeV higher in M_{N_l}. In addition, no evidence of the 2.8σ significance excess from Run I in the ee-channel was found.

Areas of the (M_{W_R}, M_{N_l}) phase space that could not be probed using the data, like $M_{W_R} \gtrsim 4$ TeV and $M_{N_l} < \frac{1}{8}M_{W_R}$ for all M_{W_R}, are being studied using newer

data. Evidence of the W_R and N_l with $M_{W_R} > 3500$ GeV and $M_{N_l} > 2200$ GeV is being searched for using the 37.8 fb^{-1} of data [38] collected by CMS in 2016. The event selection applied to events in 2016 data is nearly identical to the event selection described in this thesis, so the search using 2016 data will not have significantly more sensitivity to LRS models that predict $M_{N_l} \lesssim \frac{1}{8} M_{W_R}$. A separate analysis using the 2016 data is searching for evidence of a W_R and N_l in the phase space where the N_l mass is light relative to the W_R mass, $M_{N_l} < \frac{1}{8} M_{W_R}$. In this search, events are selected using a completely different set of selection criteria that are optimized for signals with low N_l mass and high W_R mass, such as a smaller ΔR separation requirement between the leptons and jets.

References

[1] Hans Peter Beck and Uni Bern. The 2013 Nobel Prize in Physics. November 2013. General Photo.

[2] Richard Ruiz. Drell-Yan, Drell-Yan with Jets, Drell-Yan with all the Jets. 2015. General Photo.

[3] CDF Collaboration. Is the top hiding a charged Higgs? May 2014. General Photo.

[4] Andrea Giammanco. Measurement of the t-channel single Top-quark production rates in pp collisions at 7 TeV. September 2011. General Photo.

[5] Steven Weinberg. A model of leptons. *Phys. Rev. Lett.*, 19:1264–1266, Nov 1967.

[6] A. Salam. *in Elementary Particle Theory.* ed. N. Svartholm, (Almquist and Forlag 1968).

[7] F. Reines and C. L. Cowan. Detection of the free neutrino. *Phys. Rev.*, 92:830–831, Nov 1953.

[8] G. Danby, J-M. Gaillard, K. Goulianos, L. M. Lederman, N. Mistry, M. Schwartz, and J. Steinberger. Observation of high-energy neutrino reactions and the existence of two kinds of neutrinos. *Phys. Rev. Lett.*, 9:36–44, Jul 1962.

[9] DONUT Collaboration. Observation of tau neutrino interactions. *Phys. Lett.*, B504:218–224, 2001, hep-ex/0012035.

[10] C. S. Wu, E. Ambler, R. W. Hayward, D. D. Hoppes, and R. P. Hudson. Experimental test of parity conservation in beta decay. *Phys. Rev.*, 105:1413–1415, Feb 1957.

[11] "F.J. Hasert et. al.". "observation of neutrino-like interactions without muon or electron in the gargamelle neutrino experiment". *"Physics Letters B"*, "46"("1"):"138 – 140", "1973".

[12] ATLAS and CMS Collaborations. Combined measurement of the higgs boson mass in pp collisions at $\sqrt{s} = 7$ and 8 tev with the atlas and cms experiments. *Phys. Rev. Lett.*, 114, May 2015.

[13] K. S. Hirata et al. Observation of 8b solar neutrinos in the kamiokande-ii detector. *Phys. Rev. Lett.*, 63:16–19, Jul 1989.

[14] John N. Bahcall. Two solar neutrino problems. *Phys. Lett.*, B338:276–281, 1994.

[15] NOvA Collaboration. First measurement of electron neutrino appearance in nova. *Phys. Rev. Lett.*, 116:151806, Apr 2016.

[16] Mainz Collaboration. Final results from phase ii of the mainz neutrino mass search in tritium β decay. *The European Physical Journal C - Particles and Fields*, 40(4):447–468, 2005.

[17] T2K Collaboration. The T2K Experiment. *Nuclear Instruments and Methods in Physics Research Section A: Accelerators, Spectrometers, Detectors and Associated Equipment*, 659(1):106 – 135, 2011.

[18] F. P. An et al. Observation of electron-antineutrino disappearance at daya bay. *Phys. Rev. Lett.*, 108:171803, Apr 2012.

[19] IGEX Collaboration. Igex ^{76}Ge neutrinoless double-beta decay experiment: Prospects for next generation experiments. *Phys. Rev. D*, 65:092007, May 2002.

[20] GERDA Collaboration. Results on neutrinoless double-β decay of ^{76}Ge from phase i of the gerda experiment. *Phys. Rev. Lett.*, 111:122503, Sep 2013.

[21] Jogesh C. Pati and Abdus Salam. Lepton Number as the Fourth Color. *Phys. Rev.*, D10:275–289, 1974. [Erratum: Phys. Rev.D11,703(1975)].

[22] G. Senjanovic and R. N. Mohapatra. Exact left-right symmetry and spontaneous violation of parity. *Phys. Rev. D*, 12:1502–1505, Sep 1975.

[23] G. Senjanović. Spontaneous breakdown of parity in a class of gauge theories. *Nuclear Physics B*, 153:334–364, 1979.

[24] R. N. Mohapatra and G. Senjanovic. Neutrino mass and spontaneous parity nonconservation. *Phys. Rev. Lett.*, 44:912–915, Apr 1980.

[25] Murray Gell-Mann, Pierre Ramond, and Richard Slansky. Complex Spinors and Unified Theories. *Conf. Proc.*, C790927:315–321, 1979, 1306.4669.

[26] D0 Collaboration. Evidence for an anomalous like-sign dimuon charge asymmetry. *Phys. Rev. D*, 82:032001, Aug 2010.

[27] Alessio Maiezza, Miha Nemevšek, Fabrizio Nesti, and Goran Senjanović. Left-right symmetry at lhc. *Phys. Rev. D*, 82:055022, Sep 2010.

[28] Yosef Nir. CP violation in and beyond the standard model. In *Proceedings, 27th SLAC Summer Institute on Particle Physics: CP Violation in and Beyond the*

Standard Model (SSI 99): Stanford, USA, July 7-16, 1999, pages 165–243, 1999, hep-ph/9911321.

[29] Chakrabortty, J. and Gluza, J. and Jelinski, T. and Srivastava, T. Theoretical constraints on masses of heavy particles in Left-Right Symmetric Models. *Phys. Lett.*, B759:361–368, 2016, 1604.06987.

[30] Y. Zhang, H. An, X. Ji, and R. N. Mohapatra. General cp violation in minimal left-right symmetric model and constraints on the right-handed scale. *Nuclear Physics B*, 802:247–279, Oct 2008.

[31] Measurement of the production cross section for pp to Z(nu nu) gamma at sqrt(s) = 13 TeV at CMS. Technical Report CMS-PAS-SMP-16-004, CERN, 2016.

[32] CMS Collaboration. Searches for invisible decays of the Higgs boson in pp collisions at sqrt(s) = 7, 8, and 13 TeV. *JHEP*, 02:135, 2017, 1610.09218.

[33] CMS Collaboration. Search for heavy neutrinos and w bosons with right-handed couplings in proton-proton collisions at $\sqrt{s} = 8$ tev. *The European Physical Journal C*, 74(11):3149, 2014.

[34] The CMS Collaboration. The CMS Experiment at the CERN LHC. *JINST*, 3:S08004, 2008.

[35] Oliver Sim Brning, Paul Collier, P Lebrun, Stephen Myers, Ranko Ostojic, John Poole, and Paul Proudlock. *LHC Design Report*. CERN Yellow Reports: Monographs. CERN, Geneva, 2004.

[36] ATLAS Collaboration. *ATLAS detector and physics performance: Technical Design Report, 2*. Technical Design Report ATLAS. CERN, Geneva, 1999.

[37] The CMS Collaboration. Cms physics technical design report, volume ii: Physics performance. *Journal of Physics G: Nuclear and Particle Physics*, 34(6):995, 2007.

[38] CMS. Cms luminosity public results. 2017.

[39] CMS Collaboration. The commissioning and performance of the CMS pixel tracker with cosmic ray muons. *JINST*, 5:T03007, 2010.

[40] CMS Collaboration. Cms physics: Technical design report volume 1: Detector performance and software. Cms technical design report, 2006.

[41] The CMS Collaboration. Description and performance of track and primary-vertex reconstruction with the cms tracker. *Journal of Instrumentation*, 9(10):P10009, 2014.

[42] CMS Collaboration. Performance of cms muon reconstruction in pp collision events at s = 7 tev. *Journal of Instrumentation*, 7(10):P10002, 2012.

[43] CMS Collaboration. Energy calibration and resolution of the cms electromagnetic calorimeter in pp collisions at s = 7 tev. *Journal of Instrumentation*, 8(09):P09009, 2013.

[44] CMS Collaboration. Cms: The electromagnetic calorimeter technical design report. Cms technical design report, 1997.

[45] CMS Collaboration. Electron and photon energy calibration and resolution with the cms ecal at $\sqrt{s}$ = 7 TeV. CMS Physics Analysis Summary CMS-PAS-EGM-11-001, 2011.

[46] CMS Collaboration. Jet energy scale and resolution in the CMS experiment in pp collisions at 8 TeV. *JINST*, 12(CMS-JME-13-004. CERN-PH-EP-2015-305. CMS-JME-13-004):P02014. 92 p, Jul 2016.

[47] CMS Collaboration. Performance of the cms muon detector and reconstruction with pp collisions at $\sqrt{s} = 13$ TeV. CMS Physics Analysis Summary CMS-PAS-MUO-16-001, 2016.

[48] CMS Collaboration. The cms trigger system. *Journal of Instrumentation*, 12(01):P01020, 2017.

[49] Wolfgang Adam, R. Frhwirth, Are Strandlie, and T. Todor. Reconstruction of electrons with the gaussian-sum filter in the cms tracker at the lhc. 2005.

[50] Electron reconstruction and identification at sqrt(s) = 7 TeV. 2010.

[51] Particle-Flow Event Reconstruction in CMS and Performance for Jets, Taus, and MET. Technical Report CMS-PAS-PFT-09-001, Geneva, Apr 2009.

[52] CMS Collaboration. Commissioning of the particle-flow reconstruction in minimum-bias and jet events from pp collisions at 7 tev. CMS Physics Analysis Summary CMS-PAS-PFT-10-002, 2010.

[53] Transverse-momentum and pseudorapidity distributions of charged hadrons in *pp* collisions at $\sqrt{s} = 7$ TeV. *Phys. Rev. Lett.*, 105(arXiv:1005.3299. CMS-QCD-10-006. CERN-PH-EP-2010-009):022002. 26 p, May 2010.

[54] Matteo Cacciari, Gavin P. Salam, and Gregory Soyez. The anti-k_t jet clustering algorithm. *JHEP*, 04:063, 2008, 0802.1189.

[55] S. Catani, Yu.L. Dokshitzer, and B.R. Webber. The k-clustering algorithm for jets in deep inelastic scattering and hadron collisions. *Physics Letters B*, 285(3):291 – 299, 1992.

[56] S. Catani, Yu.L. Dokshitzer, M.H. Seymour, and B.R. Webber. Longitudinally-invariant k-clustering algorithms for hadron-hadron collisions. *Nuclear Physics B*, 406(1):187 – 224, 1993.

[57] Stephen D. Ellis and Davison E. Soper. Successive combination jet algorithm for hadron collisions. *Phys. Rev. D*, 48:3160–3166, Oct 1993.

[58] Matteo Cacciari, Gavin P. Salam, and Gregory Soyez. The catchment area of jets. *JHEP*, 04:005, 2008, 0802.1188.

[59] Matteo Cacciari and Gavin P. Salam. Pileup subtraction using jet areas. *Phys. Lett. B*, 659:119, 2008, 0707.1378.

[60] Marc Stoever. Searches for new physics in lepton+jet final states. Technical Report CMS-CR-2017-284, CERN, Geneva, Sep 2017.

[61] CMS Collaboration. Measurement of the differential cross sections for the associated production of a W boson and jets in proton-proton collisions at sqrt(s) = 13 TeV. 2017, 1707.05979.

[62] CMS Collaboration. Measurement of the double-differential inclusive jet cross section in proton–proton collisions at sqrt(s) = 13 tev. *The European Physical Journal C*, 76(8):451, Aug 2016.

[63] J. Alwall et al. Madgraph 5: Going beyond. *JHEP*, 06:128, 2011, 1106.0522.

[64] Simone Alioli et al. A general framework for implementing NLO calculations in shower monte carlo programs: the POWHEG BOX. *JHEP*, 06:043, 2010, 1002.2581.

[65] Torbjörn Sjöstrand, Stephen Mrenna, and Peter Skands. A brief introduction to PYTHIA 8.1. *Computer Physics Communications*, 178:852–867, 2007, 0710.3820.

[66] Torbjörn Sjöstrand, Stephen Mrenna, and Peter Skands. PYTHIA 6.4 physics and manual. *JHEP*, 05:026, 2006, hep-ph/0603175.

[67] Simone Alioli, Paolo Nason, Carlo Oleari, and Emanuele Re. NLO single-top production matched with shower in POWHEG: s- and t-channel contributions. *JHEP*, 09:111, 2009, 0907.4076. [Erratum: JHEP02,011(2010)].

[68] Tom Melia, Paolo Nason, Raoul Rontsch, and Giulia Zanderighi. W+W-, WZ and ZZ production in the POWHEG BOX. *JHEP*, 11:078, 2011, 1107.5051.

[69] CMS Collaboration. Event generator tunes obtained from underlying event and multiparton scattering measurements. *EPJC*, 76(3):155, Mar 2016.

[70] R. Ball, V. Bertone, F. Cerutti, L. Del Debbio, S. Forte, A. Guffanti, J. I. Latorre, J. Rojo, and M. Ubiali. Unbiased global determination of parton distributions and their uncertainties at NNLO and at LO. *Nucl. Phys. B*, 855:153, 2012, 1107.2652.

[71] S. Agostinelli et al. GEANT4 – a simulation toolkit. *Nucl. Instrum. Meth. A*, 506:250, 2003.

[72] Search for narrow resonances in dilepton mass spectra in protonproton collisions at s=13tev and combination with 8 tev data. *Physics Letters B*, 768(Supplement C):57 – 80, 2017.

[73] R. Ball, V. Bertone, S. Carrazza, C. S. Deans, L. Del Debbio, S. Forte, A. Guffanti, N. P. Hartland, J. I. Latorre, J. Rojo, and M. Ubiali. Parton distributio0ns for the lhc run ii. *JHEP*, 04:151, 2015, 1410.8849.

[74] R. Ball, V. Bertone, F. Cerutti, L. Del Debbio, S. Forte, A. Guffanti, J. I. Latorre, J. Rojo, and M. Ubiali. Unbiased global determination of parton distributions and their uncertainties at NNLO and at LO. *Nucl. Phys. B*, 855:153, 2012, 1107.2652.

[75] Collins, John C. and Soper, Davison E. and Sterman, George F. Factorization of Hard Processes in QCD. *Adv. Ser. Direct. High Energy Phys.*, 5:1–91, 1989, hep-ph/0409313.

[76] Andrew Gelman, John B. Carlin, Hal S. Stern, David B. Dunson, Aki Vehtari, and Donald B. Rubin. *Bayesian Data Analysis, Third Edition.* Chapman and Hall/CRC Texts in Statistical Science. Chapman and Hall/CRC, 2013.

Appendix A

Glossary and Acronyms

Care has been taken in this thesis to minimize the use of jargon and acronyms, but this cannot always be achieved. This appendix defines jargon terms in a glossary, and contains a table of acronyms and their meaning.

A.1 Glossary

- **barrel** – The central η region of each sub-detector is called the barrel.
- **endcap** – The high η region of each sub-detector is called the endcap.
- **hadronization** – The process through which bare quarks and gluons become color neutral hadrons.
- **interaction point** – The region at the center of the detector where proton-proton interactions occur.
- **minimum bias collisions** – A collection of randomly selected proton-proton collision events where energy is detected in CMS. Due to its high cross section, inelastic and diffractive proton-proton collisions constitute the majority of minimum

bias collisions.

- **nuclear interaction length** – On average a relativistic hadron will experience one nuclear interaction after travelling through one nuclear interaction length of material.
- **pileup** – Additional proton-proton interactions that occur in the same collision event.
- **reconstruction** – The process through which detector information is transformed into particles used in physics analyses.
- **Supercluster** (**SC**) – A 5×5 crystal region in the Electromagnetic Calorimeter.
- **Supercluster seed crystal** (**SC seed**) – The highest energy crystal in a Supercluster.

A.2 Acronyms

Table A.1: Acronyms

Acronym	Meaning
CRμ	Cosmic-Ray Muon

Appendix B

Trigger and Offline Selection Criteria

During collisions, events with two muons were selected using a Level-1 trigger that required one track segment with $p_T > 16$ GeV. The segment was required to have measurements in DT or CSC chambers from at least 2 stations, and in at least 4 layers of each chamber. In the HLT, the following selection criteria were applied:

- A track was reconstructed in the silicon tracker with $p_T > 50$ GeV and $|\eta| < 2.4$.
- In the plane perpendicular to the beam axis, the distance between the silicon tracker track origin and its reconstructed vertex was < 1 mm.
- The muon detector track that passed the L1 trigger extrapolated back to the silicon tracker track (η, ϕ) position to within 3 cm.

During collisions, events with an electron and a muon were selected using the single muon Level-1 trigger described previously. In the HLT, the following selection criteria were applied:

- A track reconstructed in the silicon tracker with $p_T > 30$ GeV and $|\eta| < 2.4$ was geometrically matched to the muon detector track segment that passed the L1 trigger.
- In the plane perpendicular to the beam axis, the distance between the track and the reconstructed vertex was < 1 mm.
- At least one 5×5 ECAL crystal cluster was required to have $E_T > 30$ GeV, and:
  - the hadronic energy behind the cluster was $< 15\%$ of E_T in the barrel, and $< 10\%$ of E in the endcap.
  - Ninety percent of the cluster's energy was measured in an area that was only two crystals wide in η.
  - For a barrel cluster, a reconstructed track that was measured in at least two pixel tracker layers extrapolated from the pixel tracker to within 2.3 cm of the cluster position in z, and to within the width of one crystal from the cluster (η, ϕ) position.

In events selected by the single muon trigger and the electron-muon trigger, tracks in the muon detectors and silicon tracker were identified as being caused by muons using reconstruction algorithms described in Chapter 4. Then, the following offline selection criteria were applied to select promptly produced muons that were isolated from other particles, and reconstructed in multiple muon stations:

- The muon track reconstructed in the silicon tracker:
  - Was reconstructed from signals in at least 1 silicon pixel detector layer, and signals in at least 5 layers in the entire tracker.
  - Within a cone of radius $\Delta R = 0.3$ centered on the track, the $\sum p_T$ of all other reconstructed tracks was low compared to the muon p_T, $\frac{\sum p_T}{muon p_T} < 0.1$.

- The muon's track segment went through a muon chamber in at least 2 muon stations. Track segments in each DT chamber were required to have signals in all 4 r-z layers, and at least 7 of 8 r-ϕ layers. Track segments in each CSC were required to have signals in all 6 layers.

- The origin of the muon's silicon tracker track was within 2 mm of the muon's reconstructed vertex position along the z axis.

During collisions, events with two electrons were selected using single and double-electron Level-1 triggers. These triggers required one 5×5 ECAL crystal cluster that had $E_T > 40$ GeV, or two 5×5 ECAL clusters that had $E_T > 22$ GeV and $E_T > 10$ GeV. In the HLT, the following selection criteria were applied:

- At least two 5×5 ECAL crystal clusters separated by $\Delta R > 0.1$ were required to have $E_T > 33$ GeV.

- For each ECAL cluster:

  - The hadronic energy behind the cluster was $< 15\%$ of E_T in the barrel, and $< 10\%$ of E_T in the endcap.

  - Ninety percent of E_T was measured in an area that was only two crystals wide in η.

  - For a barrel cluster, a reconstructed track that was measured in at least two pixel tracker layers extrapolated from the pixel tracker to within 2.3 cm of the cluster position in z, and to within the width of one crystal from the cluster (η, ϕ) position.

In events selected by the double-electron trigger and the electron-muon trigger, reconstructed tracks and ECAL SCs were identified as being caused by electrons using

the algorithms described in Chapter 4. Then, the following offline selection criteria were applied to select the promptly produced electrons that were isolated from other particles, excluding the electrons in the ECAL transition region $1.44 < |\eta| < 1.57$:

- The electron E_T is the calibrated ECAL SC energy E_{SC}.
- For a SC in the barrel, at least 94% of E_{SC} was measured in an area that was 2 crystals wide in η.
- The hadronic energy (H) behind the SC was $\frac{H}{E_{SC}} < 0.05 + \frac{1\text{GeV}}{E_{SC}}$ in the barrel, and $\frac{H}{E_{SC}} < 0.05 + \frac{5\text{GeV}}{E_{SC}}$ in the endcap.
- In a $\Delta R = 0.3$ radius cone centered on the electron's (η, ϕ) trajectory:
  - The $\sum p_T$ of all tracks excluding the electron's track was low, $\sum p_T < 5$ GeV.
  - The total calorimeter energy $E_{ECAL+HCAL}$ not associated with the electron was $E_{ECAL+HCAL} < 2 + 0.03\alpha + 0.28\rho$. ρ is the neutral particle energy per unit η, ϕ area, α in the barrel is E_{SC}, and α in the endcap is $E_{SC} - 50$.
- For a SC in the endcap, the electron track extrapolated from the outermost silicon tracker measurement to the SC seed crystal position to within ~3 crystal widths in ϕ.
- The electron track was reconstructed from signals in every silicon pixel and inner strip detector layers, or all but 1 layer.
- The electron track's origin was separated from its vertex by a small distance Δ_{xy} in the $x - y$ plane: $\Delta_{xy} < 0.2$ mm in the tracker barrel, and $\Delta_{xy} < 0.5$ mm in the tracker endcap.

In events selected by the lepton triggers, jets were reconstructed from tracks and calorimeter energy clusters using the algorithms described previously. Then, the following offline selection criteria were applied to select jets that contained at least one charged hadron, and whose energies were not dominated by electron or photon SCs:

- Each jet had at least two constituents, and at least one was a charged hadron.
- Less than 90% of the total energy of each jet came from neutral hadrons.
- Less than 90% of the total energy of each jet came from photons.
- Less than 99% of the total energy of each jet came from electrons.

B.1 Drell-Yan Control Region Triggers

During collisions, events with two muons were selected using a Level-1 trigger that required one track segment with $p_T > 20$ GeV. The segment was required to have measurements in DT or CSC chambers from at least 2 stations, and in at least 4 layers of each chamber. In the HLT, the following selection criteria were applied:

- A track reconstructed in the silicon tracker with $p_{T1} > 22$ GeV and $|\eta| < 2.4$ was geometrically matched to the muon detector track segment, reconstructed with p_{T2} that passed the L1 trigger.
- In the plane perpendicular to the beam axis, the distance between the silicon tracker track origin and its reconstructed vertex was < 1 mm.
- In a $\Delta R = 0.3$ radius cone centered on the muon trajectory:
  - The total ECAL energy was $< 11\%$ of p_{T2} in the barrel, and $< 8\%$ of p_{T2} in the endcap.

  - The total HCAL energy was $< 21\%$ of p_{T2} in the barrel, and $< 22\%$ of p_{T2} in the endcap.
  - The total p_T of all silicon tracker tracks excluding the muon track was $< 9\%$ of p_{T1}.

During collisions, events with two electrons were selected using a single electron Level-1 trigger that required one 5×5 ECAL crystal cluster that had an $E_T > 30$ GeV and an $|\eta| < 2.1$. In the HLT, the following selection criteria were applied:

- At least one 5×5 ECAL crystal cluster was required to have $E_T > 30$ GeV, and a second non-overlapping cluster was required to have $E_T > 4$ GeV.
- For the cluster with $E_T > 30$ GeV:
  - The hadronic energy behind the cluster was $< 5.5\%$ of E_T in the barrel, and $< 7\%$ of E_T in the endcap.
  - Ninety percent of E_T was measured in an area that was only two crystals wide in η.
  - A reconstructed track that was measured in at least two pixel tracker layers extrapolated from the pixel tracker to within 1 cm of the cluster position in z, and to within the width of one crystal from the cluster (η, ϕ) position.
  - The cluster E_T and the p_T of the matching track did not differ by more than 50%.
  - In a $\Delta R = 0.3$ radius cone centered on the cluster:
    * The total ECAL energy not measured in the cluster was $< 22.5\%$ of E_T in the barrel, and $< 12.1\%$ of E_T in the endcap.
    * The total HCAL energy was $< 15.5\%$ of E_T in the barrel, and $< 16\%$ of E_T in the endcap.

In events selected by the electron and muon triggers, reconstructed tracks in the silicon tracker and muon detectors, and ECAL SCs were identified as being caused by muons and electrons using the algorithms described in Chapter 4. Then, the offline selection criteria described previously were applied to select events with two electrons or two muons.

Appendix C

Bayesian Limits

The W_R cross section $\times$ branching ratio ($\sigma(W_R)\times BR(W_R \to \ell\ell jj)$) limits are calculated using several quantities. Each limit for a specific M_{W_R} signal is calculated using the number of measured events G and predicted signal (S) and background (B) events in the $M_{\ell\ell jj}$ window, and their uncertainties δS and δB. Expected limits, calculated by setting $G = B$, were used to determine the sizes of the $M_{\ell\ell jj}$ windows. Expected limits were calculated at 95% confidence level (CL) using a Poisson model of the SB events:

$$Poisson(\mu S(\boldsymbol{\theta}) \;\; B(\boldsymbol{\theta})) \tag{C.1}$$

where μ is the dimensionless W_R signal strength, and $\boldsymbol{\theta}$ represent the uncertainties δS and δB described later in Section 6.3. Using Bayesian statistics, the probability distribution for μ given G measured events, $p(\mu|G)$, is obtained by evaluating the integral [76]:

$$p(\mu|G) = \int p(\mu|\boldsymbol{\theta}, G)p(\boldsymbol{\theta}|G)d\boldsymbol{\theta} \tag{C.2}$$

where $p(\boldsymbol{\theta}|G)$ are the probability distributions for the uncertainties given the measurement G ("marginal posterior distributions"), and $p(\mu|\boldsymbol{\theta}, G)$ are the probability distributions for μ given the uncertainties, and the measurement G ("conditional posterior distributions"). Functional forms of the marginal posterior distributions are either log-normal or Gamma distributions depending on the uncertainty, and are identified later for specific uncertainties. Functional forms of the conditional posterior distributions are derived from uniform prior distributions and Equation C.1. The integrals in Equation C.2 were evaluated numerically using MC methods to derive $p(\mu|G)$. Then, $p(\mu|G)$ was integrated from $\mu = 0$ to $\mu = \mu_{max}$ such that the normalized integral equaled 0.95. The value μ_{max} is the 95% CL upper limit on the signal strength. The value of $\sigma(W_R) \times BR(W_R \to \ell\ell jj)$ obtained from simulations is multiplied by μ_{max} to calculate the upper limit on $\sigma(W_R) \times BR(W_R \to \ell\ell jj)$.